THESIS FOR THE DEGREE OF LICENTIATE OF ENGINEERING

Structure evolution of spin-coated phase-separated EC/HPC films

PIERRE CARMONA

CHALMERS
UNIVERSITY OF TECHNOLOGY

Department of Physics
CHALMERS UNIVERSITY OF TECHNOLOGY
Gothenburg, Sweden 2021

Structure evolution of spin-coated phase-separated EC/HPC films

CARMONA PIERRE

pierre.carmona@chalmers.se
Department of Physics
Division Nano- and Biophysics
Eva Olsson Group
CHALMERS University of Technology | chalmers.se
Fysikgränd 3 | 412 96, Gothenburg, Sweden

pierre.carmona@ri.se
Division Bioeconomy and Health
Department Agriculture and Food
Unit Product Design
RISE Research Institutes of Sweden | ri.se
Frans Perssons väg 6 | Box 5401, SE-402 29, Gothenburg, Sweden

Cover:
Micrographs of a phase-separated EC/HPC film with EC:HPC ratio 63:37 wt%, showing the HPC phase (bright) and the EC phase (dark). The images were acquired with a confocal scanning laser microscope with 300x magnification (field of view of 52x30 µm). From left to right, the micrographs correspond to the times $t = 256$, 284 and 328 s after spinning.

Printed by:
Chalmers Reproservice
Gothenburg, Sweden 2021

Structure evolution of spin-coated phase-separated EC/HPC films

PIERRE CARMONA
Department of Physics, Chalmers University of Technology

ABSTRACT

Porous phase-separated films made of ethylcellulose (EC) and hydroxypropylcellulose (HPC) are commonly used for controlled drug release. The structure of these thin films is controlling the drug transport from the core to the surrounding liquid in the stomach or intestine. However, detailed understanding of the structure evolution is lacking. In this work, we use spin-coating, a widely applied technique for making thin uniform polymer films, to mimic the industrial manufacturing process of fluidized bed spraying. The aim of this work is to understand the structure evolution and phase separation kinetics of single layer and multi-layer spin-coated EC/HPC films. The structure evolution is characterized using confocal laser scanning microscopy (CLSM) and image analysis.

The influence of spin-coating parameters and EC:HPC ratio on the final phase-separated structure and the film thickness was determined. Varying spin speed and EC:HPC ratio gave us precise control over the characteristic length scale and thickness of the film. The results show that the phase separation occurs through spinodal decomposition and that the characteristic length scale increases with decreasing spin speed and with increasing HPC ratio. The thickness of the spin-coated film decreases with increasing spin speed.

Furthermore, optimized spin-coating parameters were selected to study the kinetics of phase separation *in situ,* in particular the coarsening mechanisms and the time dependence of the domain's growth as a function of EC:HPC ratio. We identified two main coarsening mechanisms: interfacial tension driven hydrodynamic growth for the bicontinuous structure and diffusion driven coalescence for the discontinuous structures. In addition, we obtained information on the wetting, the shrinkage, and the evaporation process by looking at a film cross section, which allowed an estimation of the binodal of the phase diagram.

The findings from this work give a good understanding of the mechanisms responsible for the morphology development and open the road towards tailoring thin EC/HPC film structures for controlled drug release.

Keywords: biopolymer, cellulose, phase separation, confocal laser scanning microscope, spin-coating, porous film, kinetics, phase separation mechanisms, controlled drug release, drug delivery

PREFACE

The research presented in this work was carried out at the Department of Agriculture and Food, RISE Research Institutes of Sweden, Gothenburg, Sweden during the period October 2018 – May 2021. Main supervisor was Adj. Prof. Niklas Lorén, RISE, and assistant supervisors were Adj. Ass. Prof. Magnus Röding, RISE, and Prof. Aila Särkkä, Department of Mathematical Sciences, Chalmers University of Technology and Gothenburg University. Examiner was Prof. Eva Olsson, Department of Physics, Chalmers University of Technology. The research was done in collaboration with the Eva Olsson group, Department of Physics, Chalmers University of Technology and Dr. Christian von Corswant from AstraZeneca.

The work was founded by the Swedish Foundation of Strategic Research. The project was also supported by AstraZeneca.

List of publications

Paper I.	*Structure evolution during phase separation in spin-coated ethylcellulose/hydroxypropylcellulose films*. **Carmona, P**., Röding, M., Särkkä, A., von Corswant, C., Olsson, E., & Lorén, N. Published in Soft Matter (2021); DOI: 10.1039/d1sm00044f
Paper II.	*Structure formation and coarsening kinetics of phase-separated spin-coated ethylcellulose/hydroxypropylcellulose films.* **Carmona, P**., Röding, M., Särkkä, A., Olsson, E., von Corswant, C., & Lorén, N. Manuscript

Contribution Report

For Paper I and II.: Planned and performed the experimental work; carried out the calculation; image analysis and discussion with co-authors; wrote the paper.

ACKNOWLEDGEMENTS

Firstly, I would like to express my sincere gratitude to my advisor Niklas Lorén, RISE, for the continuous support of my PhD study and related research, for his never-ending optimism, motivation, and knowledge. His guidance helped me throughout the research and writing of this thesis. But also, to my co-supervisors, Magnus Röding, RISE, and Aila Särkkä, Chalmers. Magnus for the many hours spent together writing in MATLAB, it is another language that I wish to master soon.

I want to thank Eva Olsson, Chalmers, for the warm welcome in the Eva Olsson group and the continuous support. Your feedback is always so useful to me. Also, I want to thank the whole Eva Olsson group, my fellow colleagues, for the fruitful talks during our gathering about science and everything else: Cecilia, Gustav, Jonathan, Torben, Andy, Ludwig, Lunjie, Gabriel, Fredrik, Shun, Xin, Carl and Rebecka.

My sincere thanks also to all RISE team, and especially the whole Product and Design Unit for the conviviality and the funny talk during coffee break, also for teaching me how to use my dear confocal microscope. Special thanks to Ana, my roomie, you are always here to support me, rehearse all my presentations with me and your laughter. But also, Patricia, Nodas, Mihaela, Loredana and Gonzalo.

The people from AstraZeneca, Anna Olsson and mainly Christian von Corswant for the support and all the fruitful talks and your deep knowledge on the EC/HPC system.

I thank the friend from Sweden, present the whole time. My thanks go to Cecilia, Kengo, Govin, Måns, Ida, Emma and Pavlina. Cecilia thank you for our laughs and for bringing joy in my life, you are my first and my best friend here, and I am so happy about this. Emma thank you for your optimism, joy, and bringing me into the Swedish culture.

Last but not the least, I would like to thank my family: my parents to begin with and my twin brother Julien for supporting me throughout writing this thesis and in my life in general. Merci à ma famille : les cousins Thomas, Charlotte, Camille mais aussi et surtout Brigitte ma grand-mère pour son soutien constant. Les amis du BAFA : Kim, Zucchi et Nina mais aussi mes colocataires de cœur : Katz, Wuiwui, Louis, Simonou, Léouch, Loulou, Claire, Lulu et Auré. Merci, merci, d'avoir été là pour moi, à m'écouter me plaindre, à me supporter et à m'aider à avancer dans la thèse mais aussi dans la vie.

List of abbreviations and acronyms

CLSM	Confocal Laser Scanning Microscopy
EC	Ethylcellulose
FFT	Fast-Fourier Transform
FOV	Field Of View
HPC	Hydroxypropylcellulose
Mw	Molecular weight
NG	Nucleation and Growth
SD	Spinodal Decomposition

TABLE OF CONTENTS

1 Introduction

Controlled drug release formulations are used to deliver drugs at predetermined rates and periods of time in the body to optimize the efficiency of the drug and to minimize side effects. For the last decades, solid oral dosage forms have been the most popular way of drug administration (Gupta *et al.*, 2009). One way to obtain the desired release is to use a controlled release formulation like a pellet, containing a drug reservoir coated with a porous film. The porous microstructure of the pellet coating is controlling the mass transport of the drug from the core to the surrounding liquid in the stomach or intestine. By controlling the manufacturing and the formulation, and therefore the coating structure, the drug release rate can be controlled (Tiwari *et al.*, 2012).

Coatings made of porous phase-separated films are very effective in controlling mass transport (Marucci *et al.*, 2011) but the kinetics and mechanisms of structure formation in such films are not fully understood. Ethylcellulose (EC) and hydroxypropylcellulose (HPC) are two cellulose derivatives with established use in the pharmaceutical industry (Sakellariou and Rowe, 1995). Figure 1 is showing the formation of an EC/HPC film for drug delivery. Mixed with a common solvent *e.g.* ethanol, EC and HPC form a one-phase polymer solution at low polymer concentration. During solvent evaporation (see Figure 1), phase separation occurs, and a dry film is produced. EC is water-insoluble and HPC is water-soluble, and in contact with water the dissolution and leakage of the water-soluble HPC leads to the formation of a porous EC matrix through which the drug flows or diffuses (see Figure 1).

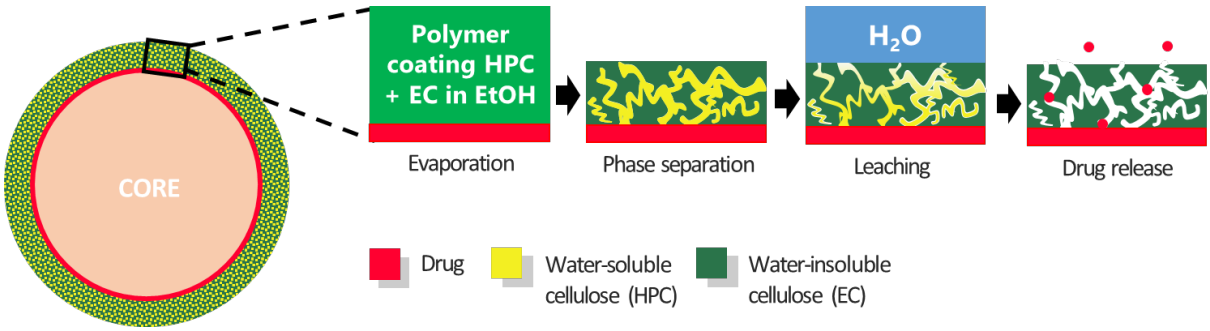

Figure 1 Formation of porous film made of EC and HPC for the delivery of drugs. From left to right, the different steps: evaporation of ethanol, phase separation and kinetic trapping, leaching of HPC and the release of the drug.

The 3D structure determines the transport through the porous network in phase-separated systems (Wassén *et al.*, 2014, Gebäck *et al.*, 2015). By controlling the process of phase separation, the film structure, and hence the mass transport can be tailored. The 3D structure and porosity, pore size distribution, pore shape and connectivity of EC/HPC films have been determined using Focused Ion Beam Scanning Electron Microscopy (FIB-SEM) and advanced image analysis (Fager, 2018, Röding *et al.*, 2021, Fager *et al.*, 2020a, Fager *et al.*, 2020b): the method allowed identification of central features of the porous network by quantification of channels where pore paths coincide. It was found that the interconnectivity and porosity increase with increasing amount of HPC. The effect of the molecular weight of EC and HPC

on the microstructure (Andersson *et al.*, 2013, Andersson *et al.*, 2009, Andersson *et al.*, 2011, Andersson *et al.*, 2016) and interactions of the film with water and its influence on permeability of both water and drug during leaching has also been investigated (Jansson *et al.*, 2014).

The coating of the EC/HPC films is nowadays made batch-wise in a spray-coating fluidized bed device to coat drug-containing pellets. One challenge is to relate the final properties of the polymer coating to the parameters of the industrial process used during production of coated pellets. During spraying, small droplets containing EC, HPC and ethanol are hitting, mixing, and coating the pellets, which influences the structure evolution of the phase-separated EC/HPC film. Many mechanisms are involved in the formation of the phase-separated films on the pellets, and they are competing in a complex, and time dependent manner. Examples of involved mechanisms are phase separation, kinetic trapping by viscosity increase, solvent evaporation, solvent quench, rewetting and mixing. This research focuses on understanding how all these mechanisms interact during the structure evolution and how the composition and process influence the final film structure.

2 Purpose and aim

The purpose of this work is to obtain a mechanistic understanding of the phase separation phenomenon in polymer mixtures and to increase the quality and robustness in the tailoring of thin EC/HPC film for pharmaceutical applications.

Specific aims are:

- To find a method to mimic the industrial process of spray drying and film formation in a controlled lab environment.
- To develop an experimental setup which allows observation *in situ* of the structure evolution and structure formation.
- To determine the kinetics of phase separation during solvent quenching and to understand the different mechanisms of phase separation and coarsening that influence the structure in a competing manner.
- To investigate the effect of composition and processing on the structure evolution and the final film structure.
- To understand the formation of multilayer structures in industrial pellets.

3 Background

In this section, the background of the study and the context of the research are established. First, the drug delivery systems and how phase separation can be used to make controlled drug release formulations are introduced. Second, we give an overview of the phase separation mechanisms in (bio)polymer mixtures. Then, some information about the biopolymers we use in this study, namely the two cellulose derivatives ethylcellulose (EC) and hydroxypropylcellulose (HPC) is given. Finally, we describe the industrial process of making drug delivery system coated with phase-separated EC/HPC films and introduce the challenges of mimicking such a process.

3.1 Controlled drug release in pharmaceutics

Drug delivery systems, referring to the ensemble of technologies for transporting a drug into the body to achieve a targeted therapeutic effect, have been used worldwide for decades to deliver pharmaceutics (Rhodes and Porter, 1998). Figure 2 summarizes the main goals and features of a drug delivery system. The main aim of a drug delivery system is to obtain an optimal treatment in the right location in the body (Klein, 2002) using a combination of active pharmaceutical ingredient (API) and release rate system. The delivery rate is critical, because the drug concentration in the blood must be within a certain interval. If the concentration is too low, the drug has no effect and if it is too high the drug can cause side effects and be poisonous. The location where the drug is released is also crucial for the functionality of the drug. In the case of oral dosage, the drug needs to be released in a particular zone in the gastrointestinal tract. The pH value varies between 1 and 5.5 in the upper part (stomach, upper intestine) and between 5.5 and 7 in the lower part (lower intestine, colon) (Rawlings and Lucas, 1985). Therefore, the pH must be considered when selecting materials for the delivery system. Other challenges when formulating a drug release system are the reduction of the amount of drug needed and the reduction of side effects (Hutton and Morris, 1992, Edsbäcker *et al.*, 2003).

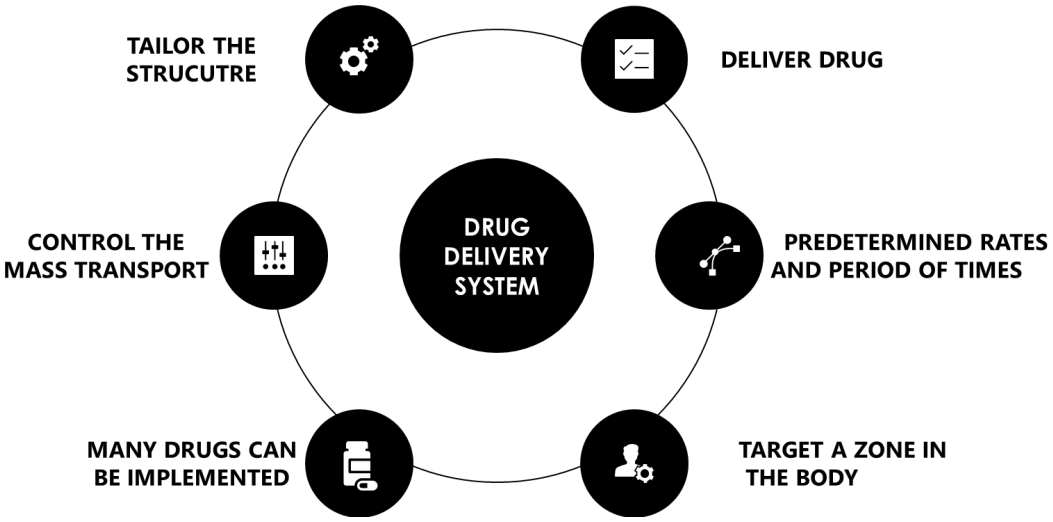

Figure 2 Drug delivery system objectives.

Conventional formulations, also called immediate release systems, give a rapid release of the drug, and can be obtained by several systems such as capsules, tablets, and pellets. Such

formulations are used where diseases or infections need acute drug delivery. However, when the release of the drug needs to be performed over a longer period and the delivery rate needs to be precise, controlled release formulations are used. Figure 3 shows the drug level in the blood for the two different types of release. In theory, the desired drug concentration (grey area) can be obtained with both releases systems. Conventional release can last if multiple doses are taken (blue dashed curve) however the controlled release (red curve) is more stable and fewer and more spaced out doses are needed.

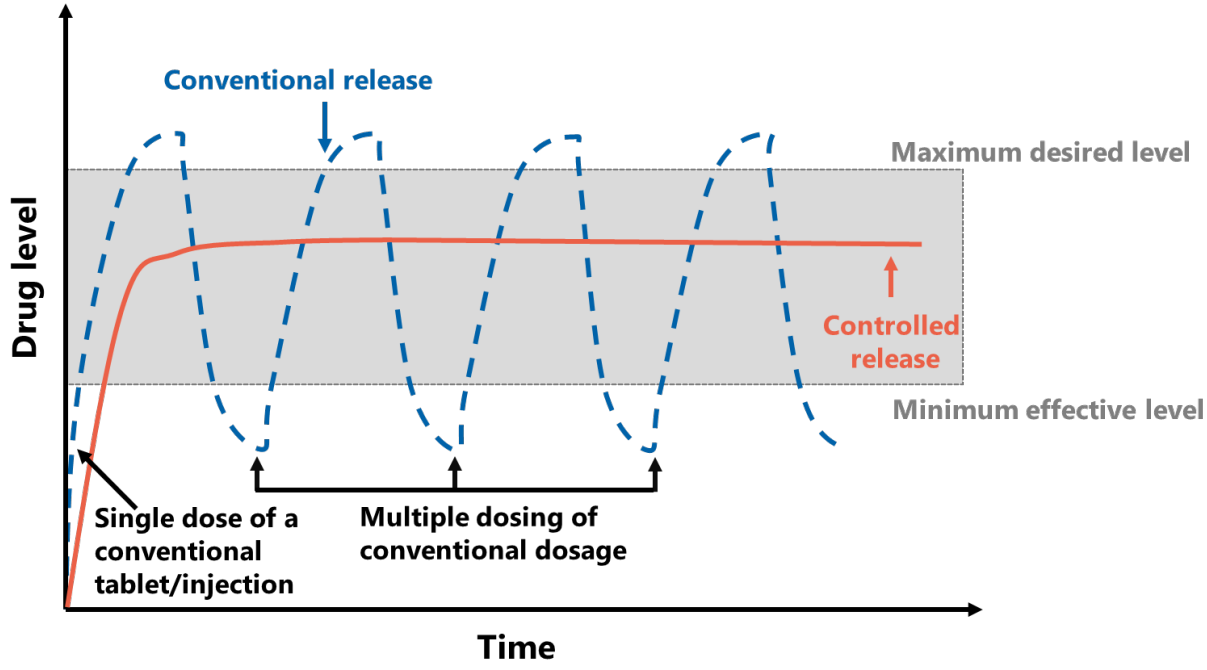

Figure 3 Drug levels in the blood released from: traditional release system, a combination of multiple oral capsules or injection dosing (blue dashed curve) and a controlled release system (red continuous curve). Adapted from (Huynh and Lee, 2015).

Soft materials and in particular polymers are often used for drug formulations. Both synthetic and natural polymers are used (Langer and Peppas, 2003). Natural polymers present the two enormous advantages to be highly accessible due to the huge number of sources, and to exhibit high affinity to biological tissue. Synthetic polymers need to be synthetized, but the synthesis can be controlled, and the properties can be more easily tuned. Examples of natural polymers are various types of cellulose derivatives. Like other polysaccharides they offer a range of possible chemical modifications and therefore modifications of material properties (Sakellariou and Rowe, 1995, Langer and Peppas, 2003).

For controlled release formulations two main approaches exist. Figure 4 shows the different approaches: the reservoir controlled release system where a coating encapsulates the drug, see Figure 4a, and the matrix controlled system where the drug is dispersed in the matrix, see Figure 4b (Langer and Peppas, 1983, Sershen and West, 2002). Compared to the reservoir system, the matrix system is not enveloped within a delivery rate limiting membrane. As such, the release rate of the drug from the matrix system is usually not constant and decreases in time. The most common matrix-based formulations use polymers which erode or dissolve with time as shown

in Figure 4b. The mechanisms of release for both approaches are mainly diffusion, dissolution, osmotic pumping and swelling (Sakellariou and Rowe, 1995, Langer and Peppas, 1983, Uhrich *et al.*, 1999). In the case of EC/HPC phase-separated film coating, the system is a reservoir-controlled release, and the mechanism is diffusion. The water-soluble polymer in the coating is leached out revealing a porous transport path through which the drug diffuses (see Figure 1).

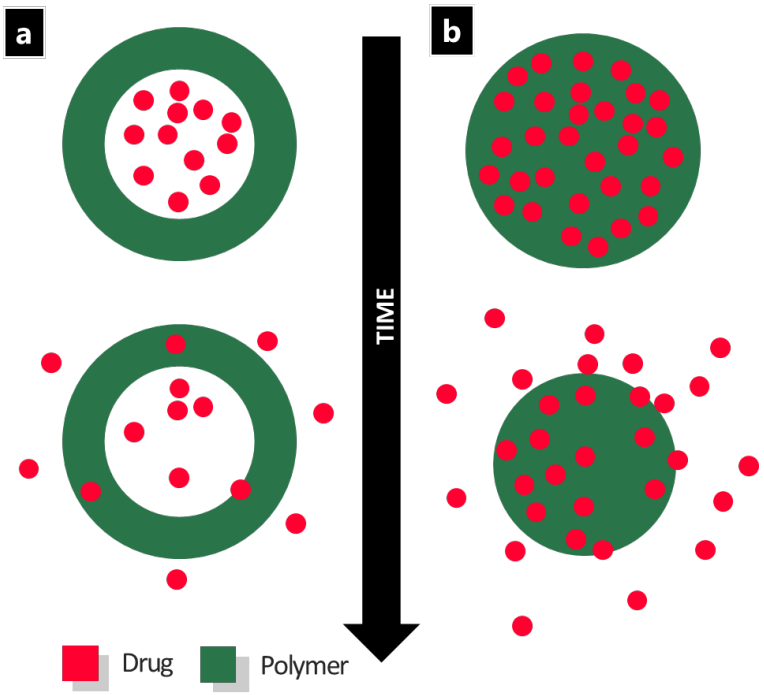

Figure 4 Schematic illustration of controlled release formulations systems, with a) a reservoir-controlled release system, and b) a matrix-controlled system. Adapted from (Stewart et al., 2018).

3.2 Phase separation of (bio)polymer mixtures

Phase separation is a general phenomenon of many polymer mixtures (Picullel *et al.*, 1995). By controlling the phase separation process, properties of high-performance polymers can be tuned. It allows changes of material characteristics, often leading to an improvement with respect to *e.g.* rigidity, toughness, chemical resistance, or abrasion. Phase separation can be initiated by a change in temperature (Jin *et al.*, 2015). It can also be triggered by evaporation and drying (removal of solvent), polymerization (Schaefer *et al.*, 2016, Petersson, 2005) , by change of pH or salt concentration (Firoozmand *et al.*, 2012) and by gelation and conformational ordering (Lorén *et al.*, 2001).

In polymer mixtures, phase separation is used mainly in separation and purification procedures with the manufacturing of films, fibers, membranes, and foams. In the pharmaceutical field, phase-separated polymer films are very effective in controlling the mass transport of drugs (Sakellariou and Rowe, 1995). Phase separation is also very common in the food industry. For example, phase-separated polymer mixtures can be used as fat replacement materials to control texture and consistency in food products (Clark, 1995). Another example is depletion-induced phase separation and gelation of xanthan and casein mixtures that gives the opportunity for controlling the stability, the microstructure and the mechanical properties (Mezzenga *et al.*,

2005).Viscoelastic phase separation in food is caused by incompatibility and viscoelastic forces, and it is used to control texture and stability of products (Tanaka, 2012). This type of phase separation occurs for instance in mixtures composed of *e.g.* globular protein, bovine serum albumin and an anionic polysaccharide, low-methoxyl pectin (Donato *et al.*, 2005). Phase separation in emulsions is also an important aspect in food science to form water/water/oil systems. For example, sodium caseinate is used as an emulsifying agent in dairy products or soy protein systems (Renkema, 2004).

3.2.1 The Gibbs free energy of mixing

Whether two polymers are mutually miscible depends on the composition and the shape of the Gibbs free energy of mixing curve (Gibbs, 1961, Jones and Richards, 1999). The system reaches a state of minimum free energy at equilibrium. Gibbs free energy (G) is a measure of the maximum available work that can be derived from any system under conditions of constant temperature (T) and pressure (P) and is an important thermodynamic quantity. Changes in Gibbs free energy is defined as $\Delta G = \Delta H - T\Delta S$, where ΔS is the changes in entropy and ΔH is the enthalpy from Flory–Huggins theory. The partial molar Gibbs free energy of mixing with respect to the solvent for the formation of a polymer solution is given by the following equation.

$$\Delta G_m = RT[\varphi_1 \ln \varphi_1 + \varphi_2 \ln \varphi_2 + \chi \varphi_1 \varphi_2]$$

where φ_i is the volume fraction of the component i, χ is the Flory-Huggins binary interaction parameter, R is the universal gas constant, and T is the absolute temperature. The first two terms of the right-hand side in the equation above, are related to the entropy of mixing, and the third term is originally assigned to the enthalpy of mixing.

3.2.2 Phase diagrams of (bio)polymer mixtures

Phase diagrams are useful for describing the status of a mixture. Figure 5 shows the different behavior regions for a typical polymer/polymer/solvent mixture (Tolstoguzov, 2003b, Tolstoguzov, 2003a). The binodal curve represents the transition from compatible one phase (region 1) to incompatible two-phase region (regions 2, 3 and 4). Going from region 1 to regions 2 and 3 occurs through NG; going from region 1 to area 4 occurs through SD (refer to section 3.2.3 Mechanisms of phase separation). Regions 2 and 3 represent the meta-stable regions and region 4 is the unstable region. The boundary between the unstable and the meta-stable regions is the spinodal curve. When phase separation occurs, the process does not stop before the compositions in each phase have reached their equilibrium concentrations. These compositions are located along the binodal curve. They are connected through the tie line that passes through the original composition and the equilibrium compositions of each phase in the phase diagram. Note that even after reaching equilibrium, the concentrations will never be 100% of any of the components for entropic reasons.

Figure 6 shows a typical ternary phase diagram, used to describe a ternary system consisting of two polymers and a solvent. In the diagrams, two regions are described: the 1-phase region where the mixture is one homogeneous phase and the 2-phase region where the mixture is separated in two distinct phases.

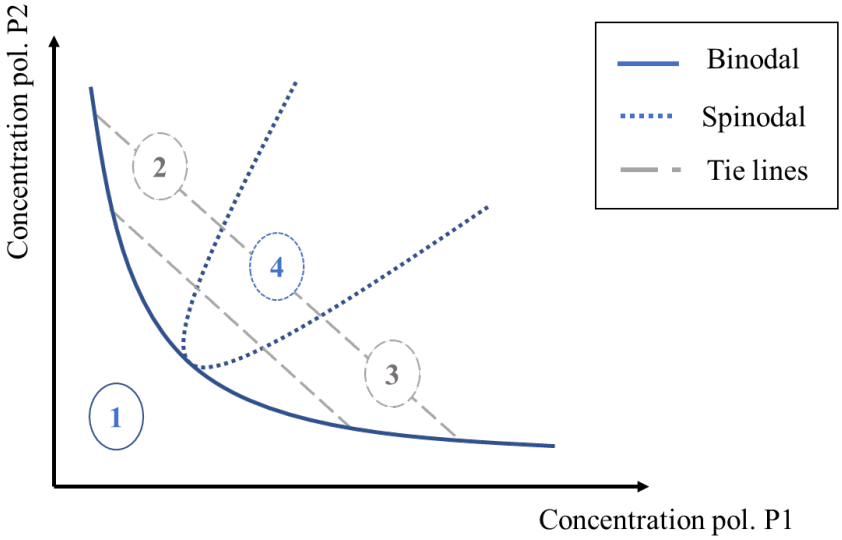

Figure 5 Schematic phase diagram of solvent/ polymer/polymer system. Areas: 1, one phase solution; 2 to 4 phase-separated morphologies. Adapted from (Tolstoguzov, 2003b).

Depending on the types of interactions that occur between the polymers in solution, an associative or a segregative phase separation can occur (Picullel *et al.*, 1995). During associative phase separation (Figure 6a), both polymers are enriched in one phase and depleted in the other phase. During segregative phase separation (Figure 6b), each phase is enriched in one of the polymers. Solvent partitioning is taking place when the polymer A or B has stronger affinity with the solvent, in this case the solvent will not be equally distributed between the phases enriched in polymer A or B. The type of assembly of the components in the system is governed by the free energy of mixing (Jones and Richards, 1999) (refer to previous section 3.2.1).

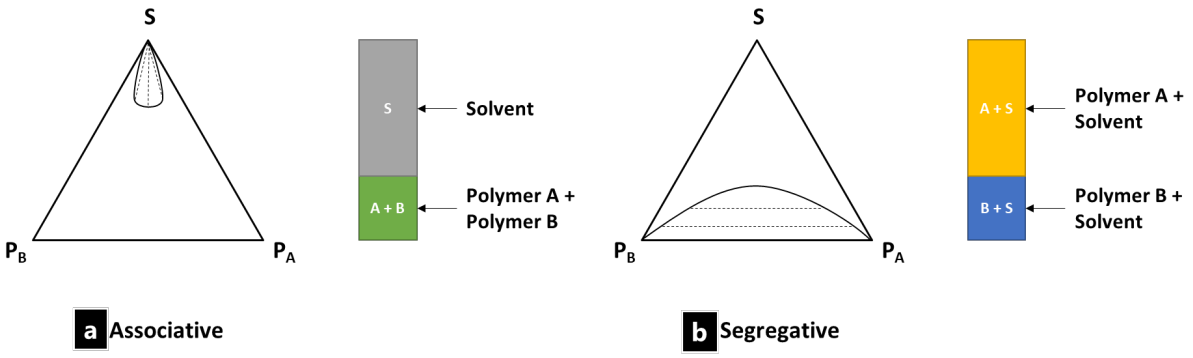

Figure 6 Ternary phase diagram with a) associative phase separation and b) segregative phase separation.

Temperature and composition are two key parameters influencing incompatibility. Figure 7 shows a phase diagram of a ternary polymer mixture composed of two polymers in a solvent, (Clark, 1995) with the temperature *versus* the composition of polymer A ($x_A = 1 - x_B$), where x_i is the composition of the polymer i. In the diagram, the separation between the compatible one-phase region and the incompatible two-phase region is represented by the binodal curve whereas the spinodal separates the metastable region from the unstable region in the

incompatible region. The binodal and the spinodal coincide in only one point: the critical point (x_{cr} and T_{cr}).

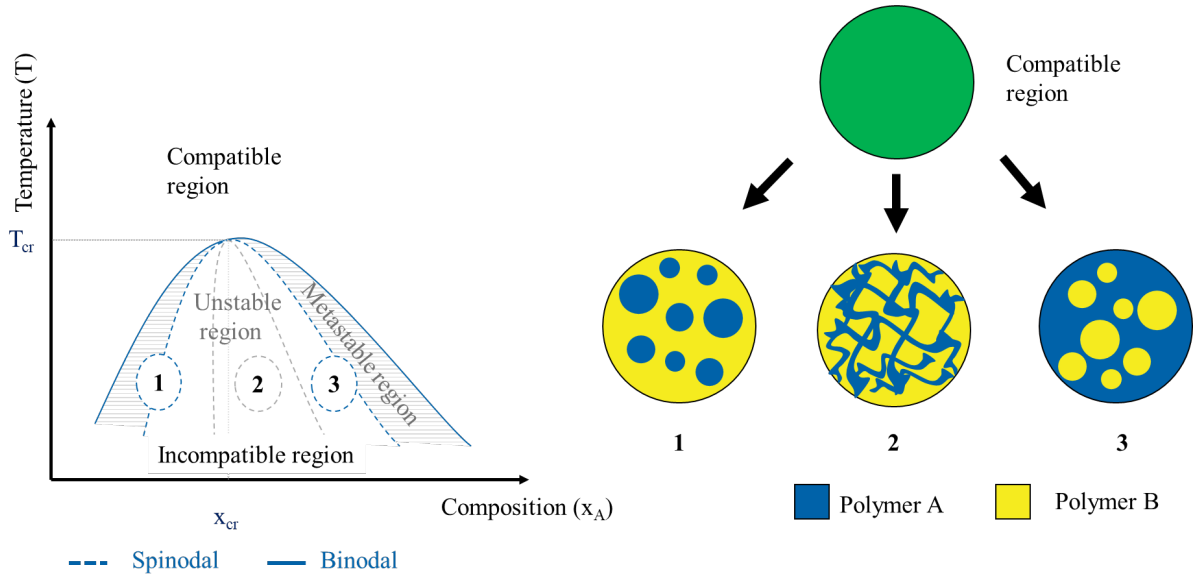

Figure 7 Schematic temperature-composition phase diagram of a ternary polymer mixture composed of two polymers and a solvent. Tcr and xcr are the critical temperature and composition at the critical point. Adapted from (Jones and Richards, 1999).

In Figure 7, compositions inside the meta-stable region, separate according to the NG mechanism, whereas those within the unstable region separate through the SD mechanism. Morphology 1-3 is a droplet like structure mainly initiated by NG mechanism. Morphology 2 is a periodically modulated structure caused by a SD phase separation (see section 3.2.3 for the explanation about NG and SD).

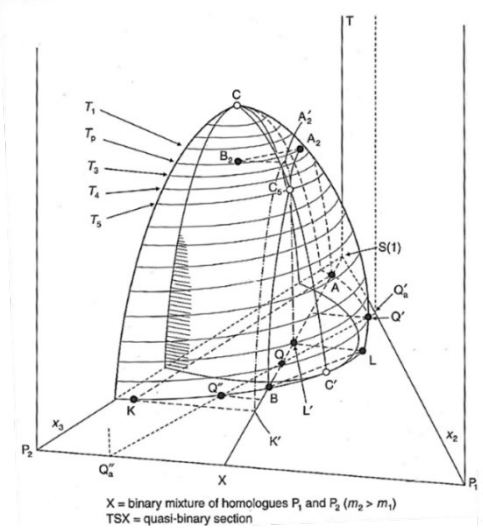

Figure 8 Illustration of the binodal and spinodal in a ternary system at constant pressure. The spinodal plane is partly hatched.(Koningsveld et al., 2001).

However, a ternary phase diagram is established for one constant temperature and pressure. For example, temperature is not described in the ternary diagram shown in Figure 6. Therefore, for the same mixture, the phase diagram is varying as a function of temperature. Some systems exhibit a UCST-behavior (upper critical solution temperature) and some an LCST-behavior

(lower critical solution temperature). Eventually, the binodal becomes a circle and then a point, and thus there is an upper temperature limit (UCST). To describe the spinodal and the binodal in ternary systems composed of two polymers and a solvent, a three-dimensional ternary phase diagram can be used. In this case, the binodal and the spinodal regions are represented with planes (Figure 8).

3.2.3 Mechanisms of phase separation

There are two main phase separation mechanisms in polymer mixtures: Spinodal decomposition (SD) and Nucleation and Growth (NG). The binary phase diagram in Figure 7 shows for which composition the mixture has been separated with either mechanism: the composition values within the metastable region separates according to the NG mechanism while the composition values within the incompatible region separates trough the SD mechanism.

3.2.3.1 Nucleation and growth

Nucleation and growth describes the formation of a heterogeneous structure from a homogenous structure, initiated by a nuclei (Gibbs, 1961). In the phase diagram, when the polymer mixture ends up in the metastable region, the NG will appear (Das, 2014). Figure 9 shows the different steps of a general case of NG: step I) when the concentration increases over a certain level denominated as C_{nuc} in Figure 9 ; step II) a nuclei is formed; step III) the growth takes place at the surface of the nuclei until reaching the equilibrium concentration C_{eq}.

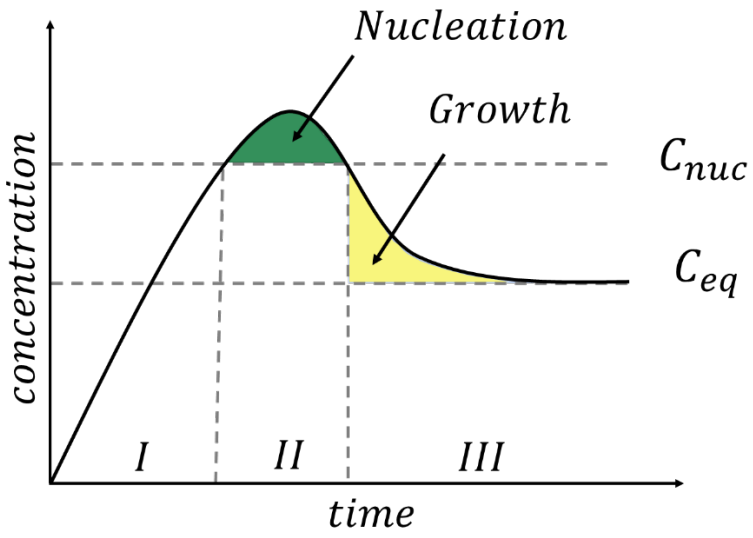

Figure 9 Homogeneous nucleation and growth mechanism. C_{nuc} is the minimal concentration for nucleation. C_{eq} is the concentration at equilibrium. Adapted from (Ottesen, 2011).

During polymer phase separation, NG can be associated with the formation of irregular sized droplets that grow bigger as a function of time. In addition, the occurrence of the droplets is distributed in time (Sagui and Grant, 1999, Debenedetti, 2000). Most of the time NG is heterogeneous: when foreign particles act as nucleating agents and induce the phase separation, the growth is taking place by addition of constituents from the bulk. More rarely, homogenous

NG can occur, where droplets are formed by concentration fluctuations that overcome the energy barrier and attain the equilibrium state (C_{eq} in Figure 9) in which they remain. For a polymer mixture, the NG-type phase separation leads to a droplet-like structure (Tanaka and Nishi, 1985) (see morphology 1 and 3 in Figure 7).

3.2.3.2 Spinodal decomposition

Spinodal decomposition is a mechanism for rapid unmixing of a mixture of liquids or solids from one compatible phase to two coexisting phases. SD is characterized by a periodicity in domain formation, or equivalently as having a characteristic wavelength L(t) (see Figure 10 d). In general, SD is initiated by small fluctuations in concentration within the blend, reducing the free energy of mixing (Jones and Richards, 1999).

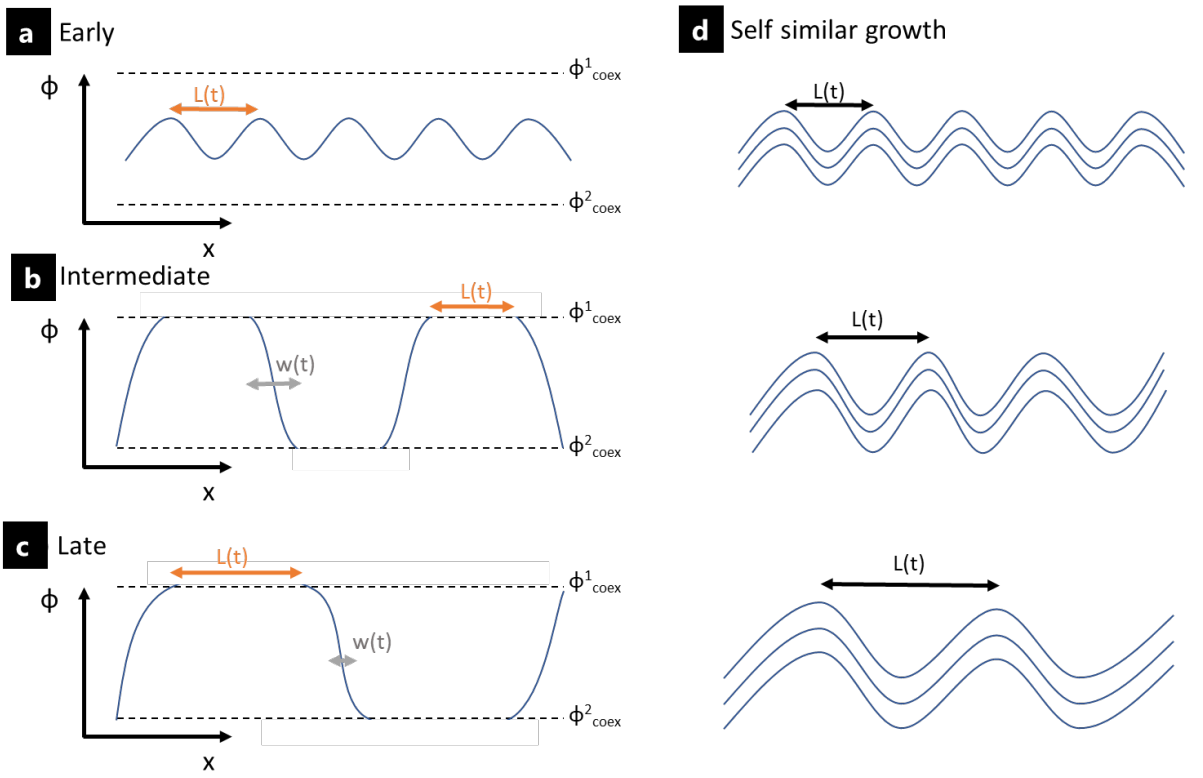

Figure 10 Time-dependent structural evolution of the domain size as a function of time through the (a) early, (b) intermediate, and (c) late stages of the spinodal decomposition mechanism d) Illustration of self-similar growth during spinodal composition. Adapted from (Hashimoto, 1988).

Figure 10 shows the successive steps of SD. Initially an interconnected structure will be formed, then the SD goes through three stages: an early stage, see Figure 10a, an intermediate stage, see Figure 10b, and a late stage, see Figure 10c. In the early stage, the concentration fluctuations are present at different length scales and therefore grow at different rates (Hashimoto, 1988). The wavelength selection mechanism (Cahn, 1965) makes the concentration fluctuations with an intermediate wavelength predominate. Fluctuations with short wavelengths exhibit a sharp concentration of gradients which make them energetically not preferable. Fluctuations with long wavelengths grow very slowly due to the large distances, material has to be transported. The values of the domain sizes $L(t)$ and interfacial width $w(t)$

evolve through the SD process. At the early stage, $L(t)$ and $w(t)$ remain constant, only the amplitude increases. In the intermediate stage, the amplitude reaches its maximum (the maximum corresponds to the equilibrium concentration, ϕ_{coex} in Figure 10), the domain size $L(t)$ increases while the interfacial width $w(t)$ starts to decrease towards the equilibrium. During the late stage of SD the entire system is brought to equilibrium, $w(t \rightarrow \infty) = w_{eq}$ and the system evolves solely by self-similar growth (Binder and Stauffer, 1974).
Simultaneously with the phase separation, a secondary, also called double, phase separation can occur at a different scale inside a phase-separated domain (Tanaka, 1994, Tanaka and Araki, 1998). The same mechanisms are taking place into a subvolume of mixture. For some polymer mixtures, cell-like and necklace-like morphology can be observed during SD (Yamamura *et al.*, 2002).

3.2.4 Coarsening of phase-separated structures and time dependency

With SD in bulk, the system can evolve to a bicontinuous structure where the polymer phases are interconnected, or to a discontinuous morphology where droplets of one polymer are distributed in the other polymer phase without connection between them.
The growth of these possibilities (interconnected phases or discontinuous morphology) phase-separated (bio)polymer mixtures are governed by different coarsening mechanisms: hydrodynamic growth (Siggia, 1979), droplet coalescence (Chesters, 1991) and Ostwald ripening (De Gennes *et al.*, 2004, Hill, 1995). The three mechanisms are illustrated in Figure 11.

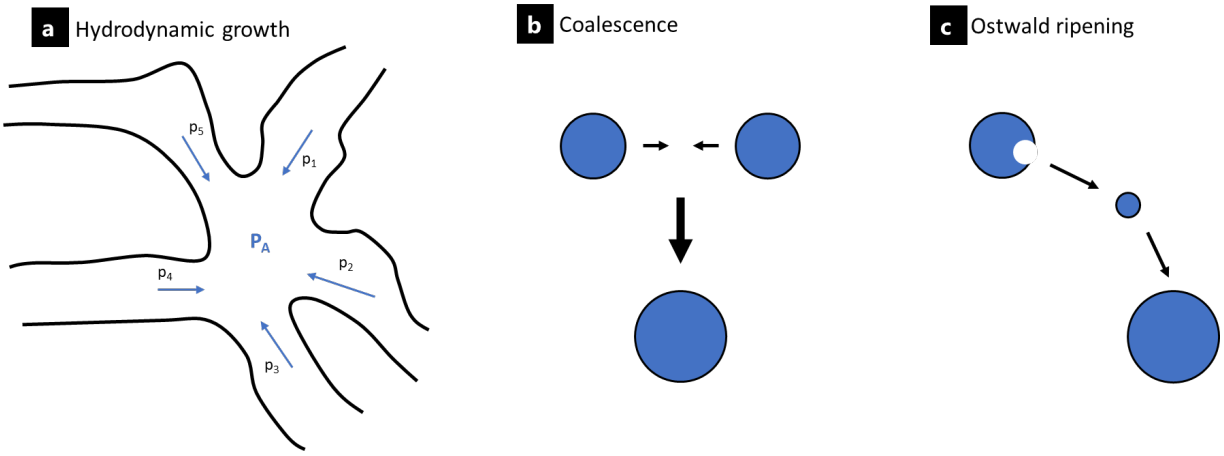

Figure 11 Illustration of the three coarsening mechanisms, (a) hydrodynamic growth, (b) coalescence, and (c) Ostwald ripening.

Hydrodynamic growth takes place within the bicontinuous structure (interconnected phases) due to differences in Laplace pressure. The Laplace pressure $p_{Laplace}$ (Solon *et al.*, 2018) is proportional to the product of the surface tension γ and the curvature $\frac{1}{R}$: $p_{Laplace} \sim \frac{\gamma}{R}$. The pressure gradient ($p_{1\text{-}5} > P_A$) between the thinner arms (regions with high curvature) and the thicker area (region with smaller mean curvature) causes a Poiseuille flow of material from the outside arms to the inner thicker areas.

During coalescence of discontinuous structures, the droplets merge to form new larger droplets (Chesters, 1991). After the creation of a connecting bridge between the two surfaces of the droplets, the speed of the coalescence results in a competition between the capillary forces in favor of the merge and the viscous forces slowing it down (Aarts *et al.*, 2005). The transport of material during coalescence can be induced by Brownian motion, concentration gradients, or by collision-induced phenomena (Bray, 2003).
During Ostwald ripening, smaller droplets feed larger droplets that grow and expand. Both coalescence and Ostwald ripening are governed by diffusion.

All these growth mechanisms are time dependent, and the characteristic length scale growth is obeying a power law so that $L(t) \sim t^n$ where t is the time. The exponent n depends on the mechanisms of phase separation taking place and particularly on the importance of the hydrodynamic interaction (Dhont, 1996). Bray *et al.* (Bray, 2003, Bray, 2010) studied this exponent and found two regimes: the diffusive regime, and the hydrodynamic regime, where the exponent n is equal to:

$$n = \begin{cases} \frac{1}{3} & diffusive\ regime \\ 1 & hydrodynamic\ regime \end{cases}$$

For example, for a diffusion-controlled coarsening, a diffusion-based model predict that the growth evolves as: $L(t) \sim \left(\frac{\gamma D \Omega}{kT} t\right)^{\frac{1}{3}}$, where D is the effective molecular diffusivity, Ω a molecular volume, k the Boltzmann constant and T the temperature (Bray, 2010). The hydrodynamic growth in Figure 11a is driven by interfacial tension mechanism ($n = 1$) whereas Ostwald ripening in Figure 11c and coalescence in Figure 11b are diffusion driven ($n = 1/3$) (K. Haas and M. Torkelson, 1997).
Those mechanisms are often taking place one after the other: in early times the hydrodynamics effect are negligible and we have a diffusive regime, during intermediate and late times we have a hydrodynamic regime (Bray, 2003, Furukawa, 1985). Experimentally the coarsening rate was studied (Bailey *et al.*, 2007, Lorén *et al.*, 2001) and two regimes were identified: at small length scale the exponent was 1/3 (diffusive regime) and at large length scale the exponent was 1 (hydrodynamic regime). It was also shown that the cross-over between the two regimes happens at a particular length scale. For circular shape the length scale can be identified with the radius, and the cross over happens at the critical radius value $R_c = \sqrt{2k/\gamma_0}$ with k the bending rigidity and γ_0 the interfacial tension (Scholten *et al.*, 2004). The study of the exponent n is a good indicator of which coarsening mechanism is prominent (Bouttes *et al.*, 2015).

3.2.5 Influence of solvent evaporation on phase separation

The polymer phase separation can be initialized by solvent evaporation, also called solvent quenching. The evaporation leads to a huge increase in the viscosity of the polymer mixture retarding and eventually halting the coarsening, kinetically trapping the structure in a non-equilibrium stage (Schaefer *et al.*, 2016). Phase separation induced by solvent evaporation induces extra challenges since the solvent evaporation continuously changes the state of the

mixture and the influence on the structure evolution is not fully understood (Schaefer *et al.*, 2015). In the case of solvent-quenched systems, several studies have shown that faster evaporation leads to smaller features in the final dried structures (Kouijzer *et al.*, 2013, van Franeker *et al.*, 2015, Walheim *et al.*, 1997). The characteristic length scale of the phase-separated structure depends on the coarsening time but also on the time-dependent depth of the solvent quench (Schaefer *et al.*, 2015, Schaefer *et al.*, 2016). During solvent evaporation, the depth of the solvent quench changes continuously, which will influence the characteristic length scale. With deeper solvent quench the characteristic length scale is expected to become larger.

Previous work has been performed on phase separation during solvent evaporation of thin films. For example, Cummings *et al.* modelled solvent evaporation during thin film formation in phase-separating polymer mixtures (Cummings *et al.*, 2018). It was demonstrated that kinetical trapping resulting from concentration dependent mobility can lead to rougher films. De Gennes studied the instabilities that may occur at the surface of the film when the thickness is too low (De Gennes, 2001) or during the formation of a crust (De Gennes, 2002).
Buxton *et al.* have simulated the evolution of a polymer blend solution undergoing solvent evaporation and phase separation as the system is moved from the one-phase to the two-phase region of the ternary phase diagram (Buxton and Clarke, 2007). They predicted that phase separation occurs initially at the air-film surface where solvent concentrations are the lowest and then progressively propagates down through the film.
Zoumpouli *et al.* examined the effects of hydrodynamics on polymer phase separation morphologies in thin films formed during evaporation (Zoumpouli and Yiantsios, 2016). They used Cahn-Hilliard and Flory-Huggins theories to describe the free energy of the phase-separating systems. In particular, they investigated the effects of parameters characterizing the evaporation rate and the preferential wetting of the solutes at the air interface. For example, for systems exhibiting preferential wetting, they showed that diffusion alone favor lamellar configurations for the separated phases in the dried film.

3.2.6 Phase separation in spin-coated thin films

Spin-coating is a broadly used technique for producing uniform, thin polymer films (Fowler *et al.*, 2016, van Franeker *et al.*, 2015, Heriot and Jones, 2005). There has been an increasing interest in this technique due to the possibility of obtaining a broad range of different morphologies and hence the ability to tailor the structure (van Franeker *et al.*, 2015). The spin-coated, phase-separated structure depends on the transition from a one-phase state of two immiscible polymers in a common solvent to a two-phase state during evaporation of the solvent (Toolan *et al.*, 2013). Figure 12 shows the schematic principle of phase separation during spin-coating. First, the casting solution is deposed in excess on the substrate. Then the spinning leads to the formation of a thin film due to that the excess is projected onto the outside walls of the spin-coater. Subsequently, the evaporation of the solvent triggers the phase separation.

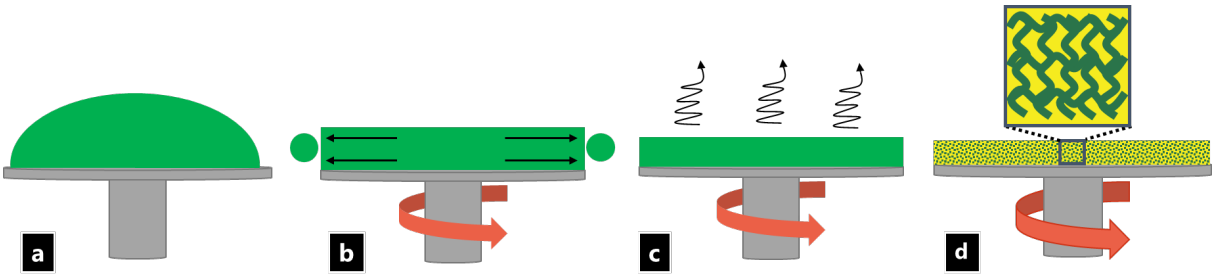

Figure 12 Schematic principle of spin-coating with the different steps a) deposition of liquid sample b) spinning and film formation c) evaporation, d) drying of the solution and phase separation.

It has been demonstrated experimentally that the final morphology of the phase-separated film depends on a wide range of factors including properties of the polymers (molecular weight (Li *et al.*, 2004), solubility (Walheim *et al.*, 1997), surface tension, and viscosity) properties of the blended solution (solid content (Dunbar *et al.*, 2010), solvent properties (Walheim *et al.*, 1997), blend ratio), and properties of the substrate (chemistry (Walheim *et al.*, 1997), roughness, size and shape). Along with the polymer and substrate features, the final morphology also depends on the spin-coating parameters such as spin speed (Fang *et al.*, 2010), acceleration, spin time, and the surrounding atmosphere (Mokarian-Tabari *et al.*, 2010b).

Toolan *et al.* (Toolan and Howse, 2013) recently developed an *in situ* method for studying the phase separation of PS/PMMA systems (polystyrene/poly(methyl-methacrylate)) synchronizing stroboscopic LED illumination with a highly sensitive electron-multiplying charge coupled device camera (EMCCD) connected to an optical microscope. They proposed a two-step mechanism for the phase separation during spin-coating: a hydrodynamic thinning (flow dominated step) followed by a solvent thinning (solvent evaporation dominated) step. They determined the influence of the spin-coating parameters on the final morphology of the film. Furthermore, a relationship between characteristic length scale and thickness has been demonstrated for thin films made of synthetic polymers (Schaefer, 2016, Williams *et al.*, 2013, van Franeker *et al.*, 2015, Muller-Buschbaum and Stamm, 2001). In addition, a wide range of models have been proposed to explain the experimental observations such as vertical solvent gradient (Buxton and Clarke, 2007), Marangoni instabilities (Scriven and Sternling, 1960) and stratification during spin-coating. However, information about this relationship in mixed biopolymer systems such as mixtures of EC and HPC is lacking.

3.2.7 Influence of surface on phase separation

During phase separation the system can go through several phenomena, related to the surface. In general, phase separation is never surface-free, and depending on the special affinity of either phase, the phase separation can be perturbed by the surface.
One possible phenomenon is the wetting. It happens by preferential wetting of solid surface by one or several components of a complex mixture (Jasnow, 1984, De Gennes, 1985). It can affect the development and the kinetics of the phase separation and the coarsening, independently of whether the obtained structure is bicontinuous or discontinuous.

In addition, Tanaka pointed out that it could also induce a secondary phase separation (Tanaka, 2001) and demonstrated that hydrodynamics plays a role in the evolution of phase-separating fluid mixture interacting with solid surfaces.
Figure 13 shows the two possible types of wetting behaviors in a capillary (2D confinement) at equilibrium: the complete wetting is a layered structure; and the partial wetting is a droplet-like structure. In Figure 13, the α-phase has more affinity with the solid surface than the β-phase. In other terms, it is energetically more favorable for the α-phase to wet the surface.
Tanaka discussed the hypothesis of having different types of coarsening depending on wettability strength: a 3D growth for weak wettability and a 2D growth for strong wettability.

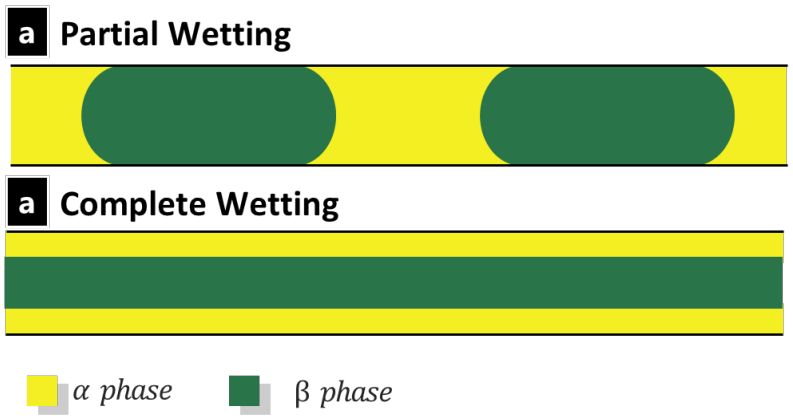

Figure 13 Final equilibrium structures for (a) partial and (b) complete wetting. Here the α-phase is more able to wet the solid wall than the β-phase. Adapted from (Tanaka, 2001).

Wassen *et al.* studied the effects of confinement on the phase separation kinetics and compared the effect of wetting in bulk and in confined environment (Wassén *et al.*, 2013). They emphasized the importance of quantifying the impact of confinement on phase separation in order to control the final microstructure. For example, Wiltzius *et al.* (Wiltzius *et al.*, 1994) studied the influence of wetting on the time dependency of the coarsening mechanisms (see section 3.2.4 Coarsening of phase-separated structures and time dependency). Using light scattering, they studied the phase separation of a fluid mixture at a glass interface and in bulk. Because of the formation of a wetting layer parallel to the surface, they found that at the substrate interface, the power law exponent was higher than in the bulk; and the coarsening, faster than in the bulk.

3.3 The EC/HPC system and phase separation

3.3.1 Cellulose and derivatives

3.3.1.1 Cellulose

Cellulose is a polysaccharide and the principal component of the primary cell wall of green plants. Cellulose is the most abundant organic polymer on Earth (Khandelwal and Alan, 2013). In industry, cellulose is mainly used to produce paper and is extracted mainly from wood pulp and cotton. As a polysaccharide, cellulose is composed by D-glucose units (see Figure 14) linked by β(1→4)-glycosidic bonds forming a linear chain. The numerous hydroxyl groups on

each unit form hydrogen bonds with neighboring chains forming crystalline regions and making native cellulose, a rigid, highly oriented and highly crystalline polymer (Klemm *et al.*, 2005). Substitutions of these hydroxyl groups can produce cellulose derivatives with a wide range of properties.

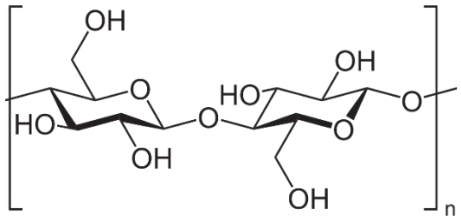

Figure 14 Chemical structure of cellulose repetitive unit (Klemm et al., 2005).

3.3.1.2 EC and HPC

Etherification and esterification (Fox *et al.*, 2011) of cellulose can be used to produce ethylcellulose (EC) and hydroxypropylcellulose (HPC). The average number of substituted hydroxyl groups per glucose unit is referred to as the degree of substitution (DS). Complete substitution is obtained with a DS of 3. In general, the nominal viscosity is the parameter used to characterize the grade of EC and HPC. It gives an indication of the average Mw of the batch. For EC it is often provided in the grade name and expressed in centipoises (cPs). Due to the strict regulation on pharmaceuticals, the grade and the Mw must be specified for each batch.

3.3.1.2.1 Hydroxypropylcellulose

Hydroxypropylcellulose (see Figure 15) is an ester of cellulose, which means that some of the hydroxyl groups of the repeating glucose units have been transformed into hydroxypropyl groups. HPC is prepared by reacting alkali cellulose with propylene oxide. Cellulose is a very crystalline (bio)polymer and not soluble in water.
However, HPC is highly soluble in water at room temperature due to the large number of hydrophilic groups (Sakellariou and Rowe, 1995). HPC molecular mobility and chain orientation make it difficult to determine the glass transition temperature (T_g) with accuracy. However, a T_g of 124°C has been proposed for HPC (Sakellariou *et al.*, 1985). The solubility of HPC in its solvent is enhanced by the hydrogen bonds and therefore HPC-solvent system exhibits a lower critical solution temperature (LCST) between 40-45°C. Above this temperature, HPC is no longer soluble in water and form a crystal solvate of six water molecules per unit of HPC (Fischer *et al.*, 1995). HPC has been used in pharmaceutical applications to form tablets (Picker-Freyer and Dürig, 2007), coatings (Huang *et al.*, 2013) and as ophthalmic inserts for treatments of dry eye syndrome (Nguyen and Latkany, 2011). Due to the mix of hydrophilic/hydrophobic parts, HPC is often absorbed at air/water interfaces or oil/water interfaces. In food industry, it has been used as emulsifier and as bubble stabilizer in bread (Andersson *et al.*, 2011, Schober *et al.*, 2008).

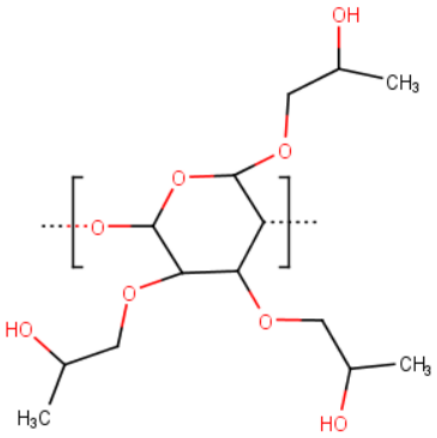

Figure 15 Chemical structure of hydroxypropylcellulose repetitive unit.

3.3.1.2.2 Ethylcellulose

Ethylcellulose (see Figure 16) is an ether of cellulose where the hydroxyl groups on the glucose units of cellulose have been converted to ethyl ether groups. EC is produced by reacting alkali cellulose with an appropriate alkyl halide (Klemm *et al.*, 2005). With its high glass transition temperature (T_g = 124-132°C (Sakellariou *et al.*, 1985)), EC is used as a plasticizer in coatings for example to improve the mechanical properties and the thermal behavior. At room temperature, EC is totally insoluble in water due to the large number of hydrophobic groups. However, it is soluble in ethanol and to some extent in ethanol-water mixture.

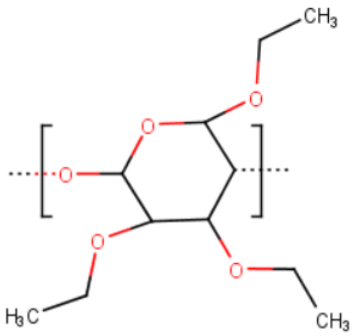

Figure 16 Chemical structure of ethylcellulose repetitive unit.

3.3.2 Phase separation in EC/HPC mixtures

EC and HPC can be dissolved in ethanol. During ethanol evaporation, the polymer blend concentration increases, and the mixture becomes incompatible and starts to phase separate. The phase separation results in an enrichment of the polymers in two separate phases (see Figure 7). This is called segregative phase separation (Picullel *et al.*, 1995). When the evaporation of ethanol is complete, a kinetically trapped, phase-separated film of EC/HPC remains.

3.3.3 EC/HPC systems for drug delivery

The presence of the water soluble HPC in the phase-separated film of EC and HPC is a good feature for the delivery of drug. Immersion of such film in an aqueous media (*e.g.* body liquids)

leads to a leaching of HPC and the formation of pores in the EC matrix. Through these pores the drug can be released and subsequently, permeability of the film can be defined.

By tailoring the structure of the pores, the drug delivery rate can be controlled. Several studies were performed to find a method to regulate the pore shapes in the final film. Several key parameters were identified: the polymer blend ratio in the initial mixture between EC/HPC and the solvent (here ethanol).

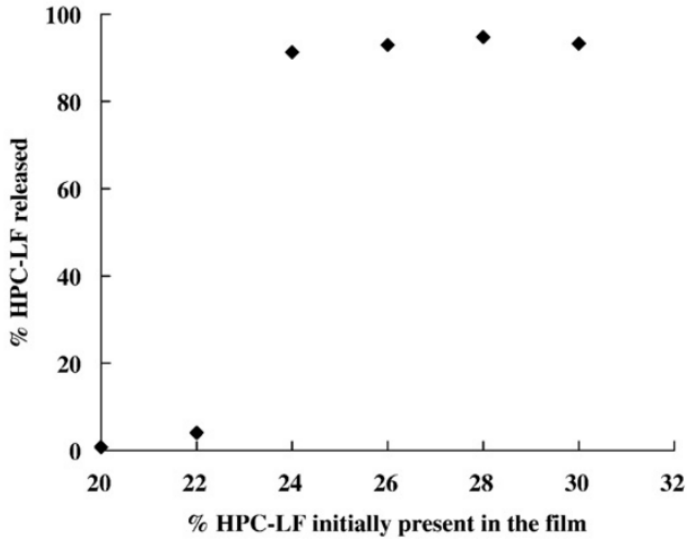

Figure 17 HPC-LF leached from EC/HPC-LF films after 24h exposure to phosphate buffer solution at pH 6.8 under well-stirred conditions. (Marucci et al., 2009).

Previous works have shown that the structure of EC and HPC in the film and its properties depend on numerous parameters such as the EC:HPC ratio, the molecular weight distribution of EC and HPC (Andersson *et al.*, 2009, Andersson *et al.*, 2013), and the coating processing parameters (temperature, gas flow, spray rate) (Marucci *et al.*, 2009). Differences were observed in the microstructure, in water and solute permeability, in drug release rate and release rate of HPC. It was found that a higher molecular weight of HPC results in a lower permeability (Andersson *et al.*, 2016). Marucci et al. (Marucci *et al.*, 2009) studied permeability and leaching of EC/HPC films with different compositions. They discovered the presence of a percolation onset at about 22 wt% HPC (see Figure 17). When the HPC ratio exceeded 22 wt%, both the amount of HPC leached out and the water permeability of the films increased linearly with the HPC ratio up to a certain concentration of HPC (Fager, 2018, Andersson *et al.*, 2009, Marucci *et al.*, 2009, Jarke, 2009, Marucci *et al.*, 2011).

For each (bio)polymer system, the phase diagram must be determined for a given temperature and pressure. The system of interest in this study is EC/HPC in ethanol and the grades selected are HPC-LF and EC-10cps. Figure 18 shows the phase diagram for these specific grades of EC and HPC elaborated at atmospheric pressure for two temperatures: 25°C (Figure 18 b) and 50°C (Figure 18 a) (Baderstedt, 2011). Baderstedt *et al.* let EC/HPC solutions rest in vials for at least one month and performed a visual inspection of the meniscus to determine if the solution was one phase or phase-separated.

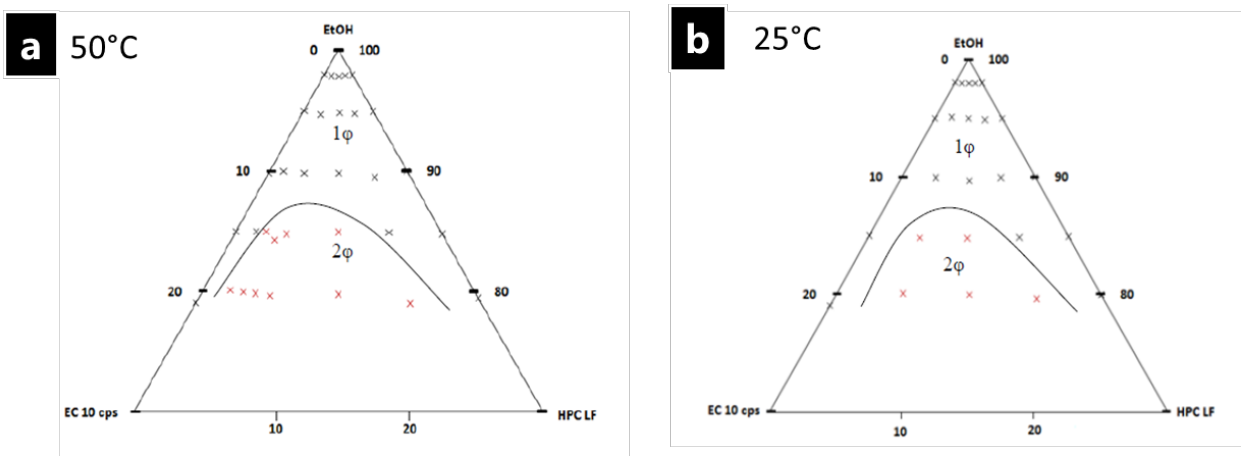

Figure 18 Ternary phase diagrams of EC 10cps and HPC-LF in ethanol at 25°C and 50°C. The red dots represents the samples that have phase-separated, whereas the lines are suggestions for binodal lines. (Baderstedt, 2011).

3.3.4 Industrial process of spray-coating

Pellets used for drug release are often made using a spray coating fluid bed device. In this device, the pellets are circulating through the spraying zone and then back to the bottom of the device. The polymer mixture is in one phase state and the mixture is sprayed onto the pellets in the spraying zone. A large number of small droplets are hitting the pellet and they form a coating onto the core. With the ethanol evaporation, the mixture starts to phase separate and the film structure for the drug release is formed. Figure 19 shows the coating process and the pellet travel in the device. Thanks to the gas circulation (nitrogen with ethanol) the particles go from the bed to the spraying cone, and back in the bed in a chaotic trajectory. The pellets will pass through the spraying zone many times during the processing. Consequently, the pellets perform a cycle with spraying, phase separation and drying, which is repeated.

Pellets consisting of microcrystalline particles were sprayed using the spray coating spouted bed device. These pellets were analyzed using a FIB-SEM technique, allowing the characterization of the coating structure in terms of connectivity and tortuosity (Fager, 2018, Fager *et al.*, 2020a). According to this recent study, EC/HPC coating structure after spraying and leaching of the water soluble HPC, takes the form of a superposition of layers. Those findings have inspired the thoughts that the droplets have been distributed on the surface and a thin layer is deposed for each passage in the spraying cone. One hypothesis is that a large number of droplets is hitting the particle and is spread all over the surface while the particle is spinning due to the air circulation .

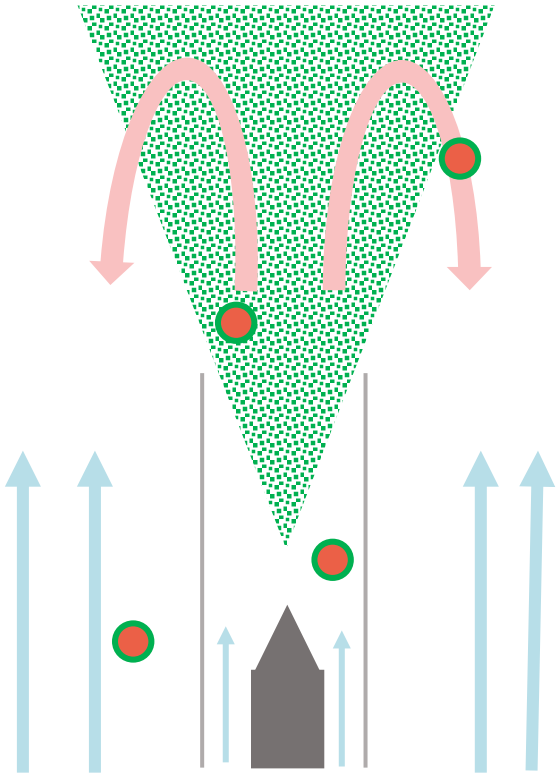

Figure 19 Illustration of the industrial process of spray-coating, with the pellets (in red) and the spraying cone (doted green) going out from the spraying nozzle (grey). The air circulation (blue arrows) and the movements of the particles (red arrows) in the device are represented.

4 Experimental

In this section the material and methods used in this work are described. First, the preparation of the EC/HPC solutions for the different experiments is explained. Then, the principle of spin-coating, confocal scanning laser microscopy, rheology and profilometry are addressed. Finally, the image analysis methods are described.

4.1 Preparation of EC/HPC solutions

Solutions of HPC (Klucel Pharm HPC, grade LF, Ashland Inc, Covington, Kentucky, USA) with a mean molecular weight of 95 kDa (Ashland, 2017) and EC (Ethocel Standard Premium, viscosity 10 cps, Dow Cellulosics, Dow Chemical Company, Midland, Michigan, USA) with a mean molecular weight of 30 kDa (DowCellulosics, 2005) were prepared. 6 wt% of polymer blends were mixed in a solution of 2 mM Na-fluorescein (CAS. 518-47-8, Sigma Aldrich, St. Louis, Missouri, USA) and ethanol (CAS. 64-17-5 AnalR NORMAPUR® 96 %, VWR Chemical, Radnor, Pennsylvania, USA), see Figure 20. The EC/HPC polymer ratios studied were 15, 20, 22, 25, 30, 35, 40, 45, 50, 55, 60 and 85 wt% of HPC in the polymer blend.

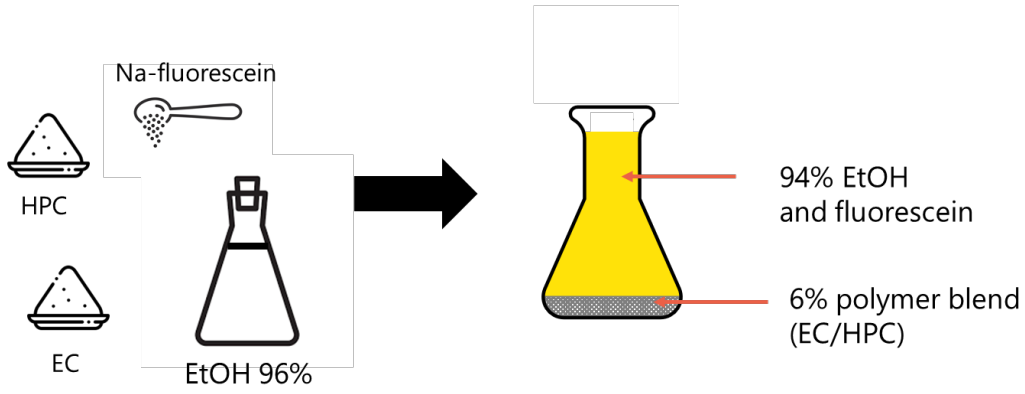

Figure 20 Preparation of EC/HPC solutions in ethanol with fluorescein as flurochrome.

For the viscosity measurements, 16 solutions were prepared with the following compositions: 22, 30, 45, and 60 wt% HPC and 4 ratios of solvent: 94, 90, 85 and 80 wt% of ethanol (96%). The ethanol was added to the polymer blend and the solutions were stirred overnight.

4.2 Spin-coating of EC/HPC films

It is challenging to follow the multilayer formation and the phase separation occurring in a fluidized bed. One technique with which phase separation during solvent evaporation in a thin film is much easier to follow and understand is spin-coating. Therefore, spin-coating was selected to mimic the structure formation occurring in a fluidized bed in this work.

A spin-coater (WS-650MZ-23NPP, Laurell Technologies, North Wales, Pennsylvania, USA) was used to spin-coat the EC/HPC solutions. The volume of the solution was optimized and fixed at 200 µL. The polymer solution was deposed on the surface of a 25x7 mm^2 (thickness 1 mm) glass microscope slide (SuperFrost Ground 90°, Thermo Scientific, Waltham, Massachusetts, USA) for static measurement. For dynamic measurements, the solution was

poured in a 22 mm diameter round glass bottom petri dish (HBST-3522, Willco Wells, Amsterdam, Netherlands).
The spin-coater bowl was equipped with nitrogen flow which ensured a nitrogen environment while coating. The spin speed was varied between 1000 and 10 000 RPM and the spin time between 1 and 45 s. The acceleration ratio, *i.e.* the ratio between the acceleration speed and the spin speed, was fixed at 1:1 (*e.g.* for a spin speed of 3000 RPM, the acceleration was 3000 RPM/s).

4.3 Rheology of EC/HPC mixtures

To determine the zero-shear viscosity of the stock solutions (6 wt% polymer blends in 94 wt% of ethanol) and during evaporation, experiments on different EC/HPC mixtures were conducted on a rotational rheometer (ARES-G2, Texas Instruments, Dallas, Texas, USA). Four ratios of EC:HPC were studied: 78:22; 70:30; 55:45; 40:60 wt% and 4 concentrations of solvent: 94, 90, 85 and 80 wt% of ethanol. A logarithmic flow sweep was performed in triplicate with a bob and cup geometry: 30 mm diameter cup and 27.7 mm diameter bob.

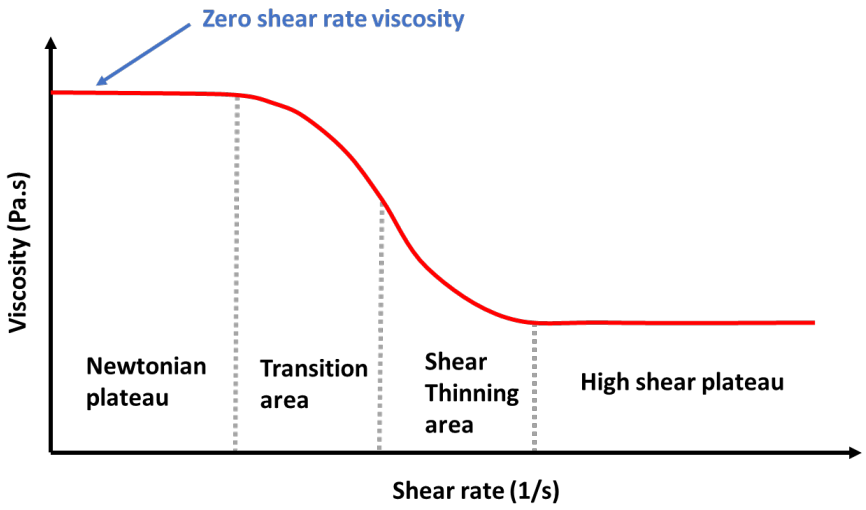

Figure 21 Viscosity profile of a typical shear thinning mixture. Adapted from (Morris et al., 1981).

The system was closed to prevent evaporation. After pouring 25 mL of solution in the cup, the sample was conditioned at 23°C with a soak time of 30s, a pre-shear of 20 s at 0.1 s^{-1} and an equilibration time of 10 s. The logarithmic flow sweep was performed in triplicate with a shear rate from 0.01 to 100 s^{-1} with 10 points/decade. A similar approach was used to determine the viscosity of EC/HPC solutions by Andersson *et al.* (Andersson *et al.*, 2013). The zero-shear viscosity was extrapolated from the rheology data (Barnes, 2000) (see the blue arrow in Figure 21). The specific viscosity at zero shear rate was calculated through the following equation:

$$\eta_{sp,zero\ shear} = \frac{\eta_{zero\ shear}}{\eta_{solvent}} - 1$$

4.4 Profilometry

To determine the thickness of the spin-coated film, a stylus profilometer (Alpha-Step D-100 KLA Tencor, Milpitas, CA, USA) was utilized. Figure 22 shows the principle of stylus profilometers. A contact probe was used to detect the surface. The diamond stylus is physically moving along the surface to measure the surface height. Prior to the measurement, the film surface was scratched with a razor blade. The stylus slides across the film and uses the difference in height from the film surface to the glass surface (inside of a scratch) to determine the film thickness with a precision of about 1 nm. The measurements were performed with stylus speed 0.03 mm/s, stylus force 0.03 N, and using averaging with16 lines per passage.

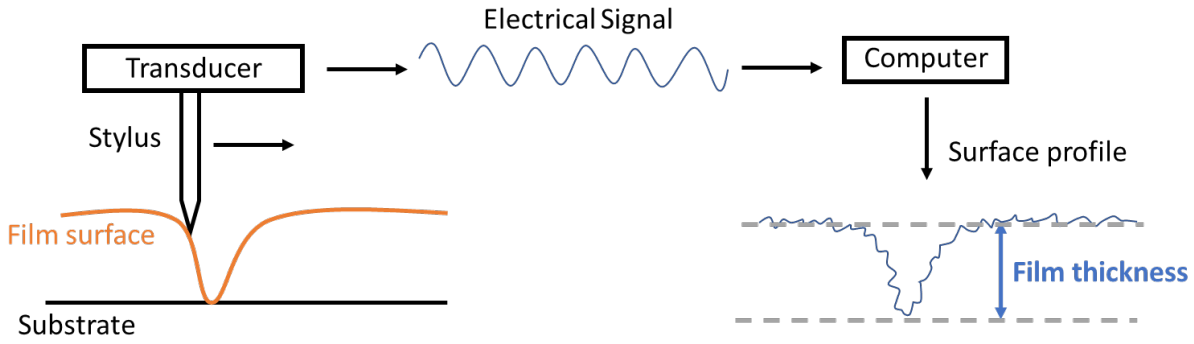

Figure 22 Schematic principle of stylus profilometry. Adapted from (El Khoury, 2017).

4.5 CLSM and analysis of phase separation kinetics

Microscopy is a powerful tool for investigating material structures at different length scales. Confocal Laser Scanning Microscopy (CLSM) offers possibilities to determine material structures at the micrometer scale. CLSM is a fluorescence microscope. The image information is coming from a thin confocal plane in the specimen, which allows for three-dimensional imaging of the structure. For decades it has been an important technique to study soft materials and biological samples (Pawley, 2006). CLSM is a non-invasive technique, it does not need a long and difficult preparation of samples and presents the possibility to study bulk material.

4.5.1 Principle and components

Figure 23 shows a schematic illustration of a CLSM with the principal components. To obtain the image of the specimen one or several laser beams are used to excite fluorochromes in the specimen at specific wavelengths. The laser power transmitted from each laser is controlled by an acousto-optical tunable filter (AOTF). The laser beam goes thought a first pinhole called the illumination aperture and is directed towards the specimen, going through the beam splitter, the scanning mirrors, and the objective. The acousto-optical beam splitter mixes the proportion of light coming from each laser in the array and subsequently transmits it to the specimen. Depending on the scale of observation, the objective features can be changed *i.e.* magnification, numerical aperture and immersion medium. The beam splitter is a filter that differentiates the incoming laser light from the light emitted by the excitation of the specimen. The pinhole removes the out of focus fluorescent light and allows only the light that emanates from the focal plane to go to the detector (Lorén *et al.*, 2007).

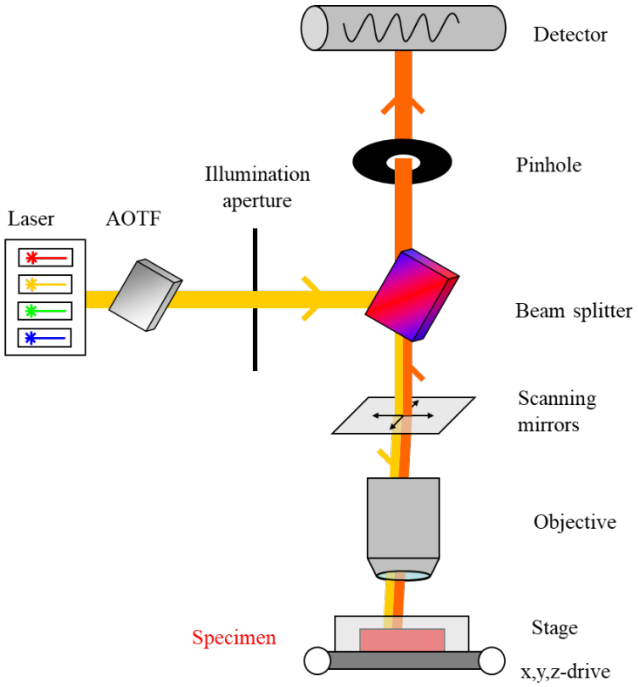

Figure 23 Scheme of a confocal laser scanning microscope.(Lorén et al., 2007).

4.5.2 Fluorescence

Fluorescence is the ability of some atoms and molecules to absorb the light from a specific wavelength and subsequently remit it at longer wavelengths after a short time interval. The CLSM technique is based on using a fluorescent sample. Hence, the sample preparation solely consists of labelling the specimen with fluorochromes (if the sample is not already auto-fluorescent) (Shotton, 1989). Fluorochromes can be dyes added to the solution or fluorescent molecules covalently bonded to the molecule of interest. Different species can be detected separately by using different fluorochromes. Each fluorochrome has a typical emission spectrum and the detector can simultaneously detect different intervals of emission wavelengths for several fluorochromes. If the emission spectra are non-overlapping, it is possible to detect several species at the same time. There are fluorochromes that can bind non-specifically to a whole set of molecules (like protein or fat).

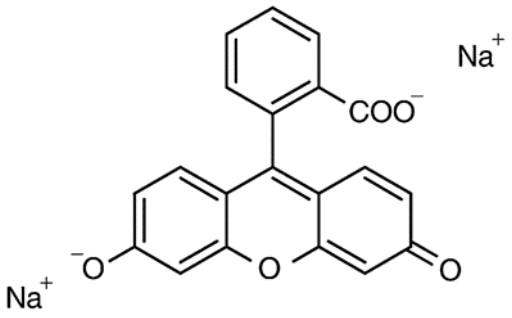

Figure 24 Chemical structure of sodium fluorescein.(Barbero et al., 2009)

For the EC/HPC system, sodium fluorescein (see Figure 24 for the chemical structure) is used to label HPC. In previous studies, sodium fluorescein was mixed in the polymer mixture and

its strong affinity with HPC allowed observation with CLSM (Andersson *et al.*, 2009). However, in most studies in the literature, covalently labelled HPC with fluorescein isothiocyanate (FITC-HPC) is used (Deprez, 2016, Jarke, 2009, McDonough *et al.*, 2015).

4.5.3 Spatial resolution

Controlling and understanding the CLSM objective features allow to obtain a good spatial resolution. It is of fundamental importance to guide the maximum number of photons emitted by the fluorochromes in the specimen safely to the detector. The spatial resolution is governed by the features of the CLSM: the numerical aperture (NA, 0.2 up to 1.45), which determine how much of the re-emitted fluorescent light is collected by the objective; and the working distance of the objective (decreases when NA increases). It is also important to use refractive index matching as much as possible. All these parameters are related to the lateral and axial resolution trough the following equation (Jonkman and Stelzer, 2002).

$$R_{lateral} = \frac{0.4\lambda_{emission}}{NA} \quad , and \quad R_{axial} = \frac{1.4n\lambda_{emission}}{NA^2} \quad with\ NA = n \sin \alpha$$

where $\lambda_{emission}$ is the wavelength of the incoming laser light, NA is the numerical aperture, n is the refractive index of the immersion medium, and α is the maximum half angle of diffracted light that can enter the lens.

Spatial resolution is defined as the minimum spatial separation required between two-point objects to distinguish them as two separate objects. With CLSM, resolution is always a compromise between spatial resolution, temporal resolution, and noise (Sheppard and Shotton, 1997). The signal to noise ratio sets the limits for how small the pinhole can be. In optics, the Airy disk and Airy pattern are descriptions of the best-focused spot of light that a perfect lens with a circular aperture can make, limited by the diffraction of light (Lorén *et al.*, 2007). It has been shown that a good compromise is obtained at a pinhole size equal to the first minimum in the Airy disk. Many commercial instruments set the pinhole size equal the first minimum in the Airy disk by default.

4.5.4 Characterization of phase separation of EC/HPC films with CLSM

The structure of the spin-coated thin film was determined at the micrometer level using CLSM (Leica TCS SP5, Leica, Wetzlar, Germany). A Leica 100x/1.4 PL APO oil objective was used for the characterization and a 488 nm argon laser for imaging. The signal emitted in the interval 500-600 nm was recorded (with a peak expected at 515 nm for maximum fluorescein emission). The theoretical lateral resolution was about 140 nm and the axial resolution was about 530 nm. Zooms between 1x and 12x (FOV 155 and 13 µm respectively) were used, depending on the size of the structure observed. The images were recorded with 1024x1024 pixels with a scanning rate of 400Hz and 6-line averaging for static measurements and no line averaging for kinetics measurements.

4.5.5 Kinetics of phase separation with CLSM

CLSM is a suitable technique for *in situ* observation of structure evolution. For EC/HPC mixtures in ethanol, the solvent evaporation and phase separation take place at room temperature. By scanning the sample at regular time intervals, the dynamics of the phase separation can be determined.

Films were spin-coated in a petri dish with 200µL of polymer mixture for a small amount of time (1 to 10s) so that the film was not totally dried. When starting the spinning time, t = 0s. Directly after the spinning, the petri dish was closed with the lid and placed on the microscope stage. As the temperature is a key parameter influencing both phase separation and evaporation, the temperature was controlled during the whole process temperature: the solutions are in a water bath at 25°C, the temperature bowl was measured for each experiment and was 25±1°C and the stage and objective were heated to 25°C, with an incubation stage and controller system for microscopes (Tokai Hit, Fujinomiya-shi, Japan).

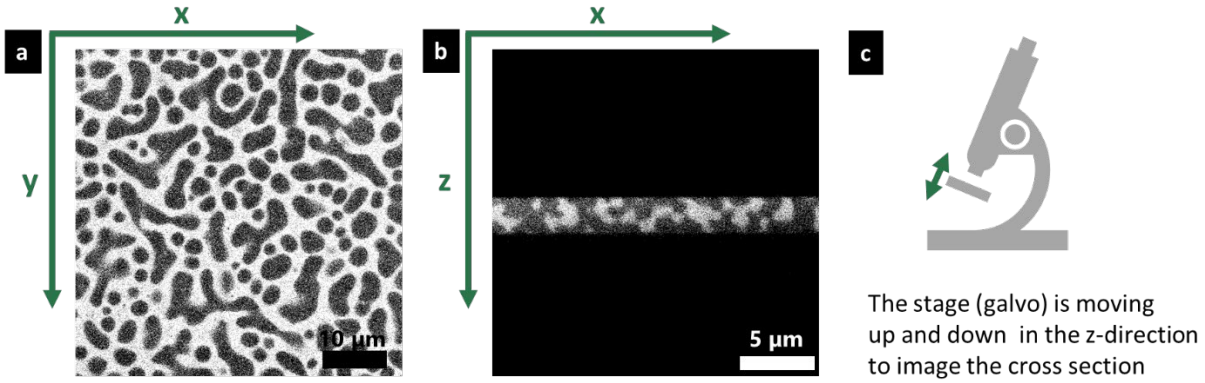

Figure 25 Coordinate system for the kinetic measurements with a) the in-plane xy and b) the cross section xz. c) is a schematic illustration of the galvo stage

In Figure 25, we introduce a coordinate system where the in-plane is denoted as xy-plane and the cross-section plane as the xz-plane. Two types of kinetics measurements were performed.

- XYT measurements with zoom in the range 3x to 8x and a time interval of 2.575 s between each frame.
- XZT measurements with a zoom of 3.44x and a time interval of 2.77 s between each frame. Those measurements were performed with a galvanometric stage that moves rapidly up and down (16 µm/s) and with high precision in the z-direction permitting to image a slice in the xz-plane with high quality.

The association of the two planes offers a good view of the phase separation process and the morphology evolution.

4.6 Image analysis

During SD, a typical periodicity or characteristic length scale of the bicontinuous (interconnected) pattern is unique for each structure and describes the stage of phase separation.

The Cahn-Hilliard model (Cahn, 1965) is the reference model when studying SD and the evolution of the bicontinuous pattern (Playne and Hawick, 2009). Spinodal decomposition can also form discontinuous structures, see Figure 7. When the obtained structure is discontinuous, the term characteristic length scale is still used but it then refers to the diameter of the droplet-like inclusions.

In this work we studied the characteristic length scale L(t) to determine the influence of spin-coating parameters and polymer blend composition on the dried film morphology by three image analysis methods. The time dependent growth was analyzed through the increase of the characteristic length scale. The image analysis was conducted using MATLAB (MathWorks, Natick, MA, USA).

4.6.1 Characteristic length scale determination

4.6.1.1 Fast Fourier Transform

Fourier image analysis is a very pertinent tool for phase separation analysis and has been widely used to extract information from micrographs (Lorén *et al.*, 2002, Wassén *et al.*, 2014, Fujita and Chen, 2018, Zhu *et al.*, 2018).
The steps in the Fourier image analysis are illustrated in Figure 26. First, a background subtraction was performed by smoothing the original image with a 2D Gaussian smoothing kernel with high standard deviation (σ = 100 pixels) and subtracting the smoothed image from the original. Second, the resulting image was smoothed with another Gaussian filter (σ = 2) for noise reduction, see Figure 26a. Third, the Fourier transform of the image was computed. Assuming that the image grayscale intensity in pixel (r_1, r_2) is $f(r_1, r_2)$, the discrete, two-dimensional Fourier transform of an image with NxN pixels (here, $N = 1024$) is computed by,

$$F(k_1, k_2) = \frac{1}{N} \sum_{r_1=0}^{N-1} \sum_{r_2=0}^{N-1} f(r_1, r_2) e^{-\frac{i2\pi}{N}(k_1 r_1 + k_2 r_2)}$$

Fourth, the so-called power spectrum or Fourier space spectrum $P(k_1, k_2)$ was calculated from the Fourier transform by

$$P(k_1, k_2) = |F(k_1, k_2)|^2$$

Figure 26b displays a power spectrum, where each point represents a frequency contained in the real domain image. If the material is statistically isotropic, the power spectrum is radially symmetric, see Figure 26c. The radius k is defined as $k = \sqrt{k_1^2 + k_2^2}$. Hence, fifth, we extracted a radial distribution averaging the power spectrum intensity in a one-pixel width ring for each integer radius value (wavenumber) in the Fourier space. In Figure 26c, a peak that represents the dominant frequency in the Fourier space is visible and corresponds to the characteristic length scale in the original image.

Finally, an estimate of the characteristic length scale L was obtained as

$$L = \frac{FOV}{\mu},$$

with μ being the average of the radial distribution representing the peak in Figure 26c and FOV being the field of view of the micrograph in μm.

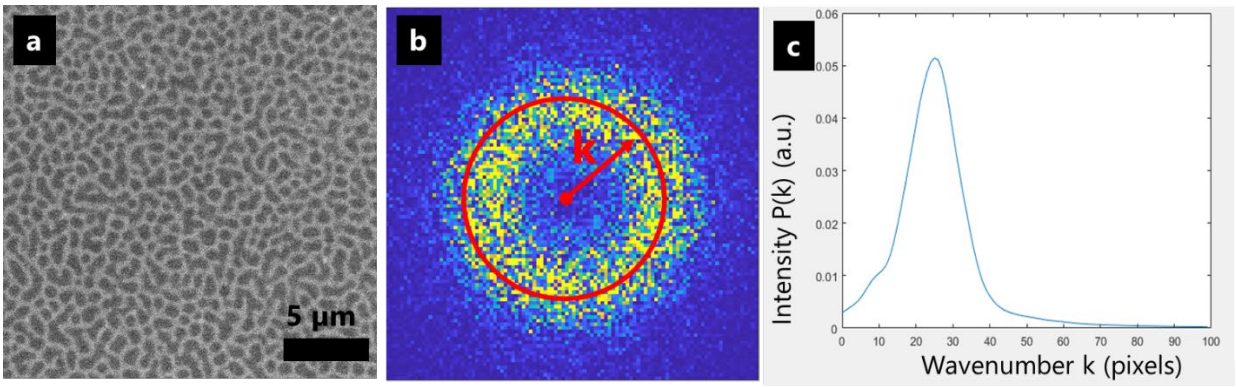

Figure 26 Determination of the characteristic length scale with 2D Fourier Transform. a) CLSM micrograph of HPC 37 wt% spin-coated for 3s at 2000 RPM; b) power spectrum and representation of the radius k c) radial distribution: the wavenumber value at the peak.

4.6.1.2 Domain size for discontinuous structure

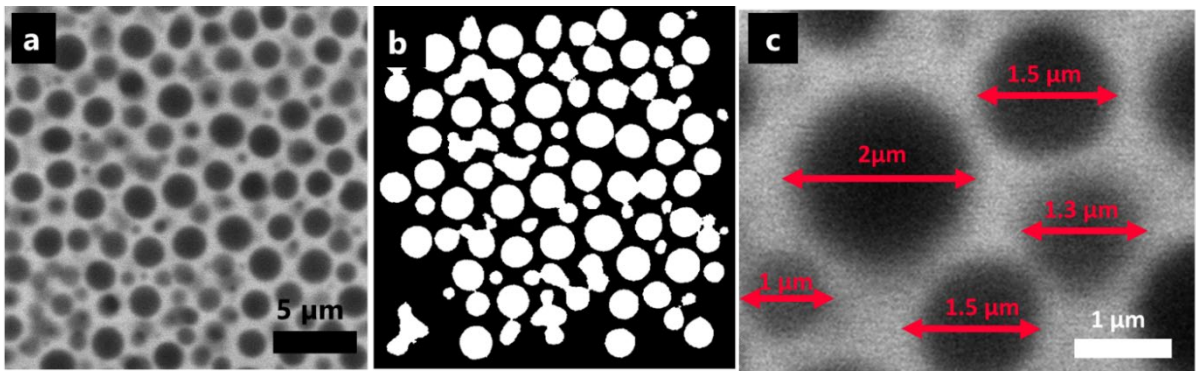

Figure 27 Determination of the characteristic length scale for discontinuous structure. a) HPC:EC 45:55 wt% spin-coated 3s at 2000 RPM with HPC is bright and EC in dark, with b) the corresponding binarized images without the edge elements with EC(white) and HPC(black). c) examples of elements diameter from micrograph (a).

Fourier image analysis is a powerful tool to study bicontinuous structures. However, for discontinuous structures, a complementary image analysis method was developed. We performed image analysis in the following way. First, a noise reduction and a smoothing were performed (as in section 4.6.1.1 Fast Fourier Transform, see Figure 27a). Second, the image was binarized using a threshold value corresponding to the EC:HPC ratio in the polymer blend *i.e.* for a composition EC:HPC 55:45, the 55 % of the pixels with the lowest intensities in the image take the value 1 (white) and the remaining 45 % of the pixels with the highest intensities take the value 0 (black). In addition, the features on the edges of the image are removed, see Figure 27b. Third, the area A of each element (white objects in the figure) was calculated.

Fourth, assuming that each element is a perfect circle the (equivalent) diameter D was determined: $D = 2\sqrt{\frac{A}{\pi}}$

Finally, the mean diameter was calculated in micrometer by averaging the diameter values and multiplying by the pixel size. Figure 27c shows the circular forms of the discontinuous structure and the corresponding calculated diameter. It is important to notice that the obtained sizes depend on the performance of the thresholding.

4.6.2 Power fit and time dependency

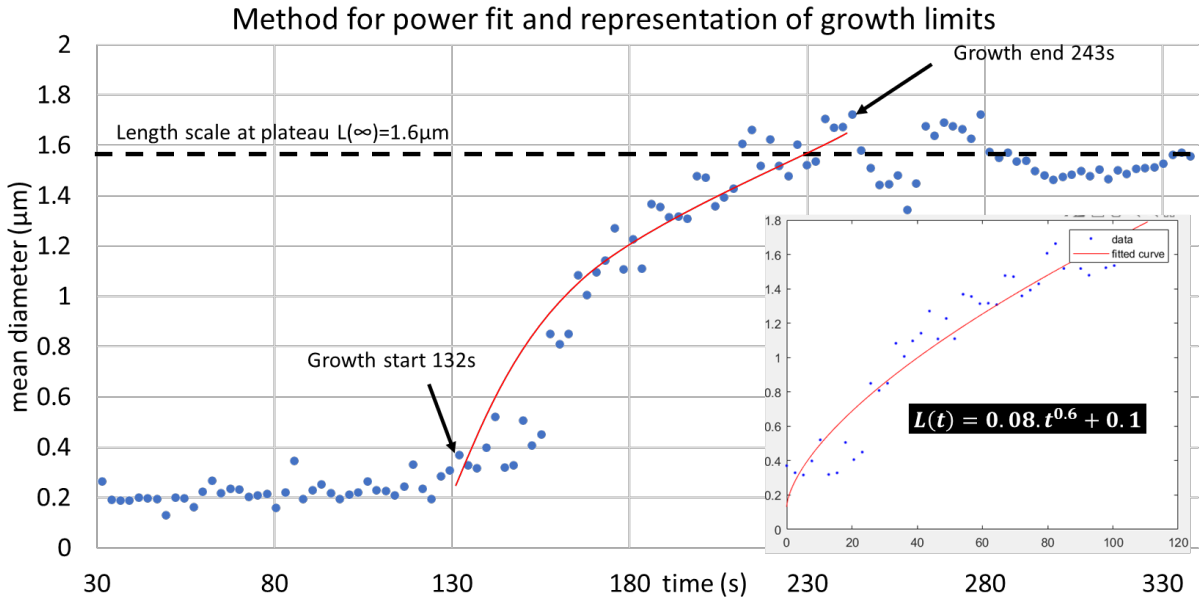

Figure 28 Estimation of the length scale over time for EC:HPC ratio 55:45 wt%, showing the estimated mean diameters (blue), the power law fit (red line). The estimated start and end points of the growth stage is also indicated. In the insert, the part of the data being used for the fit is shown together with the estimated power law relationship.

It was shown that during coarsening the domains grow in a time dependent manner such as the length scale $L(t) = at^n + c$ (see section 3.2.4 Coarsening of phase-separated structures and time dependency). To extract the two parameters a , that we will call the domain growth rate, and n, the time exponent, we performed a fit using least squares to the experimental values of L obtained by image analysis. Figure 28 shows an example of the mean diameter as a function of time for EC:HPC ratio 55:45 wt%. The limits for the fitting (start and end values of t) were determined manually for each series of micrographs by locating the inflection points at the start and end of the increase (see the limits in Figure 28, where the fitting was performed between 132 s and 243 s).

4.6.3 Shrinkage rate

Shrinkage rate was estimated using image analysis on the xzt micrograph-series. Images were taken every 2.77 s. Figure 29 shows the shrinkage of an EC/HPC film over time with EC:HPC 60:40%. By localizing the upper and lower surface of the film (red dashed lines in Figure 29a) it was possible to estimate the thickness. The estimated thickness as a function of time yields

an estimate of the shrinkage rate in µm/min. To compare the different parameters from the experimental design (mainly EC:HPC ratio), we decided to extract 5 values at different points in time for each experiment: at 35 s (t = 0 s indicating the start of the spinning), at the start of phase separation, at the end of the linear regime which corresponds to the time when the structure is kinetically trapped, and at the plateau which corresponds to the end of the shrinkage process. Between the kinetical trap and the end, only shrinkage is taking place.

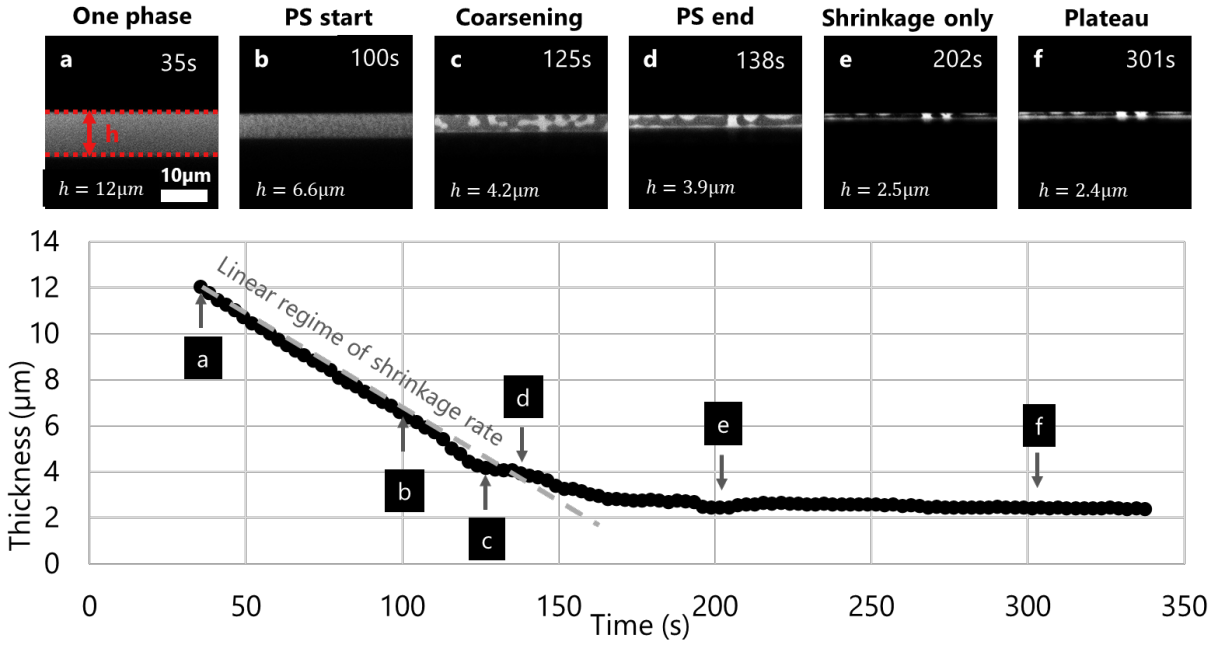

Figure 29 Example of shrinkage rate estimation for EC:HPC 60:40 wt% spin-coated at 2000 RPM for 3s. The points a to f on the curve correspond to the micrographs above taken at key times of the phase separation. The linear regime of shrinkage rate is represented (grey dashed line).

4.6.4 Curvature evolution and curvature map

To fully understand the phase separation, we wanted to determine which coarsening mechanisms are prominent for given conditions (see section 3.2.4 Coarsening of phase-separated structures and time dependency). During hydrodynamic growth, the domains are coarsened, and the shapes evolve from high curvature (small radius of curvature) to low curvature (large radius of curvature). Being an important indicator of the phase separation mechanisms, changes of curvature at the EC/HPC interface during the coarsening are therefore evaluated.

To obtain the curvature, a formula developed by Coeurjolly and Svensson called osculating radius formula (Coeurjolly and Svensson, 2003) was used. Figure 30 shows the principle of osculating radius: the curvature in v_o is given by the inverse of the radius of the circumscribing circle of the triangle (v_0, v_1, v_2) (see Figure 30).

$$R_c = \frac{abc}{4A}$$

With A being the area of the triangle (v_0, v_1, v_2)

$$A = \frac{\sqrt{(b+c)^2 - a^2}.\sqrt{a^2 - (b-c)^2}}{4}$$

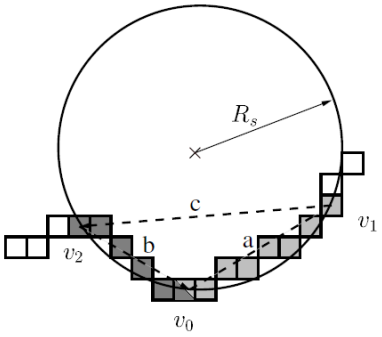

Figure 30 Illustration of the osculating radius formula to approach the curvature estimation (Coeurjolly and Svensson, 2003).

Figure 31a is a randomly generated Bezier curve. By using the osculating formula, we could estimate the local curvature on each point of a curve. In Figure 31b, the Bezier curve in the xy-plane and the local curvature on each point is plotted on the Z axis. It can be seen that for large radii of curvature (straight curve), the curvature is low and for small radii of curvature, the curvature is high.

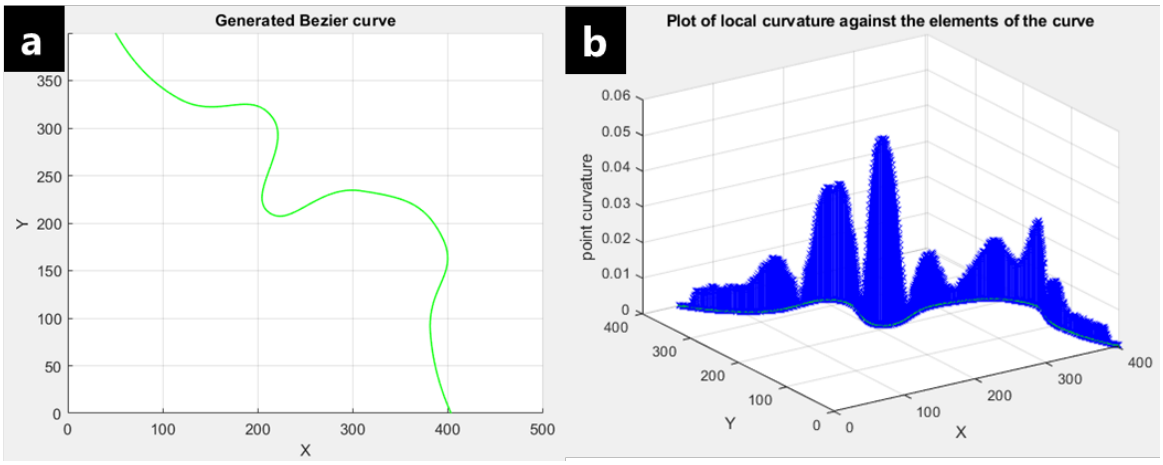

Figure 31 Example of the calculation of the local curvature at each point of a (a) Bezier curve, with (b) the corresponding local curvature values for each point along the curve in (a).

Figure 32 is an example of the determination of the curvature at the EC/HPC interface. We performed image analysis in the following fashion. First, a background subtraction was performed by smoothing the original image with a 2D Gaussian smoothing kernel with high standard deviation (σ = 100) and subtracting the smoothed image from the original. Second, the resulting image was smoothed with another Gaussian filter (σ = 10) for noise reduction, see Figure 32a (in dark the EC and in bright the HPC). Third, the image was binarized with a threshold value equal to the EC:HPC ratio, see Figure 32b (in white the EC phase and in black the HPC phase). Fourth, we identified and extracted the interfaces as independent curves, then for each point of the curve the curvature was calculated. Figure 32c shows the interfaces, and the color scale corresponds to the curvature value. Figure 32d shows the distribution of the

curvature over the micrograph for all the EC/HPC interfaces. Finally, the mean curvature was calculated, and it was plotted *versus* time to follow the curvature evolution.

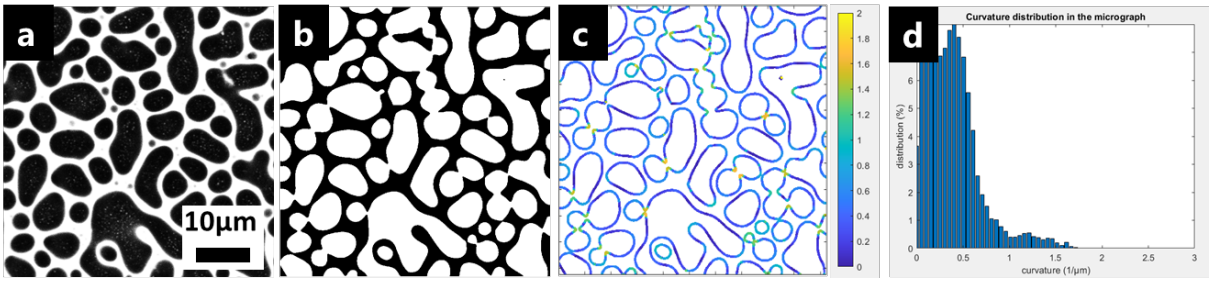

Figure 32 Example of local curvature determination for a micrograph. (a) HPC 37wt% at 495s ; white is HPC and black EC (b) binarization: white is EC and black HPC (c) Identification of the interface and calculation of the local curvatures for each point at the interface (d) corresponding distribution of the local curvature in the micrograph.

5 Results and Discussion

The focus of this work is to investigate the structure evolution and to determine the influence of EC:HPC ratio and process parameters on the formed structure. Here we introduce our model for mimicking of the industrial pellet production process using spin-coating. By observing the structure evolution and the final structure, different structure categories are discriminated. An overview of the influence of the EC:HPC ratio on the structure evolution and possible explanations of the different coarsening mechanisms and phenomena involved in the structure formation is given. Finally, we show preliminary results obtained during the mimicking of a multi-layered film.

5.1 A model system for the industrial process of spray-coating

5.1.1 Film formation and film thickness

Observing the phase separation *in situ* during fluidized bed spraying raises big challenges. Information can be obtained by analyzing the final dried microstructure of standing films or of pellet coating (Fager *et al.*, 2020a, Fager *et al.*, 2020b). However, in this work, we would like to monitor the effect of composition and process on the structure evolution and the final structure. Therefore, the strategy is to understand the kinetics of structure formation and the microstructure origin by creating a model to mimic the industrial process of fluidized bed spraying.

The main elements to reproduce and control are the production of a thin film and the homogeneous evaporation of ethanol over the film surface. In the fluidized bed, the polymer solution is coated around a pellet. Figure 33 shows an illustration of the industrial pellet structure. The core is coated with a drug layer that will be delivered in the body and this layer is coated with a phase-separated EC/HPC film. Previous results have shown that the polymer film contained a layered structure as represented in Figure 33 (Fager *et al.*, 2021). Our hypothesis is that each passage in the spraying zone corresponds to a layer and that one layer is about 1.5µm thick.

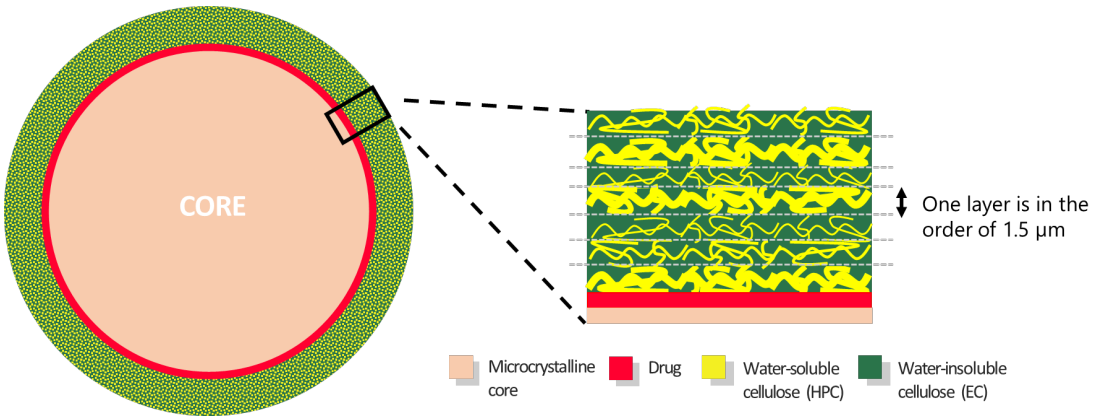

Figure 33 Illustration of the multi-layered phase-separated coating around a pharmaceutical pellet obtained via the industrial process.

The spin-coating technique is a widely used technique for making uniform polymer films, showing high reproducibility in film structure, and was chosen to make EC/HPC films in this work. To measure the film thickness and to check that the produced films are homogenous in thickness we used profilometry. Having chosen the spin-coating technique to mimic the industrial spraying process, our aim was to determine the effect of the spin-coating parameters on the phase-separated structure. After some testing, the spin time and the acceleration ratio were fixed to 45 s and 1:1, respectively. The effect of spin speed on the final film structure and thickness was investigated.

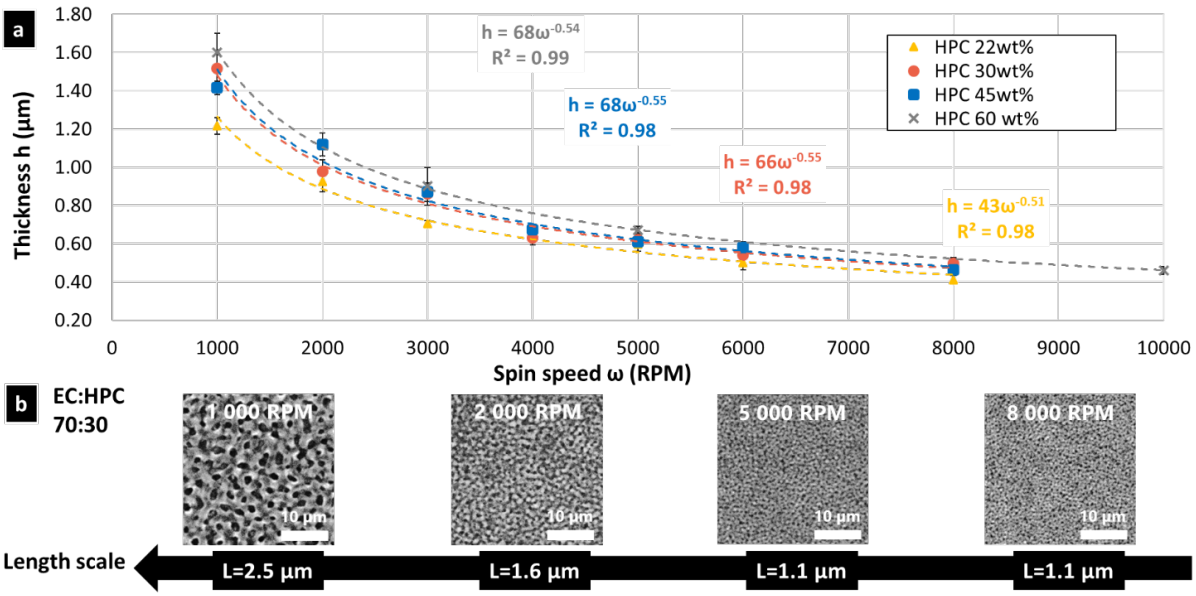

Figure 34 Influence of the spin coating parameters. a) Thickness determined by profilometry versus the spin speed (m +- sd). b) Micrographs of 30wt% HPC films spin coated at 4 different spin speed: 1000, 2000, 5000 and 8000 RPM, the corresponding length scale obtained by FFT is displayed.

Figure 34 shows the effect of different spin speeds on the film thickness for different compositions and the corresponding microstructure. Figure 34b shows CLSM micrographs of spin-coated films at different spin speeds: 1000, 2000, 5000 and 8000 RPM at magnification 500x (FOV 31 µm) for 30 wt% HPC and 70 wt% EC. The bright phase corresponds to the HPC phase and the dark phase to the EC phase. The micrographs of Figure 34b were taken in the center of the microscope slide, corresponding to the center of rotation during the spinning. The characteristic length scale L, shown under the CLSM micrographs, is obtained with Fourier image analysis. It is decreasing with increasing spin speed for the composition HPC 30 wt%: $L_{1000\,RPM} = 2.5$ µm and $L_{8000} = 1.1$ µm. This suggests that the phase separation (SD followed by coarsening) is stopped in an earlier stage of coarsening at higher spin speed. One possible explanation is that at higher spin speed the evaporation is faster. This explanation is supported by Birnie *et al.* (Birnie and Manley, 1997) who determined the ethanol evaporation rate for a spin speed in the range 500-3000 RPM. They found that the ethanol evaporation rate varies with the square root of the spin speed.

In Figure 34a, spin curves were plotted for the compositions 22, 30, 45 and 60 wt% HPC in the polymer blend, *i.e.* the average thickness of the films h is plotted against the spin speed ω. The spin curves were fitted with a power law and the values of the exponent n were determined.

Our purpose was to determine if there was some correlation between thickness and spin speed. In addition, to mimic the industrial film the thickness had to be in the order of a micrometer. Figure 34a shows that the phase-separated polymer film is thinner when the spin speed is higher, *e.g.* $h_{HPC30}(1000\ rpm) =$ 1.5 µm and $h_{HPC30}(8000\ rpm) =$ 0.5 µm. This can be explained by the fact that the increase of centrifugal forces leads to more material being spread out in all directions and hence to a thinner film. There is also a small tendency that the films become thicker when increasing the HPC ratio. A possible explanation could be that the viscosity increases with increasing HPC ratio resulting in thicker films.

Meyerhofer developed a mathematical model for spin-coated films that relates the film thickness to spin speed, initial viscosity and evaporation rate (Meyerhofer, 1978). In particular, it was shown that the thickness h decreases with increasing spin speed ω according to the relation $h \propto k*\omega^{-0.5}$, with a constant k that depends on the viscosity, density and concentration of the solution. The derivation of the model is built upon a two-step thinning during spin-coating. Meyerhofer proposed that during the first step, the thinning is dominated by the fluid being spun off (outflow) and that during the second step, the thinning is dominated by the evaporation. At the transition point, the outflow and evaporation contributions are equal, and the thickness can be estimated analytically. This two-step thinning during spin-coating has previously been used to explain the structure of phase-separated polymer system (Toolan *et al.*, 2013, Ebbens *et al.*, 2011, Heriot and Jones, 2005, Mokarian-Tabari *et al.*, 2010b). In addition, the Meyerhofer model also assumes that the evaporation rate is uniform, the thickness is constant all over the film, and that changes of concentration in the z direction (through the film) can be neglected.

In this work, the obtained power law exponents were -0.54, -0.55, -0.55, and -0.51 for 22, 30, 45, and 60 wt% HPC, respectively. The fits in Figure 34a show that the assumptions made by Meyerhofer leading to the relation $h \propto k\omega^{-0.5}$ are consistent with the experimental data obtained on the spin-coated EC/HPC mixtures. For example, it was observed that the thickness is constant in most parts of the film and that the structure is homogenous in the z direction. The Meyerhofer model provides an understanding of the thickness variations when changing spin-coating process parameters and that it is likely that a two-step thinning mechanism, hydrodynamic thinning followed by evaporation thinning, is active during the spin-coating of the EC/HPC films.

5.1.2 Evaporation process

Another crucial aspect of the EC/HPC phase separation is the evaporation process. When the evaporation starts the system phase separates while moving in the phase diagram. And at some point, during the evaporation, the structure is kinetically trapped before reaching the equilibrium. It is essential to determine the rate of the evaporation and find at which point of the evaporation the structure is trapped. Phase separation during solvent evaporation has been studied previously (De Gennes, 2001, Bassou and Rharbi, 2009, Schaefer *et al.*, 2015, Cummings *et al.*, 2018).

In our experimental set up, the evaporation process was slowed down using a closed petri-dish to facilitate fast-microscopic imaging.

Figure 35 shows the result of gravimetric experiments to determine the ethanol evaporation. A drop of 200 µL was deposed in a petri dish and spin-coated for 3s at 2000 RPM to form a film. The weight of the petri dish was set to zero at time zero and the solution's weight was followed over time. In Figure 35 we compare the weight loss after spinning in two cases: in an opened petri dish and in a petri dish closed with a lid. Our aim was to estimate the evaporation rate after spinning in open air at ambient temperature and estimate the decrease of evaporation rate when closing the petri dish.

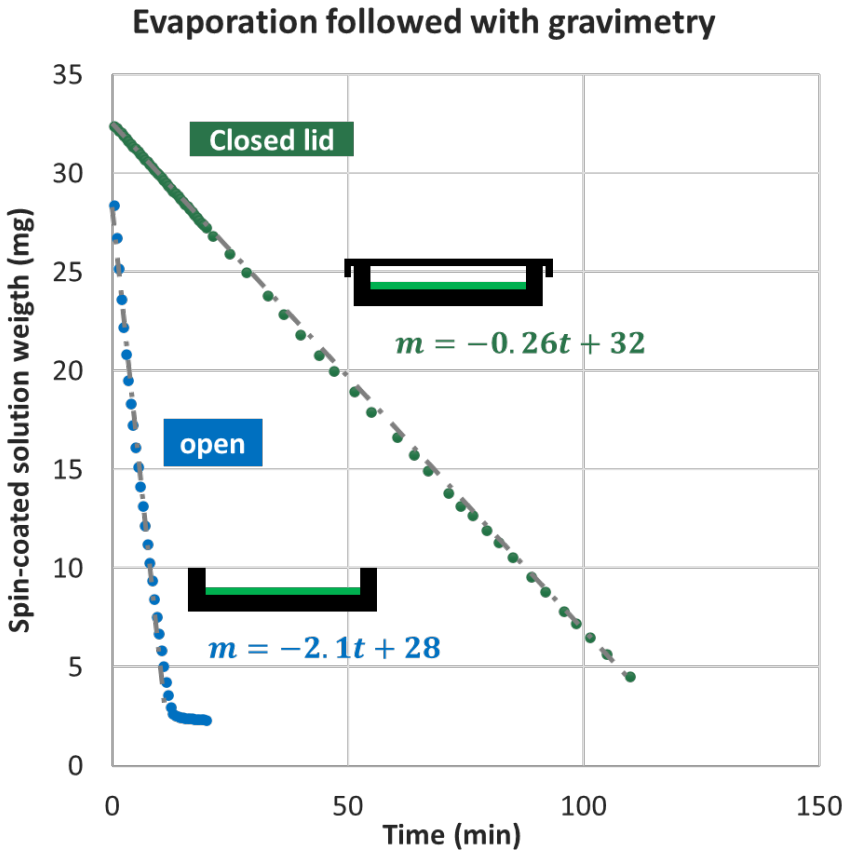

Figure 35 Estimation of the evaporation rate by gravimetry. Comparison between an open (blue dots) and a closed (green dots) petri dish.

Figure 35 shows that the weight loss is linear which is in accordance with results found in the literature (Innocenzi *et al.*, 2008, Mokarian-Tabari *et al.*, 2010a). For the open petri dish, the weight reaches a plateau, corresponding to the remaining solid fraction. From the linear regression slopes of -0.26 and -2.1 min/mg were obtained for the closed and opened petri dish, respectively. The ratio $\frac{evaporation\ rate_{opened}}{evaporation\ rate_{closed}} = 8$ shows that the evaporation is slowed down approximately 8 times by closing the lid at room temperature (25°C), which can be used to delay the onset of phase separation.

5.1.3 Experimental set up

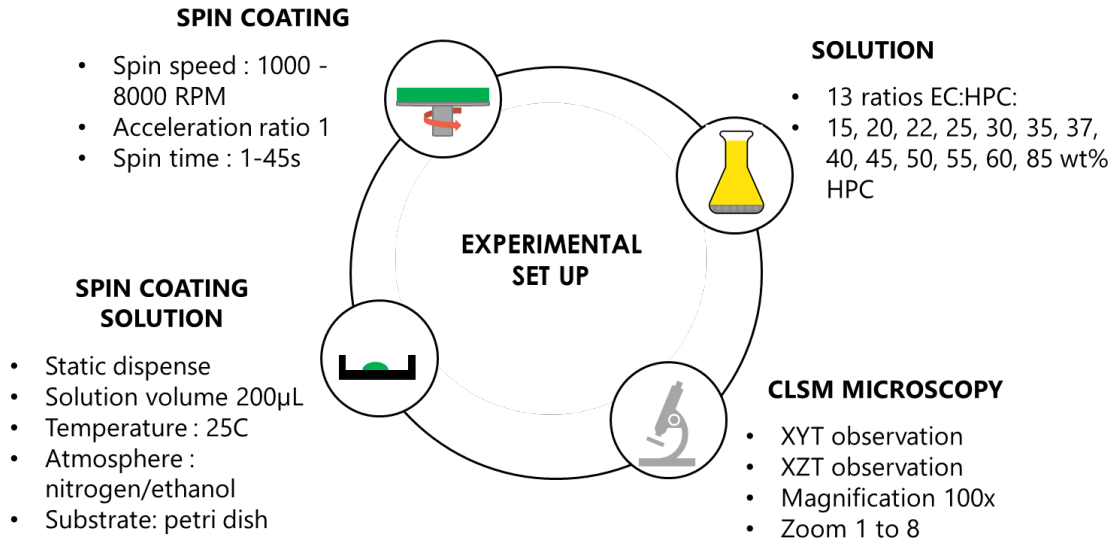

Figure 36 Schematic illustration of the experimental set up, showing the varied and fixed parameters.

To investigate the structure evolution and the final structure in thin films, an experimental set up was developed. The experimental design involved testing the influence of spin speed, volume of substrate, spin speed and spin time, on the film formation. Also, it is widely known that the atmosphere, *i.e.* temperature and humidity, has a strong influence on spin-coating results (Mokarian-Tabari *et al.*, 2010b, Dandapat *et al.*, 2005) and particularly on the structure development. For example high temperature can provoke Marangoni effect (Yiantsios *et al.*, 2015, Fowler *et al.*, 2016) and high humidity can alter the structure formation (Birnie, 2011). Figure 36 summarizes the experimental design of this work. The influence of spin speed and spin time on the final structure were investigated. To evaluate the kinetics of phase separation, spin speed and spin time were fixed at 2000 RPM and 3s and the EC:HPC ratio was the main parameter investigated. For CLSM analysis two modes of observation (xy and xz) were chosen to characterize the film's 3D structure. In all cases, the experiments were carried out in humidity free atmosphere (nitrogen purge) and at 25 °C.

5.2 Coarsening of bicontinuous structures

The combination of spin-coating in a closed petri dish and confocal microscopy allowed to produce a uniform wet film and to follow the phase separation during evaporation. Figure 37 is showing the structure evolution of a thin film of EC/HPC with 37 wt% HPC during phase separation. Figure 37a is showing four micrographs corresponding to the structure evolution of a bicontinuous pattern typical of spinodal decomposition. Figure 37b is showing the corresponding curvature at the interface between EC and HPC. Figure 37c is the corresponding curvature distribution. Figure 37d is displaying four micrographs in the xz-plane showing the structure evolution and the estimation of the thickness (denoted h). Note that the upper surface is the glass surface, and the lower surface is the air surface.

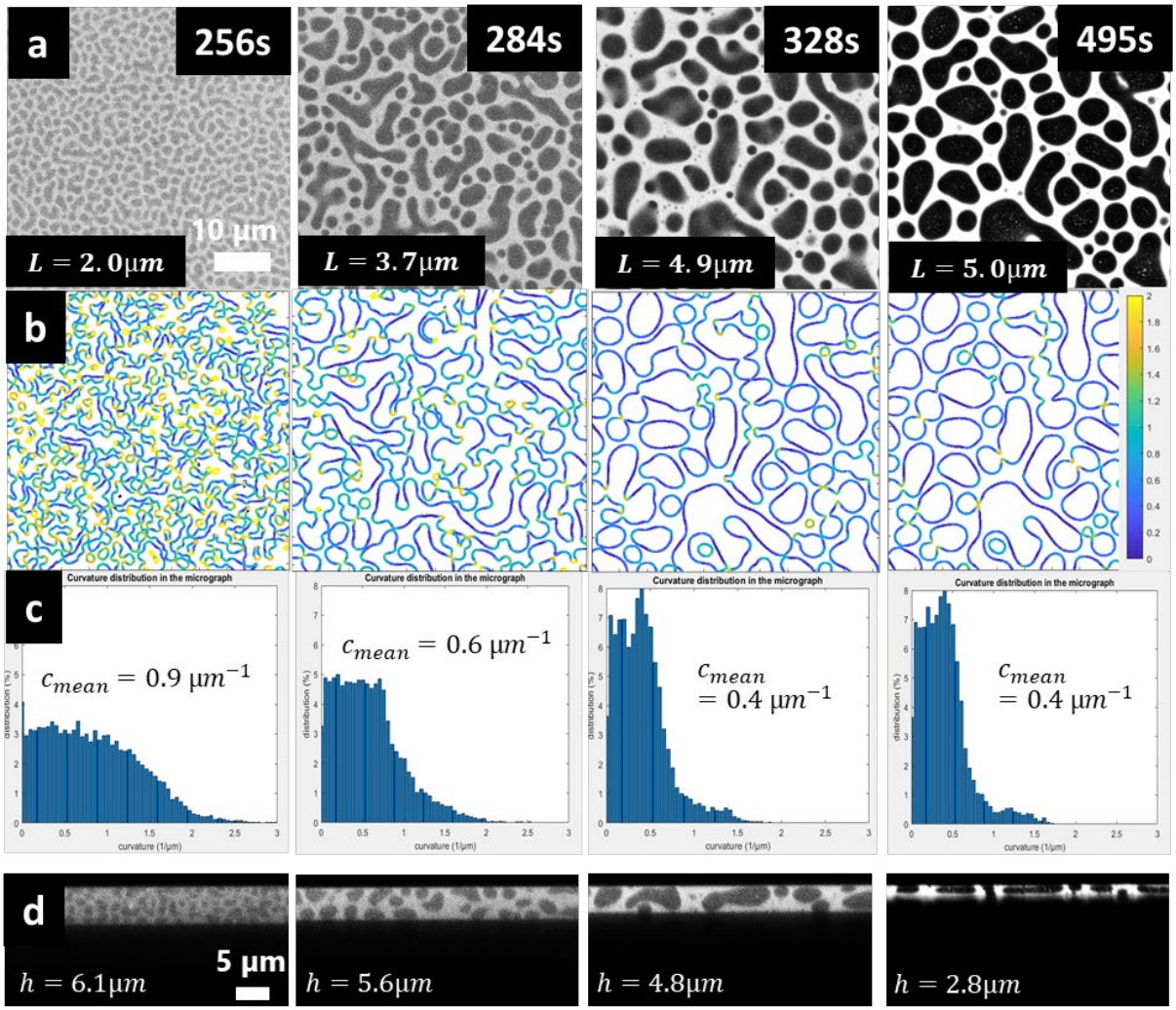

Figure 37 Structure evolution during phase separation of EC/HPC thin films that leads to a bicontinuous structure. a) xyt observation using CLSM with the length scale calculated with FFT b) interface identification and curvature calculation, with the corresponding color scale to the right c) curvature distribution d) xzt observation using CLSM with the thickness calculated with image analysis. The upper surface is the glass surface, and the lower surface is the air surface.

The length scale shown in Figure 37a is increasing over time. The first micrograph corresponds to an intermediate stage of the spinodal composition. The second micrograph at 284s corresponds to the coarsening phase, the length scale has increased from 2.0µm to 3.7 µm. At plateau (495s), the structure is trapped and almost all the ethanol has evaporated, the characteristic length scale has grown about 2.5 times the initial length scale. It can be observed that at 328s (3rd image from the left), the length scale L is nearly equal to the thickness h. We believe that after this point the coarsening is mainly taking place in 2D, not in 3D anymore, and that the wetting of surfaces will have an impact. After trapping of the coarsening, the structure can still shrink in the z direction. The preferential wetting is shown in Figure 37d in the fourth micrograph. According to the findings of Tanaka (Tanaka, 2001), the preferential wetting is taking place, it indicates that one of the phases has more wettability with the substrate surface. Our hypothesis is that HPC has preferential wetting to the glass-surface compared to EC explaining that HPC is present at both air and glass surfaces. The changes of curvature during phase separation in Figure 37b and Figure 37c show that the structure is shifting from high

curvature to low curvature over time *e.g.* the mean curvature at early stage is changing from $c_{mean}(t = 256s) = 0.9\ \mu m^{-1}$ to $c_{mean}(t = 495s) = 0.4\ \mu m^{-1}$ at plateau. When the curvature changes in this manner it implies that the coarsening is interfacial tension driven and that the main mechanism of coarsening is hydrodynamic growth (see also section 3.2.4 Coarsening of phase-separated structures and time dependency). Zoumpouli *et al.* simulated the phase separation during solvent evaporation and investigated particularly the role of hydrodynamics (Zoumpouli and Yiantsios, 2016). They found that the hydrodynamic coarsening is taking place preferably in a symmetric system *i.e.* having close to equivalent volume fractions of the two phases.

Figure 38 is a series of micrograph showing a typical hydrodynamic growth mechanism. The first micrograph at 264s shows EC domains with arms attached to a central body. On the armed structure the interfacial curvature is high, which corresponds to high Laplace pressure. The red arrows in the CLSM micrograph at 269 s represent the Laplace pressure gradients from the arms to the center causing a Poiseuille flow. EC material is flowing from the arms to the center as we can observe in the series of micrograph from 264s to 315s. At the end of the coarsening, the interface curvature has become reduced. The same coarsening behavior is seen for several domains in the structures of Figure 37b. The same behavior has been found in other systems, Bouttes *et al.* observed hydrodynamic coarsening for silica melt and noticed the same changes of curvature over time caused by the flow of the regions with high curvature towards the regions with low curvature (Bouttes *et al.*, 2015).

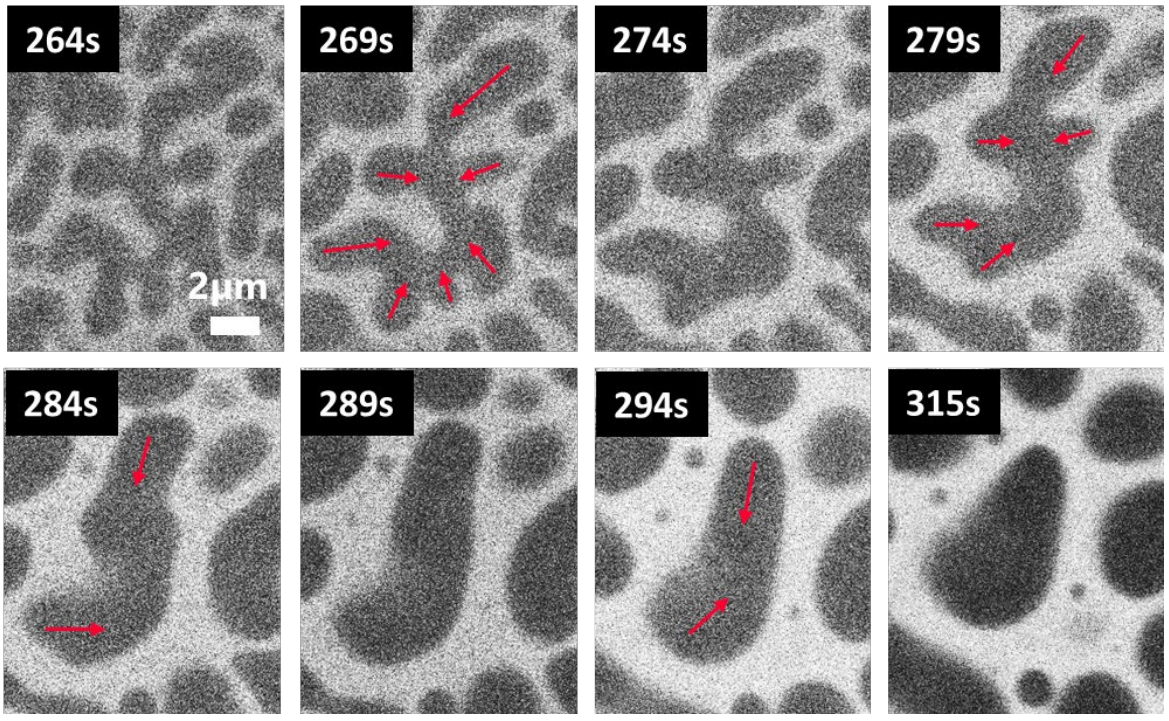

Figure 38. Typical hydrodynamic growth during coarsening of HPC 37wt% spin-coated at 2000 RPM during 3s (HPC is bright, EC is dark). The Laplace pressure gradients that cause the Poiseuille flow and the hydrodynamic growth are indicated (red arrows).

5.3 Coarsening of discontinuous structures

The second type of structures that are observed during phase separation in EC/HPC films are discontinuous structures. Inclusions of either HPC or EC domains appear and grow in a matrix of the other polymer.

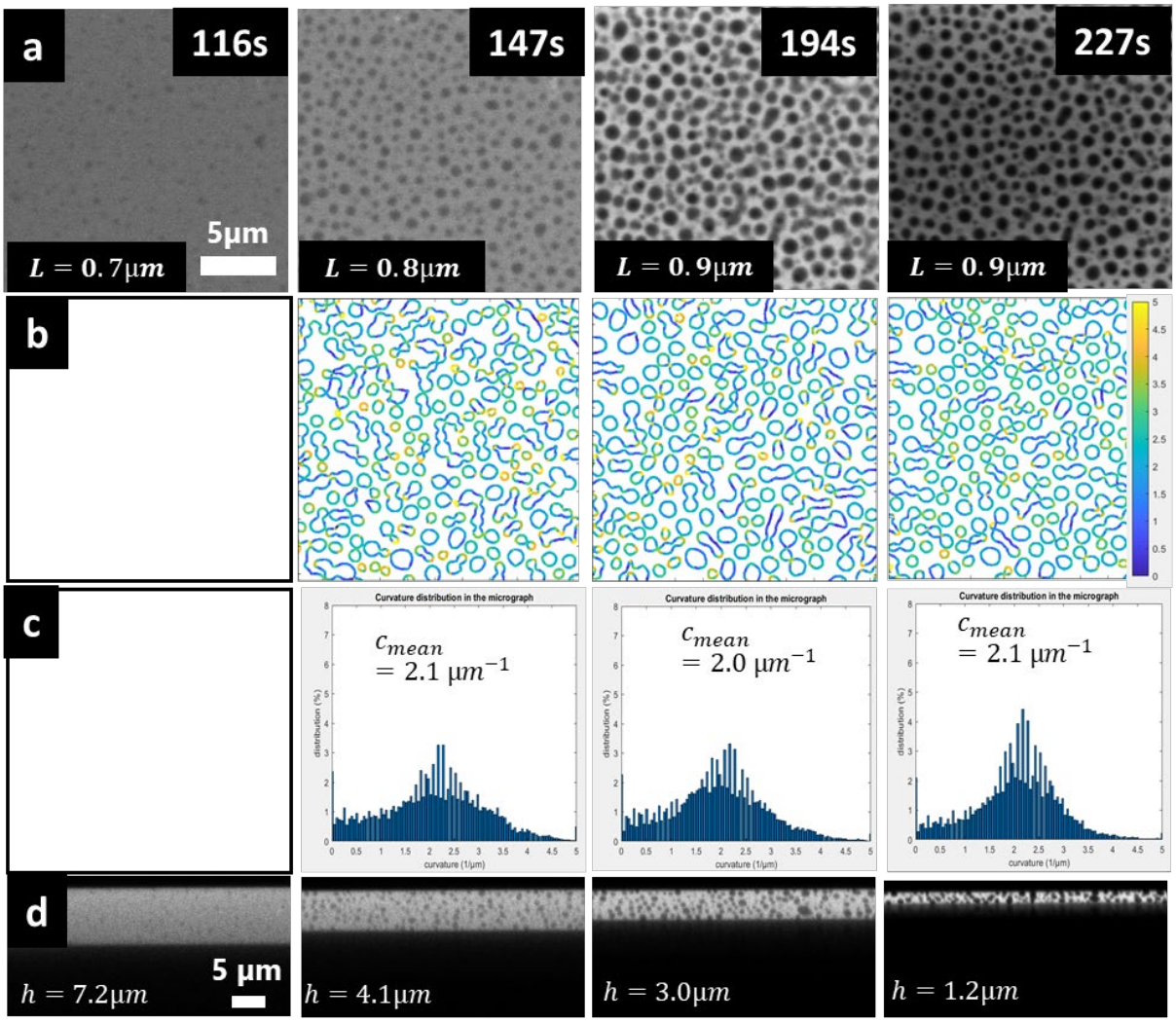

Figure 39 Structure evolution during phase separation of EC/HPC film showing a typical discontinuous structure formation for EC:HPC 40:60 wt%. a) xyt observation with the length scale calculated from the inclusion diameter. The time from the start of the experiment is displayed in the top right of each CLSM micrograph. b) interface identification and curvature calculation, with the corresponding color scale to the right c) curvature distribution d) xzt observation with the thickness calculated using image analysis. The upper surface is the glass surface, and the lower surface is the air surface.

Figure 39 is showing the structure evolution of a thin film with 60 wt% HPC during phase separation. Figure 39a is displaying four CLSM micrographs corresponding to the structure evolution of a typical discontinuous pattern with EC inclusions in a continuous HPC phase. Figure 39b is showing the corresponding curvature at the inclusion interfaces. Figure 39c is displaying the corresponding curvature distribution. Finally, Figure 39d is showing four CLSM micrographs in the xz-plane, which display the structure evolution and the estimated film thickness. The upper surface is the glass surface, and the lower surface is the air surface. It can be observed in Figure 39a that the discontinuous structure is growing over time. In the early

stage of phase separation ($t = 147s$), EC inclusions start to appear, and while keeping their circular shape they grow over time, *e.g.* the mean diameter is $D = 0.7$ µm at early stage compared to 0.9 µm at plateau. To determine the length scale L, we used image analysis to estimate the diameter. Because the structure is keeping its circular shape the curvature is not evolving so much, as Figure 39b and Figure 39c are displaying, even if the size of the inclusions are increasing slightly.
Figure 39d is showing the film evolution on the xz-plane. It confirms that the structure is discontinuous also in the depth direction, and that the EC inclusions are spherically shaped. It can be noticed that the diameter of the inclusions is generally smaller than the film thickness during the whole experiment. At $h = 3.0$ µm and $t = 194s$ the structure is kinetically trapped and does not grow further. However, shrinkage can be observed between the micrograph in Figure 39d from $h = 3.0$ µm to $h = 1.2$ µm showing that the structure growth is trapped before the evaporation is complete. We believe that at this point the viscosity of the mixture is so high that the mobility of the phases is halted, and only evaporation and shrinkage is observed.

In Figure 40, three CLSM micrographs were selected to show an example of coalescence that takes place during coarsening. In the first micrograph, at $t = 281s$, two EC inclusions start to move towards each other to finally merge at $t = 302s$. This type of coarsening mechanism is typically observed in discontinuous structures and is diffusion driven. The initial and final state is a circular shaped structure.

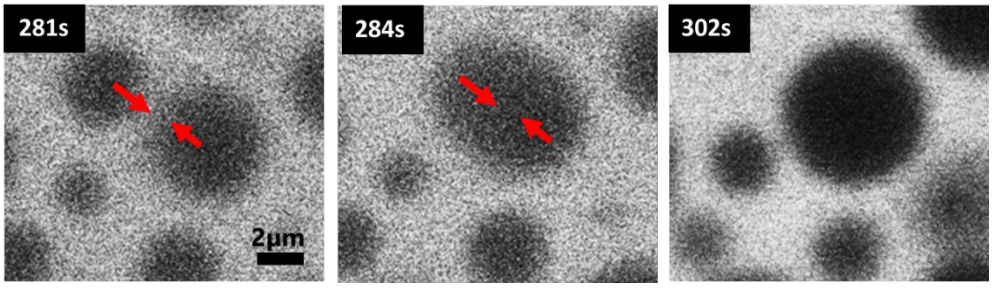

Figure 40 Typical coalescence observed during phase separation of EC:HPC 45:55 wt% (HPC is bright, EC is dark).

5.4 The time-dependent structure evolution

5.4.1 In plane structure evolution

In this section, we give an overview of the structure evolution of phase-separated structures taking place in spin-coated EC/HPC thin films. The main parameter that was varied is the EC:HPC ratio, and 13 different ratios from 15 to 85wt% HPC were investigated. Figure 41 shows CLSM micrographs of film structure evolution for the 13 ratios at different key times of the phase separation.
The first row corresponds to a stage before the phase separation has started, EC and HPC are in one phase, the micrographs are grey and homogeneous. The second row corresponds to the phase separation start, and some vague structures can be observed. This includes for instance, white inclusion of HPC in EC matrix for the ratios 15 to 22 wt% HPC, black EC inclusions in HPC matrix for the ratios 45 to 85wt% HPC, and interconnected structures for the ratios 25 to

40 wt% HPC. The third row corresponds to the growth start, where the power fit starting limit is taken. The fourth row shows the structure during coarsening. The fifth row corresponds to the power fit end where the growth ends. After this point the structure is kinetically trapped and does not grow anymore. Finally, the sixth row corresponds to the length scale at plateau, when the evaporation process is complete, and only solid polymers remain.

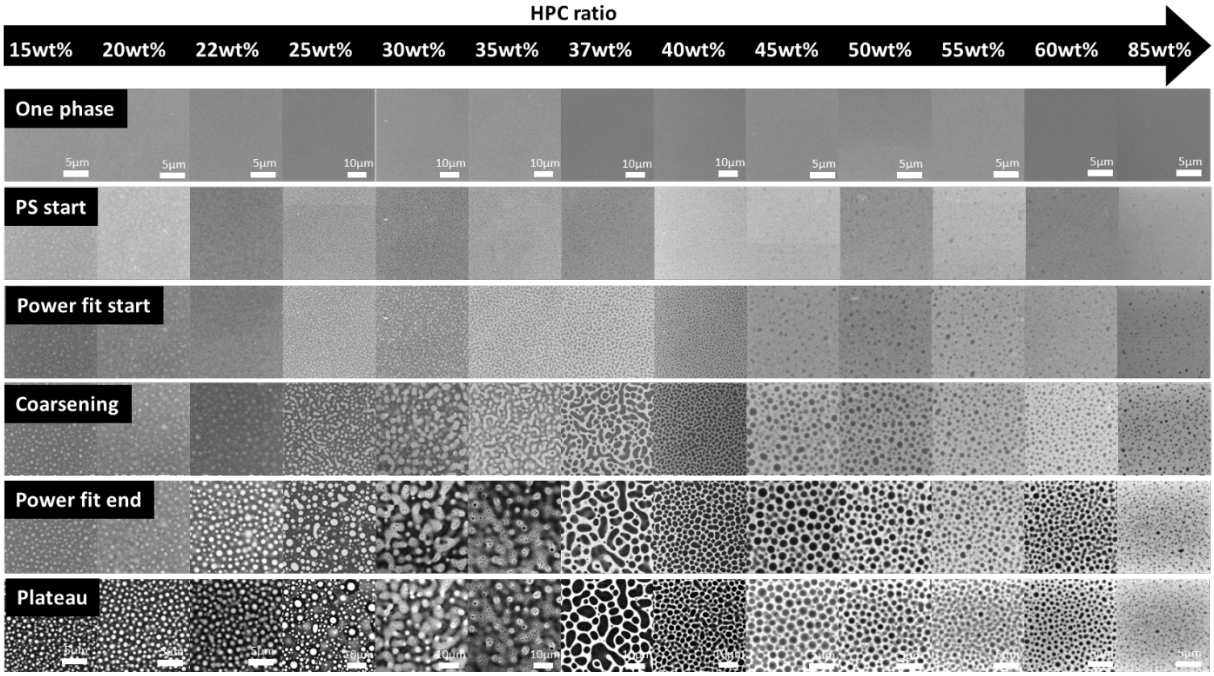

Figure 41 Overview of structure evolution of EC/HPC films at 13 EC:HPC ratio. The x axis is the HPC ratio, and the y-axis corresponds to different key times of phase separation: one phase, the phase separation (PS) starts, the start of structure growth, coarsening during growth, the end of structure growth and finally at plateau, when the structure is trapped.

It can be noticed that from the third row to the fifth the structure evolution is noticeably different depending on the ratio EC:HPC. We identified three cases: i) where, bright HPC droplet like inclusions in a dark EC matrix are forming a discontinuous structure. We observe this for the ratios 15 to 22 wt% of HPC; ii) where a bicontinuous structure is formed, the volume fractions of EC and HPC are almost equal, and the domains are interconnected. This case is observed for the ratio 25 to 40 wt% of HPC iii) where dark EC droplet like inclusions in a bright HPC matrix are forming a discontinuous structure, which is observed for the ratios 45 to 85 wt% of HPC. The ratio of 25 wt% HPC seems to be at the limit between a discontinuous and a bicontinuous case.

Figure 42 shows an illustration of the different cases observed in the micrographs in Figure 41. To the left of Figure 42, a schematic phase diagram is shown. To the right of Figure 42, illustrations of the corresponding structure is displayed. Depending on the path that the mixture will follow from the 1-phase to the 2-phase region, the mechanism of phase separation is different and various morphologies are obtained.
Figure 42 shows a hypothesis on the mechanisms of phase separation as a function of EC/HPC ratio: *i)* is the case *a* and *b,* when a discontinuous structure with HPC inclusions in an EC matrix

is obtained, *a* is in the metastable region and the structure is formed by nucleation and growth whereas *b* is in the unstable region and the discontinuous structure is formed by spinodal decomposition. *ii)* is the bicontinuous case *c,* formed by spinodal decomposition *iii)* is the case *d* and *e* with a discontinuous structure of EC inclusions in an HPC matrix, where *e* is formed by nucleation and growth and *d* in formed by spinodal decomposition. In Figure 42 to the right, the corresponding morphologies are illustrated, the difference from *a* and *b* and *c* and *d* is that the inclusions for *b* and *d* appear at the same time whereas for *a* and *e* the inclusions appear at different times. This also results in a wider distribution of inclusion sizes for the inclusions formed in regions *a* and *e*.

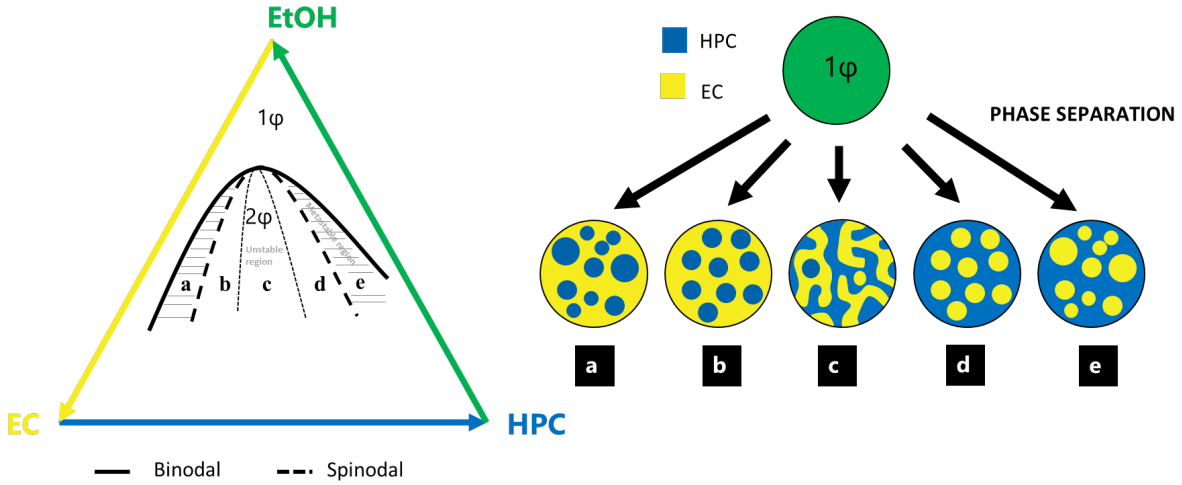

Figure 42 Schematic illustration of the possible structures that can be obtained after phase separation of EC and HPC, showing the ternary phase diagram of EC and HPC in ethanol (left) and some examples (a)-(e) of possible structures; (a) and (e) are in the metastable region, whereas (b)-(d) are in the unstable region. Further, (c) is bicontinuous whereas the rest are discontinuous.

By analyzing the structure evolution, we can estimate which mechanisms are taking place during the phase separation as a function of EC/HPC ratio. It is believed that the three cases in Figure 41 correspond to the cases in Figure 42 : Figure 42 cases *b* for the ratios 15 to 22 wt% HPC ; Figure 42 case *c* for the ratios 25 to 40 wt% HPC and to Figure 42 case *d* for the ratios 45 to 60 wt% HPC. Probably HPC 85wt% corresponds to the case *e* in Figure 42, due to the differences in inclusion sizes, but more research is needed.

On the last row of Figure 41 the micrographs corresponding to the plateau when the structure is trapped are shown. The characteristic length scale for each micrograph was calculated using image analysis and plotted *versus* the HPC ratio in Figure 43. We observe that the length scale at plateau is in the same range $L \sim 0.6 - 1.6\ \mu m$ for the discontinuous structure corresponding to the ratios 15, 20, 22, 45, 50, 55, 60, 85 wt% HPC. For the bicontinuous structures, the length scale is significantly larger, *e.g.* $L(t = \infty)_{30wt\%\ HPC} = 6.0\ \mu m$. It shows that the coarsening of phase separation taking place during the formation of bicontinuous structures is resulting in bigger structures. Another factor that is important to consider for the structure evolution is the solvent quench deep. Solvent will continuously evaporate during the progress of the phase separation, which will continuously change the position of the mixture in the phase diagram

illustrated in Figure 42. This will influence the solvent quench depth and thereby the driving forces for phase separation. Furthermore, the viscosity will change continuously during the solvent quench. Both the increased driving forces for phase separation and the viscosity change will influence the coarsening rate of the phase separated structure.

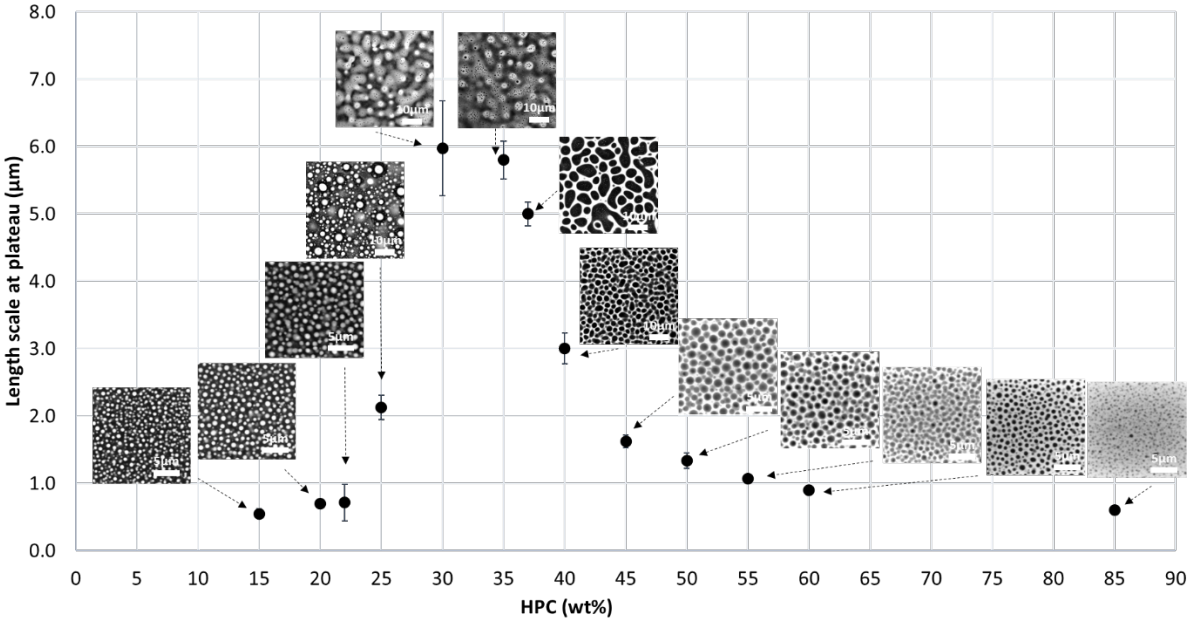

Figure 43 Length scale at plateau versus HPC ratio (m +- sd), also showing the corresponding micrographs.

Figure 44 shows the length scale time dependency and the domain growth rate of the phase-separated structure. The length scale time dependency is defined as $L(t) = at^n + c$ with a being the domain growth rate and n the time exponent. It can be noted that it is the combination of a and n that define the overall coarsening rate; larger values of both a and n will correspond to a higher growth rate. The parameters a and n were extracted from the data by performing a fit to the experimentally obtained length scales see Figure 28.

In Figure 44a, for the bicontinuous cases, ratio 25, 30, 35, 37 wt% the time exponent is close to 1, showing that the interfacial tension-driven hydrodynamic coarsening is dominating (Siggia, 1979). Films made of 40 wt% HPC are on the limit of bicontinuous structures, and the time exponent is approximately 0.7. For the discontinuous structures, the exponents are lower and closer to $1/3$ showing that the diffusive regime is having an important role in the coarsening. The exponent is approximately 0.45 for 20 wt% HPC. However, it can be noticed that for 45, 50, 50 wt% HPC, the exponent is close to 2/3. In the case of EC/HPC, the exponent $n \approx 2/3$ is observed for asymmetric systems i.e. where the volume fractions of the two polymers are far from 50:50. This is different from Datt *et. al. (Datt et al., 2015)* who used simulations to calculate the growth law exponent and found an exponent of $2/3$ for symmetric systems, whereas asymmetric systems would deviate and exhibit an exponent of $1/3$. However, the exponent value of 2/3 might show that several mechanisms are competing.

In Figure 44b the domain growth rate a is plotted *versus* the HPC ratio. The bicontinuous structures exhibit a higher growing rate ($> 0.05\ \mu m/s$), and are growing faster, meaning that the systems coarsen faster. Hence, with higher domain growth rate the final structure is

supposedly bigger. These results are in accordance with the results of Figure 43, where the length scale is bigger for the bicontinuous structure, showing that the coarsening is faster. On the contrary, the circular shapes in the discontinuous structure, mainly formed by diffusion-driven coarsening, are growing at a slower rate ($< 0.05\ \mu m/s$). It can be noticed that 40 wt% HPC has a high growth rate, which supports that 40 wt% HPC has a bicontinuous structure.

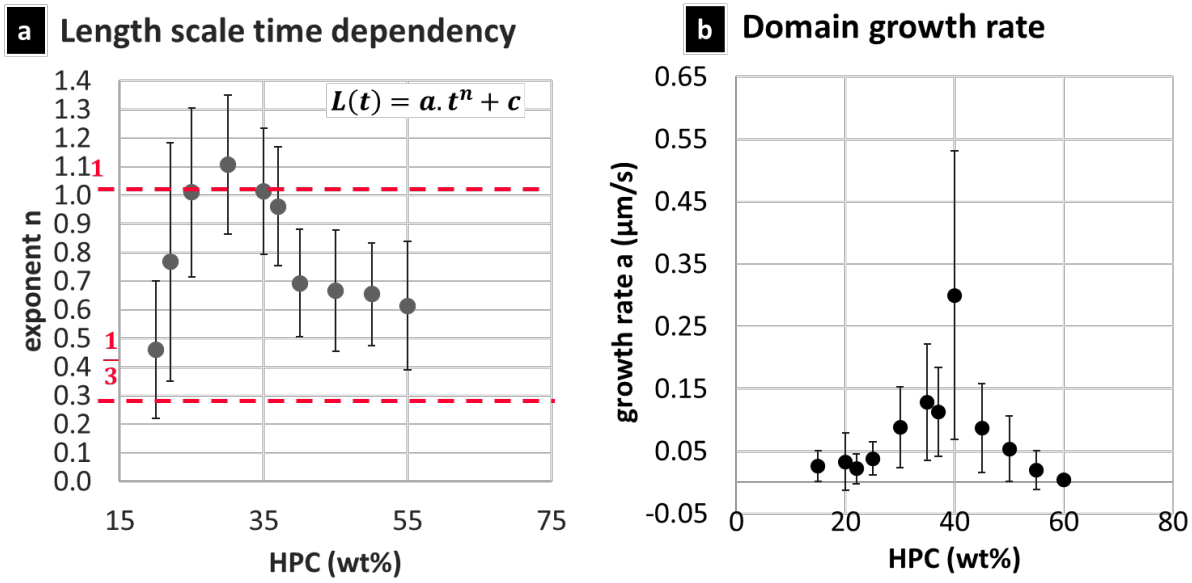

Figure 44 Time dependency analysis, showing (a) the parameter n versus the HPC ratio (m +- sd), also showing two different regimes of coarsening, the diffusive regime (1/3, bottom red dotted line) and the hydrodynamic regime (1, top dotted red line), (b) the parameter a corresponding to the domain growth rate versus the HPC ratio (m +- sd). Structure evolution in cross section

To add information on the structure evolution during phase separation, the films were observed in the xz-plane. Figure 45 shows CLSM micrographs corresponding to the structure evolution in cross section of the film for the 13 ratios at different key times of the phase separation.
The first row corresponds to a stage before the phase separation has started at $t = 35s$, the EC and HPC are in one phase, and the micrographs are grey and homogeneous. The second row corresponds to the phase separation start and some vague structures can be observed. The third row corresponds to the growth start, where the shrinkage rate linear fit starting limit is taken. The fourth row shows examples of the structure during the coarsening. The fifth row is the 'linear fit end' which corresponds to the growth end. After this point, the structure is kinetically trapped and does not grow anymore, however some shrinkage is still taking place. Finally, the sixth row is at plateau when the evaporation process is complete, and the remaining film corresponds to the solid fraction.

As for the in plane (xy-plane), Figure 45 gives a good overview of the structure evolution taking place in EC/HPC films in the cross-section plane. The thickness of the film is decreasing as a function of time. In addition, the phase separation can be observed, and particularly the coarsening. In the 5th row ("linear regime end") it can be noticed that the length scale of the phase-separated structure seems to be bigger than the film thickness for the bicontinuous cases (25, 30, 35, 37 wt% HPC). This is interesting from a structure evolution perspective, because

this means that the coarsening has gone from 3D coarsening to 2D coarsening. It is also likely that the interplay with the surrounding surfaces start to play an important role for the structure evolution.

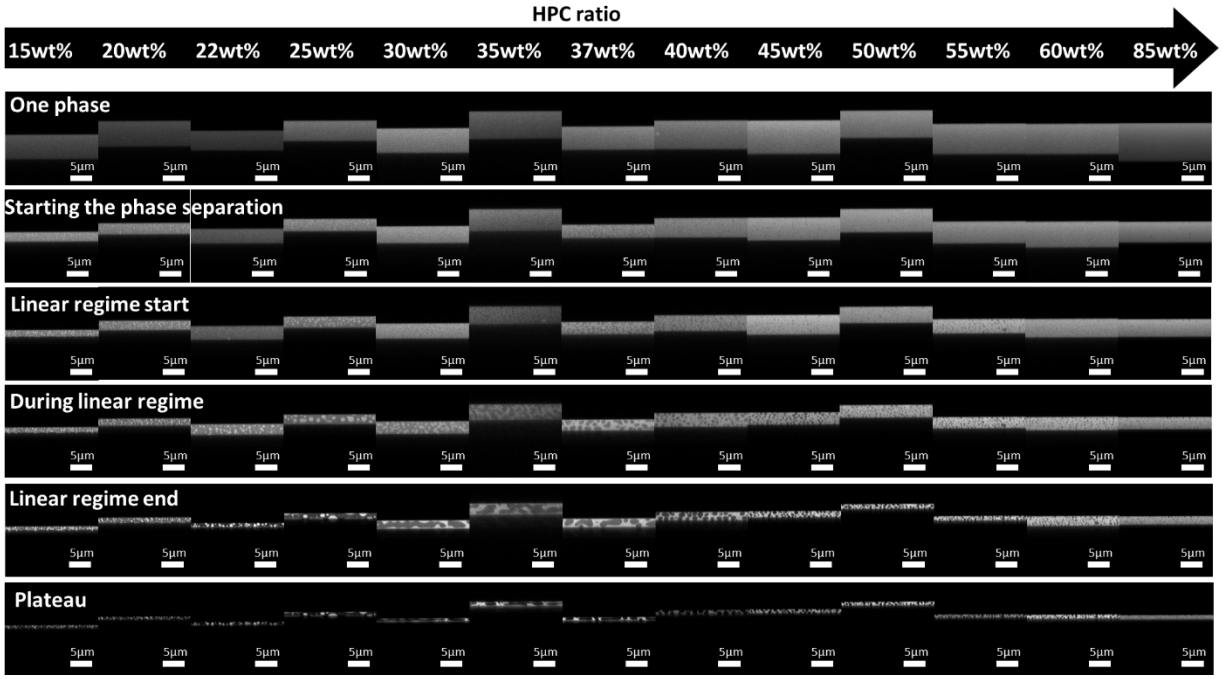

Figure 45 Overview of structure evolution in cross section of EC/HPC films at 13 EC:HPC ratio. The x axis is the HPC ratio, and the y-axis corresponds to different key times of phase separation: one phase, the start of phase separation, the start of the linear fit, during the linear regime (coarsening, at the end of the linear regime and finally at plateau, when the shrinkage has ended.

Figure 46 shows cross sections of the EC/HPC films at plateau, when the evaporation is complete for the 13 EC:HPC ratios investigated. Wetting phenomenon could be observed in the CLSM micrographs in the trapped structures. However, the wetting might start to play a role earlier than just in the end of the phase separation. The two possible wetting mechanisms (partial and complete wetting) are mainly observed for HPC concentrations between 25 and 37 wt%. The complete wetting is only observed for 30 wt% HPC. For the other compositions 25, 35, 37 wt% HPC, a partial wetting is observed. The preferential wetting that is observed can be of several origin. One possibility is that HPC has stronger affinity with the glass substrate, as the coarsening is faster, the mixture is trapped closer to the equilibrium, the EC and HPC domains have time to undergo preferential wetting. This hypothesis is supported by Zoumpouli *et. al.* (Zoumpouli and Yiantsios, 2016) that concludes that the lamellar phase separation structures are observed when preferential wetting occurs.

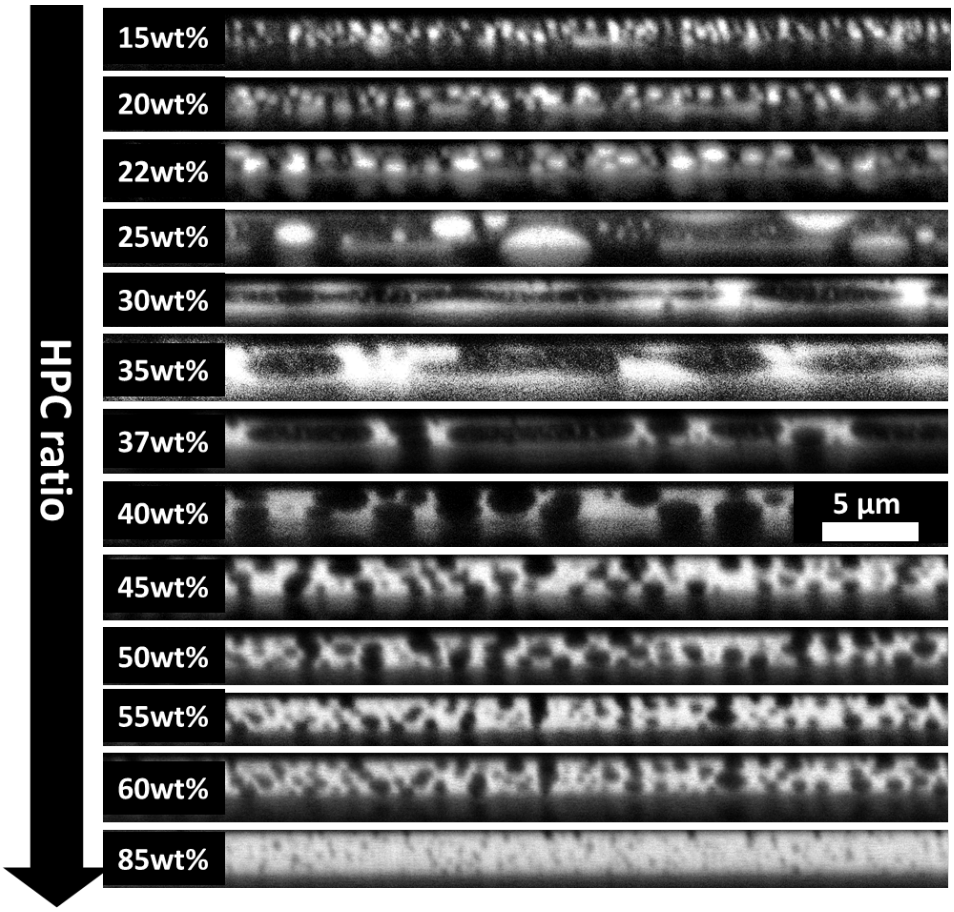

Figure 46 XZ observation of the EC/HPC film at plateau for the 13 EC:HPC ratio. The bright phase is HPC, and the dark phase is EC.

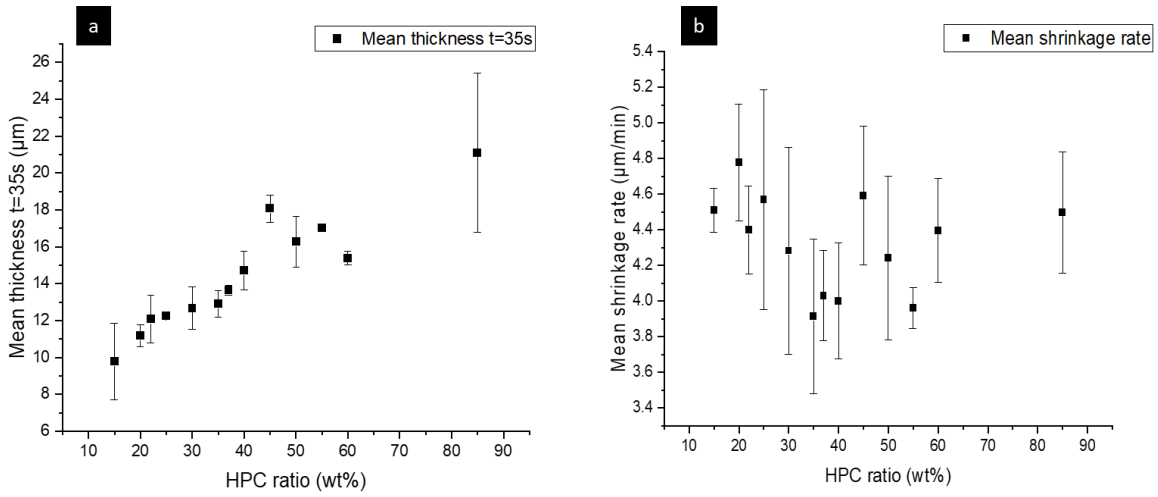

Figure 47 (a) mean thickness at 35s after spin-coating at 2000RPM for 3s for different EC/HPC ratios; (b) mean shrinkage rate. The error bars represent the standard deviation.

Figure 47 shows the mean film thickness and the mean shrinkage rate *versus* the HPC ratio. The film thickness was determined from CLSM micrographs of the cross sections using image

analysis. Figure 47a is the film thickness $at\ t = 35s$ before the phase separation has started. We observe that the thickness of the film after spinning is increasing with the ratio of HPC. Our hypothesis is that this depends on the viscosity of the polymer mixture, which is higher with higher content of HPC in the blend. During spin coating a lot of material is spread away on the side and only a fraction of it remains in the center of the substrate. With higher viscosity more material is remaining, and a thicker film is formed.
Figure 47b shows the mean shrinkage rate. A multiple comparison test using Tukey's honestly significant difference (HSD) criterion was used, indicating that none of the pairwise differences in mean shrinkage rate between the HPC fractions were significant ($p > 0.3$). Our hypothesis is that the shrinkage rate is independent of the HPC ratio and mainly depends on the evaporation process.

5.4.2 Curvature evolution

To investigate the role of curvature for the hydrodynamic coarsening, we studied the curvature evolution. It was seen in Figure 44 that the time dependency of the film formation for bicontinuous structures were close to 1, which is a strong indication of hydrodynamic coarsening.

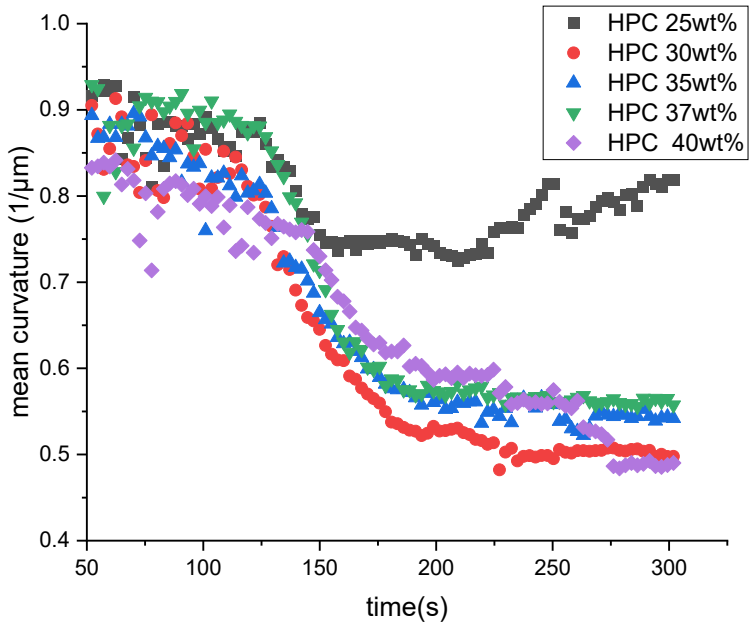

Figure 48 Mean curvature versus time for the EC:HPC ratio: 25, 30, 35, 37, 40 wt% HPC.

Figure 48 shows the time-dependent evolution of the mean curvature (average of three replicates) for the bicontinuous structures, where the interfacial tension driven mechanisms of coarsening are expected to dominate. We observe in Figure 48 that the curvature in the early stage of phase separation (t =100-120s) is high for the whole set of ratios (in the range 0.8. – 0.9 μm^{-1}), signifying that a lot of small radiuses are present at the interface between EC and HPC. Between 140 and 200s the growing rate is high, and the shape of the structure is changing rapidly. The curvature is decreasing and at about 250s a plateau is reached due to kinetic

trapping of the structure. This behavior is observed for the ratio 30, 35, 37 and 40 wt% HPC, where the structure is clearly bicontinuous. For HPC 25wt%, which is at the limit between bicontinuous and discontinuous, the drop of curvature is less pronounced. However, Figure 44 shows that for HPC 25wt% the time exponent, *b*, is close to 1 supporting that the growth mechanism is interfacial tension driven hydrodynamic coarsening. Probably different mechanisms are competing, but hydrodynamic coarsening seems to be the main mechanism of coarsening.

5.4.3 Rheology of EC/HPC solutions

The effect of HPC concentration and polymer concentration on the viscosity of the polymer solutions were investigated using rheology. The measured samples contained 22, 30, 45 and 60 wt% HPC. Furthermore, solutions with different decreasing solvent content were investigated to evaluate the increase of viscosity during ethanol evaporation because this will influence coarsening rate and kinetic trapping of the phase-separated structure. Figure 49a shows the zero-shear viscosity *versus* the ratio of HPC in the polymer blend at 6 wt% total polymer concentration in the stock solutions for the four compositions of 22, 30, 45, 60 wt% HPC. The value for the viscosity at zero shear rate was approximated from the viscosity at the Newtonian plateau (Barnes, 2000, Shaw and Macknight, 2005).

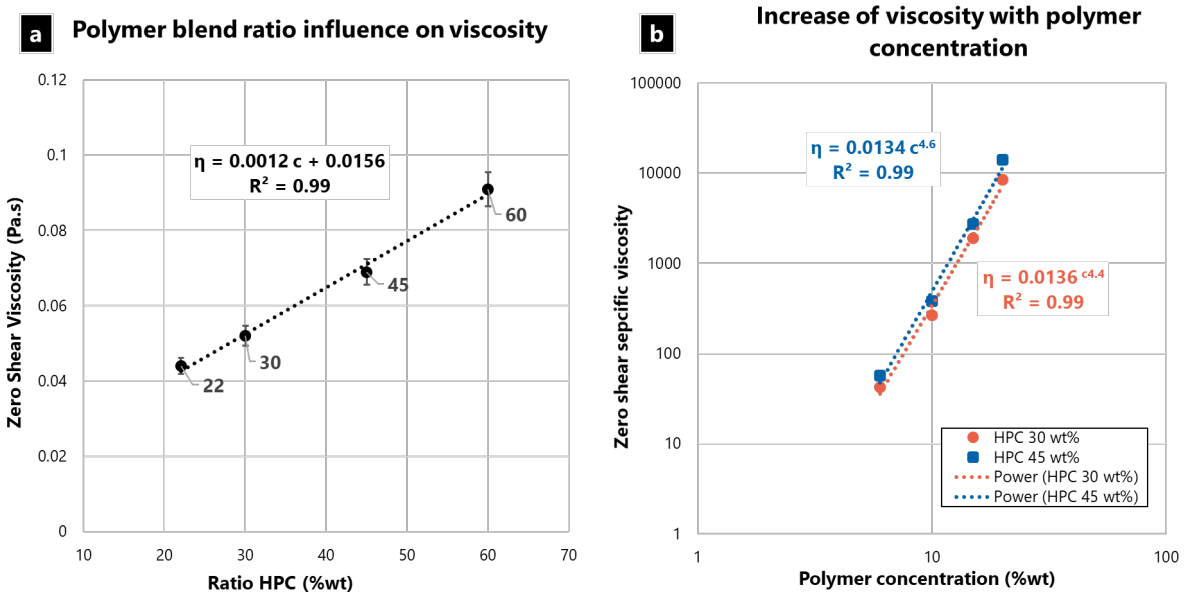

Figure 49 Rheology measurements on EC/HPC systems. a) Zero-shear viscosity versus the HPC ratio in the polymer blend. The solutions were the stock solutions with 6 wt% polymer in 94 wt% ethanol. The error bar represents the standard deviation. b) Zero-shear specific viscosity as a function of polymer concentration.

Figure 49b shows the zero-shear specific viscosity *versus* the polymer concentration. The choice of the specific viscosity in this plot was made to correlate the slope with previous values in the literature. In Figure 49a, the viscosities of different EC/HPC solutions increase linearly with the increase of HPC wt% in the polymer blend. This result can be explained by the average molecular weight values of HPC, and EC used. The molecular weight of HPC is considerably

higher than the molecular weight of EC. The entanglements between the polymer chains are higher when increasing the HPC ratio, resulting in an increase of viscosity (De Gennes, 1979).

Rheology measurements displayed in Figure 49b show that the viscosity is increasing significantly with increased evaporation of ethanol in the solution (*i.e.* increasing polymer concentration). The logarithmic plot of the zero-shear specific viscosity *versus* the polymer concentration was fitted with a power law. Bercea *et al.* (Bercea and Navard, 2018) studied the viscosity of HPC solution with molecular weights in the range of 80 to 1050 kDa. They plotted the specific viscosity as a function of c·[η], where c is the polymer concentration and [η] the intrinsic viscosity calculated from the Mark-Houwink dependence. In the entangled regime (De Gennes, 1979), Bercea *et al.* (Bercea and Navard, 2018) found a slope of 4. By estimating the intrinsic viscosity of our system with the HPC intrinsic viscosity reported for HPC in aqueous solutions at 25°C 55, c·[η] was calculated and the specific viscosity plotted *versus* c·[η]. The slope found exhibits nearly the same exponents: 4.4 for 30 wt% HPC and 4.6 for 45wt% HPC. Thus, the exponents found in this work coincide well with the ones reported earlier for HPC solutions. The plot in Figure 49b can also be used to estimate the rate of viscosity increase during evaporation. The rheological data helps us to understand the kinetic trapping: with ethanol evaporation, the viscosity increases drastically, trapping the structure during the phase separation process (Schaefer *et al.*, 2016). The increase of viscosity as a function of increasing of HPC ratio that is shown in Figure 49b is not so pronounced compared to the high increase of viscosity during evaporation shown in Figure 49b. Thus, the main parameters responsible for the kinetical trapping are the total polymer concentration and the ethanol evaporation rate. Thus, it is interesting to investigate the content of ethanol at the time corresponding to the start of the phase separation and the kinetical trapping.

5.4.4 Estimation of the phase diagram from solvent evaporation

In the following part, we use the information from the cross section (xz-plane) observation to estimate the ethanol content at each time. We assume that the evaporation process is complete at the plateau when the shrinkage is finished. Hence the thickness over time is providing information about the ethanol fraction for each micrograph. The mean volume fraction of solid material is given by the final thickness divided by the current thickness: $\varphi_S = \frac{h_{dry}}{h[t]}$ and the fraction of ethanol is $\varphi_{EtOH} = 1 - \varphi_S$ (van Franeker *et al.*, 2015). Figure 50 shows the ethanol fraction and the solid fraction *versus* the HPC ratio. In Figure 50b, the ethanol concentration at the start of phase separation is highest around 45 and 50 wt% HPC. It can also be noticed that the ethanol concentration at the end of growth is varying a lot and that it is low for low HPC concentration. This might indicate that it is hard to judge exactly then the structure is trapped and the growth period has ended. There also seem to be a trend that the ethanol concentration at the end of growth is increasing with increasing HPC concentration, which might be an effect of the viscosity increase originating from increased concentration of HPC (see Figure 49a).

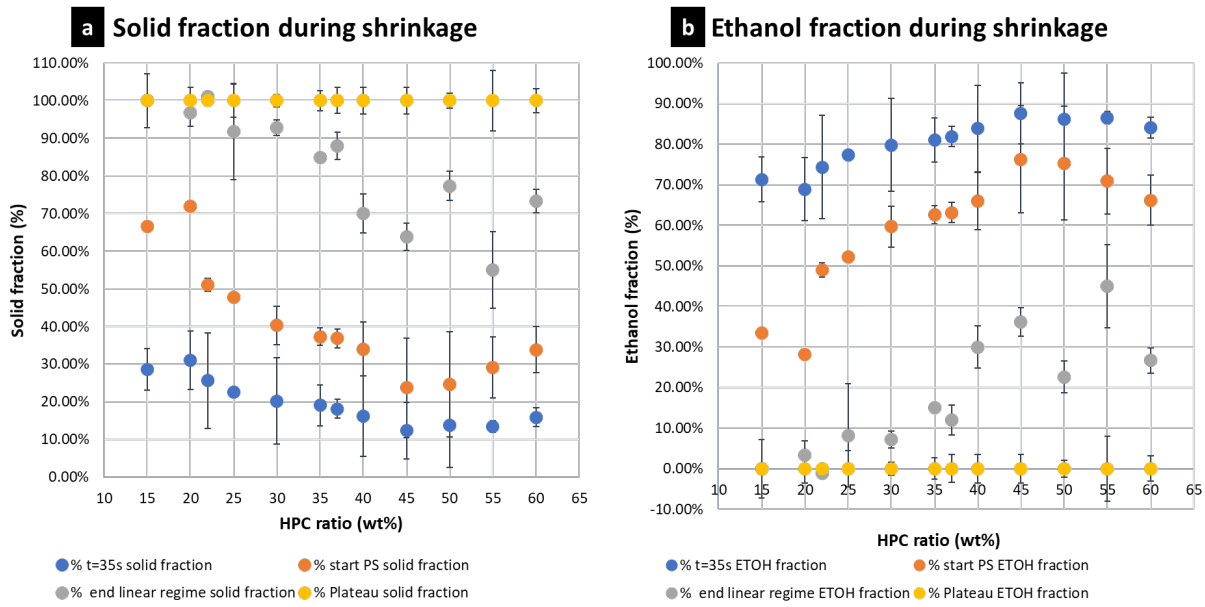

Figure 50 (a) Solid fraction versus the HPC ratio considering that at plateau the solid fraction is 100%. (b) Ethanol fraction versus the HPC ratio, considering that at plateau the ethanol fraction is 0%. The error bars represent the standard deviation.

By taking the curve $\varphi_{EtOH}(PS\ start) = f(\%HPC)$, we can estimate the position of the spinodal curve in the ternary phase diagram EC/HPC/EtOH. We speculate that it is the spinodal curve that is determined, because the metastable region in this system is probably rather small (Debenedetti, 2000).

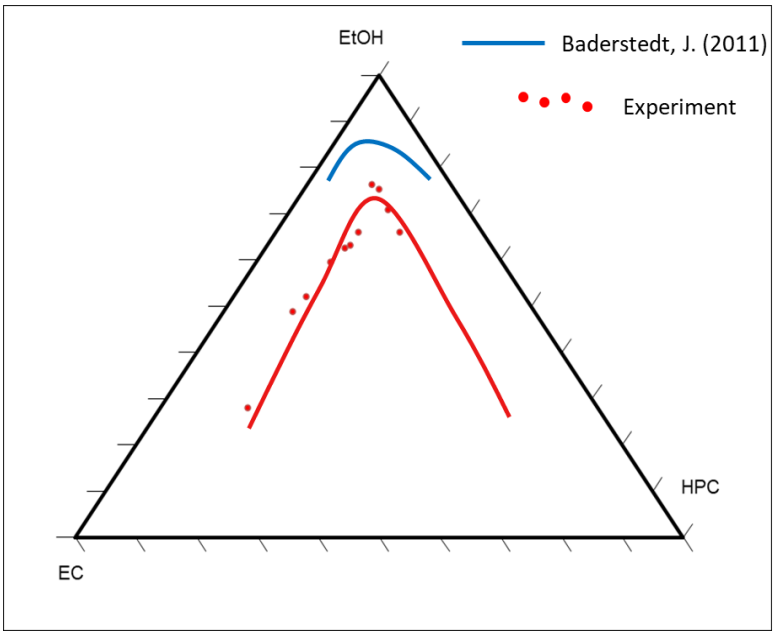

Figure 51 Estimated phase diagram of EC HPC in EtOH. Binodal (blue from Baderstedt, 2011) and spinodal estimated from the cross-section height in CLSM micrographs (red).

Figure 51 is showing a plot of the estimated phase diagram. The blue curve corresponds to the binodal curve determined experimentally in previous work by Baderstedt *et al.* They studied the phase separation in EC/HPC solutions by letting EC/HPC mixture of different composition

rest in closed vials for at least one month (Baderstedt, 2011). By visual inspection of the meniscus, they could determine at which composition the mixture would phase separate and hence, estimate the binodal curve.
The result of Figure 50b, the curve $\varphi_{EtOH}(PS\ start) = f(\%HPC)$, is plotted in the EtOH/EC/HPC phase diagram in Figure 51. We observe that the shape of the spinodal obtained experimentally corresponds to a typical spinodal shape and that it is located below the binodal. However, it is probably little shifted toward lower EtOH content due to the spatial resolution of CLSM and the concentration (intensity) differences needed to observe the phase separation. This study of the kinetics gave us a good overview of the structure formation kinetics and the influence of the EC:HPC ratio on a single layer. However, to further explore the mimicking of the industrial process, we would like to investigate multilayered films when coating successive layers of EC/HPC.

5.5 Structure of multi-layered phase-separated films

The aim of this section was to investigate the feasibility of producing multilayer films, and to identify the spin-coated layers with CLSM and image analysis. In addition, it is interesting to investigate how the spraying of a new layer interacts with an already present layer *i.e.* templating and/or re-wetting.
Our hypothesis is that by coating successive layers, the system might undergo what we are calling a templating. We give an illustration of this effect in Figure 52. In Figure 52a, the second layer is formed, and the pattern (alternation of EC and HPC domains) is independent of the first layer pattern. In Figure 52b, the large affinity of HPC to HPC and EC to EC is making the structure of the second layer similar to the first layer.

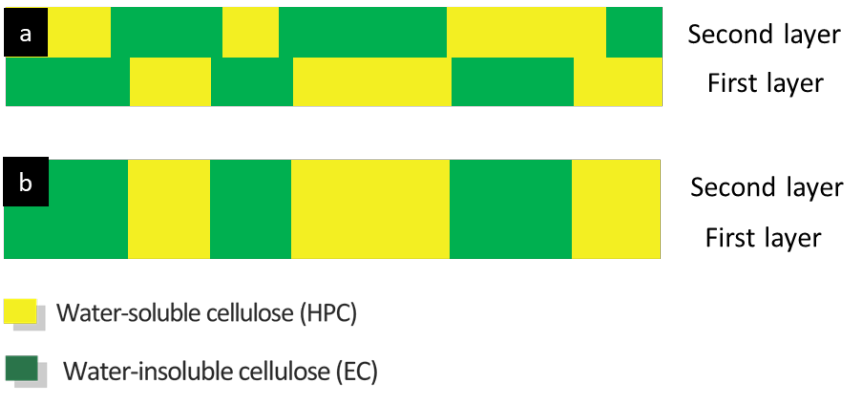

Figure 52 Schematic illustration of the templating effect (a) no templating effect between the first and the second layer (b) templating effect between the first and the second layer.

The re-wetting effect happens when a layer of wet solution is entering in contact with dried material underneath (already dried and formed layer). The ethanol contained in the wet layer will dissolve some of the dried EC/HPC and the dissolution might change the structure. For example, the coarsening might continue, leading to a bigger structure.
In previous work, the complex structure of EC/HPC coating was imaged using FIB-SEM and reconstructed (Fager *et al.*, 2020a). Image analysis of the coating structure was performed using MIST. MIST is an open source software that was developed by Barman *et al.* (Barman, 2020). Quantitative data, such as porosity, connectivity and tortuosity have been extracted from the

3D reconstructions. It was found (Fager *et al.*, 2021) that the structure of the industrial pellets are layered (see Figure 33), meaning that layers with the same porosity can be observed but no gradient from the core to the surface could be observed. In the industrial pellet there is an alternance between the typical size in the different layers.

In this work, ImageJ was utilized to reconstruct the 3D structure from the CLSM micrographs. Figure 53 shows a 3D reconstruction of a thin film made of 20 layers spin coated successively at 2000 RPM during 45s (each layer was spined during 45s) for 45 wt% HPC. In the cross sections (xz-plane), a gradient can be observed. The structure is bigger close to the glass surface compared to the air surface.

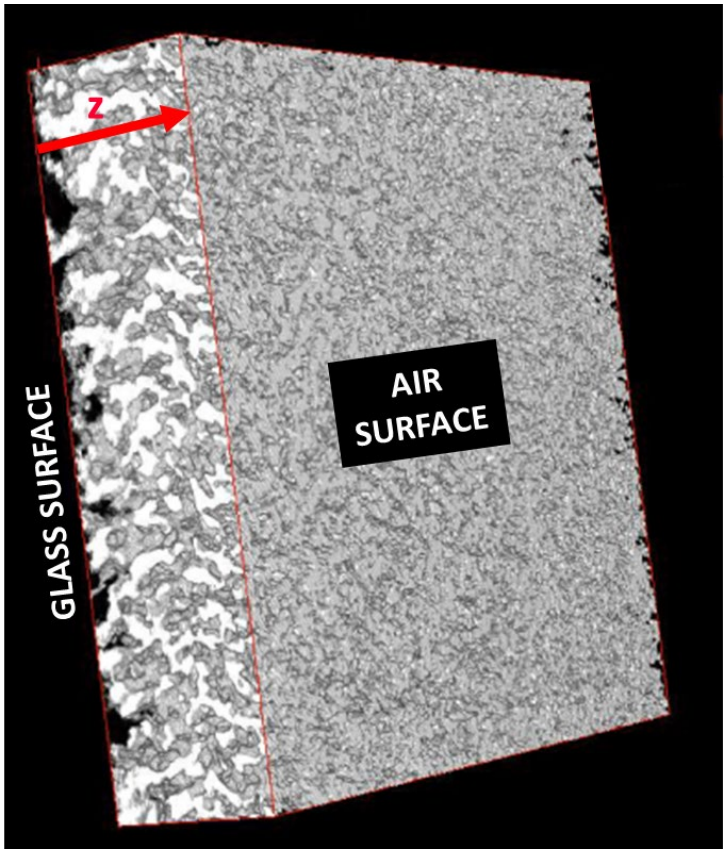

Figure 53 3D reconstruction of a multi-layered film (45 wt% HPC) with 20 layers spin-coated successively. HPC is the bright phase and EC the dark phase.

Figure 54 is showing the length scale measured by Fourier image analysis through the 20 layers shown in Figure 53. The CLSM analysis of the film was performed every 5 layers and the corresponding curve is plotted *versus* the height in the film: every fifth layer was coated, the sample was analyzed with CLSM in the xyz plane, and the image analysis was performed. Hence, we obtain curves for the films with 5,10,15 and 20 layers. It can be observed that the length scale is decreasing with increasing number of layers. It can also be noted as a general trend that the length scale is oscillating. Our hypothesis is that each local maximum is corresponding to one layer, and by counting them, we find back the 20 layers (the numbers are provided in Figure 54).

We observe a gradient from the substrate to the air surface confirming what was seen in the 3D reconstruction in Figure 53. The gradient starts from $L = 5\mu m$ at the substrate surface to $L = 1.9\ \mu m$, which approximately corresponds to the length scale of the dried film (45 wt% HPC, spin coated at 2000 RPM for 45 s) determined in Carmona *et al.* (Carmona *et al.*, 2021).
No templating is observed. However, re-wetting might cause the gradient. One might speculate that the dried layer underneath the new wet layer is receiving new ethanol, re-wetting of the underneath layer is taking place. Consequently, the phase separation and the coarsening can continue, resulting in bigger structure. The layers close to the substrate surface are re-wetted several times, explaining the large increase of structure size compared to the size that was observed for a single layer.

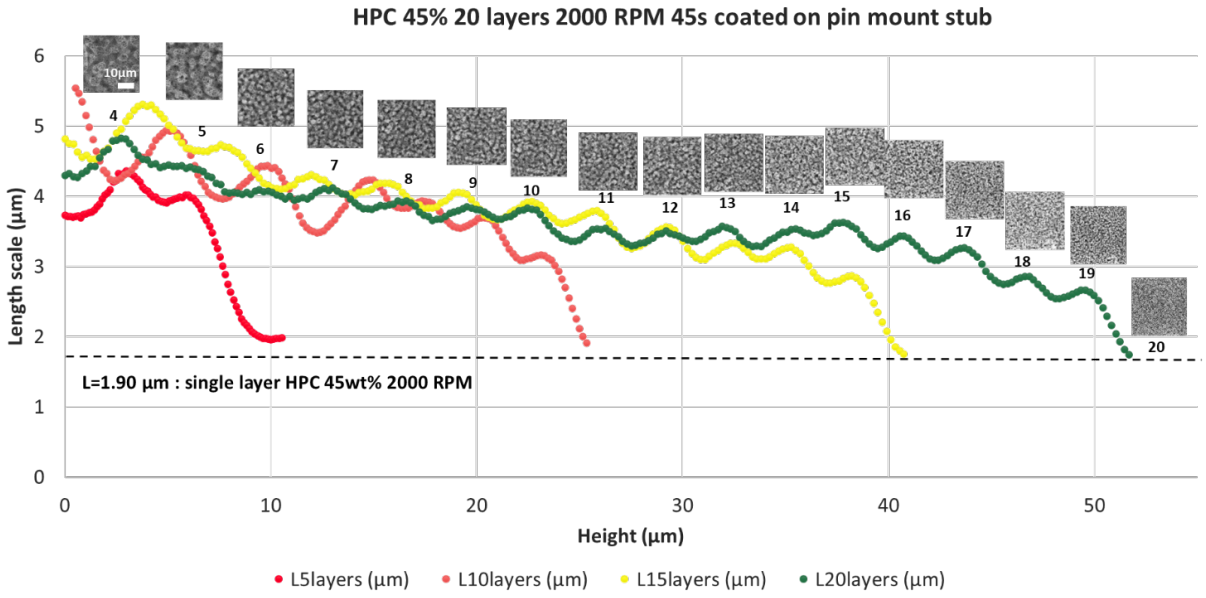

Figure 54 Length scale versus the height in a HPC 45wt% with 20 layers films. The numbers represent the layer number, and the corresponding CLSM micrograph is located above.

6 Conclusions

It was found that the combination of confocal laser scanning microscopy, image analysis, rheology and profilometry is powerful to investigate spin-coated phase-separated films made of EC/HPC. The spin-coating technique provided good control and reproducibility of the final structures. Fourier image analysis was used to determine the characteristic length scale of the bicontinuous phase-separated structure. The effect of spin-coating parameters on the final structure of the phase-separated spin-coated EC/HPC films, as a function of composition (ratio EC:HPC), was determined. The results showed that the final characteristic length scale decreases with increasing spin speed. In addition, the film thickness decreases with increasing spin speed. Spin curves were established and power law exponent close to -0.5 was found for all compositions. Finally, a strong correlation between thickness and spin speed was found for 22 wt% HPC, 30 wt% HPC and 45 wt% HPC.

An experimental set up was developed and optimized to observe the phase separation of the EC/HPC system *in situ* using CLSM. A wet homogeneous film was formed by spin coating for 3s in a petri dish. By closing the lid of the petri dish, the phase separation process was slowed down, allowing for characterization of the evolution of the phase-separated structure. Determination of the structure evolution was performed both in the in plane (xy) and cross section (xz) directions using CLSM. The xyt CLSM micrograph-series, enabled the observation of the phase separation evolution in the xy-plane (plane of interest for the determination of the characteristic length scale), while the xzt micrograph-series made it possible to follow the decrease of the film thickness and the evolution of the phase separation in the z direction (through the film). By comparing the structure evolution in xy and xz, it was noticed that the phase separation occurs at first in a 3D system that develops into a thin 2D-like system. At some point of the phase separation, the characteristic length scale became larger than the film thickness for some compositions. This was pronounced for the bicontinuous systems.

Information about the phase separation kinetics provided further understanding of the processes controlling the phase-separated structure of thin EC/HPC films. The influence of the EC:HPC ratio on the final structure was determined and two cases were identified, the bicontinuous and the discontinuous case. Each case was related to a coarsening regime, hydrodynamic regime with hydrodynamic coarsening and high growth rate for the bicontinuous structure. A diffusive regime with coalescence and smaller structures for the discontinuous structure were identified. From the xzt micrographs-series, the shrinkage rate was extracted, which allowed an estimation of the evaporation rate. The xzt-observations allowed the estimation of the ethanol content at each time and the extraction of information about the spinodal curve in the phase diagram. In addition, preferential wetting was observed for the bicontinuous structures.

The spin coating technique was used to make phase separated EC/HPC films with multiple layers. The 3D structure was reconstructed by taking micrographs at different depths using CLSM. It was possible to identify successive layers and estimate the thickness and the length scale of each layer. A gradient in structure domain size was observed when going from the substrate surface to the air surface. The structures were bigger close to the glass surface. More

detailed analysis and experiment need to be performed to identify the additional phenomena that are occurring during the layering. To mimic the industrial process, we need to understand fully the interaction between the layers and how the control of the spin speed and the time between subsequent layers can be used to design the layers.

7 Future Outlook

The next steps in this work are to continue to investigate the kinetics of phase separation, to investigate the formation of multilayer structures, and to evaluate the influence of composition and processing on the structure evolution. We plan to characterize the structure of successive spin coated layers with optimized parameters determined in the single layer study. We also intend to investigate the effects of time between the deposition of layers, droplet volume, atmosphere, temperature, and different spinning speed and time.

Further, we are also planning to use electron microscopy, *i.e.* environmental scanning electron microscope (ESEM) and or combined focused ion beam and scanning electron microscope (FIB-SEM), to investigate the microstructure of multilayered structures at higher spatial resolution, and to compare that structure with the structure evolution obtained using CLSM.

REFERENCES

AARTS, D. G. A. L., LEKKERKERKER, H. N. W., GUO, H., WEGDAM, G. H. & BONN, D. 2005. Hydrodynamics of Droplet Coalescence. *Physical Review Letters,* 95.

ANDERSSON, H., HÄBEL, H., OLSSON, A., SANDHAGEN, S., VON CORSWANT, C., HJÄRTSTAM, J., PERSSON, M., STADING, M. & LARSSON, A. 2016. The influence of the molecular weight of the water-soluble polymer on phase-separated films for controlled release. *Int J Pharm,* 511**,** 223-235.

ANDERSSON, H., HJÄRTSTAM, J., STADING, M., VON CORSWANT, C. & LARSSON, A. 2013. Effects of molecular weight on permeability and microstructure of mixed ethyl-hydroxypropyl-cellulose films. *Eur J Pharm Sci,* 48**,** 240-8.

ANDERSSON, H., MARUCCI, M., HJÄRTSTAM, J., STADING, M., VON CORSWANT, C. & LARSSON, A. 2009. New insights into the effects of polymer molecular weight on release mechanisms through polymer blend coatings. *Eur J Pharm Biopharm,* 83**,** 301-6.

ANDERSSON, H., ÖHGREN, C., JOHANSSON, D., KNIOLA, M. & STADING, M. 2011. Extensional flow, viscoelasticity and baking performance of gluten-free zein-starch doughs supplemented with hydrocolloids. *Food Hydrocolloids,* 25**,** 1587-1595.

ASHLAND. 2017. *Klucel hydroxypropylcellulose, Physical and chemical properties* [Online]. USA. [Accessed].

BADERSTEDT, J. 2011. *The effect of molecular weight on the performance of ethyl cellulose membranes.* Master of Science Thesis, CHALMERS UNIVERSITY OF TECHNOLOGY.

BAILEY, A. E., POON, W. C., CHRISTIANSON, R. J., SCHOFIELD, A. B., GASSER, U., PRASAD, V., MANLEY, S., SEGRE, P. N., CIPELLETTI, L., MEYER, W. V., DOHERTY, M. P., SANKARAN, S., JANKOVSKY, A. L., SHILEY, W. L., BOWEN, J. P., EGGERS, J. C., KURTA, C., LORIK, T., JR., PUSEY, P. N. & WEITZ, D. A. 2007. Spinodal decomposition in a model colloid-polymer mixture in microgravity. *Phys Rev Lett,* 99**,** 205701.

BARBERO, N., BARNI, E., BAROLO, C., QUAGLIOTTO, P., VISCARDI, G., NAPIONE, L., PAVAN, S. & BUSSOLINO, F. 2009. A study of the interaction between fluorescein sodium salt and bovine serum albumin by steady-state fluorescence. *Dyes and Pigments,* 80**,** 307-313.

BARMAN, S. 2020. *The pore geometry of pharmaceutical coatings: statistical modelling, characterization methods and transport prediction.* DOCTOR OF PHILOSOPHY, Chalmers University of Technology.

BARNES, H. 2000. *Handbook of Elementary Rheology,* University of Wales.

BASSOU, N. & RHARBI, Y. 2009. Role of Benard-Marangoni instabilities during solvent evaporation in polymer surface corrugations. *Langmuir,* 25**,** 624-32.

BERCEA, M. & NAVARD, P. 2018. Viscosity of Hydroxypropyl Cellulose Solutions in Non-Entangled and Entangled Stated. *Cellulose Chemistry and Technology,* 52**,** 603-608.

BINDER, K. & STAUFFER, D. 1974. Theory for slowing down of the relaxation and spinodal decomposition of binary mixtures. *Phys. rev. letters,* 33**,** 1006-1009.

BIRNIE, D. P. 2011. Rational solvent selection strategies to combat striation formation during spin coating of thin films. *Journal of Materials Research,* 16**,** 1145-1154.

BIRNIE, D. P. & MANLEY, M. 1997. Combined flow and evaporation of fluid on a spinning disk. *Physics of Fluids,* 9**,** 870-875.

BOUTTES, D., LAMBERT, O., CLAIREAUX, C., WOELFFEL, W., DALMAS, D., GOUILLART, E., LHUISSIER, P., SALVO, L., BOLLER, E. & VANDEMBROUCQ,

D. 2015. Hydrodynamic coarsening in phase-separated silicate melts. *Acta Materialia,* 92**,** 233-242.

BRAY, A. J. 2003. Coarsening dynamics of phase separating systems. *Phil. Trans. R. Soc. Lond. A*

BRAY, A. J. 2010. Theory of phase-ordering kinetics. *Advances in Physics,* 51**,** 481-587.

BUXTON, G. A. & CLARKE, N. 2007. Ordering polymer blend morphologies via solvent evaporation. *Europhysics Letters (EPL),* 78**,** 56006.

CAHN, J. W. 1965. Phase separation by spinodal decomposition in isotropic systems. *J. Chem. Phys.,* 42**,** 93-99.

CARMONA, P., RÖDING, M., SÄRKKÄ, A., VON CORSWANT, C., OLSSON, E. & LORÉN, N. 2021. Structure evolution during phase separation in spin-coated ethylcellulose/hydroxypropylcellulose films. *Soft Matter***,** 3913-3922.

CHESTERS, A. K. 1991. The modelling of coalescence processes in fluid-liquid dispersions : a review of current understanding. *Chemical Engineering Research and Design,* 69**,** 259-270.

CLARK, A. H. 1995. Kinetics of demixing. *Biopolymer Mixtures.* Nottingham University Press.

COEURJOLLY, D. & SVENSSON, S. 2003. Estimation of Curvature along Curves with Application to Fibres in 3D Images of Paper. *SCIA'03: Proceedings of the 13th Scandinavian conference on Image analysis.*

CUMMINGS, J., LOWENGRUB, J. S., SUMPTER, B. G., WISE, S. M. & KUMAR, R. 2018. Modelling solvent evaporation during thin film formation in phase separating polymer mixtures. *Soft Matter,* 14**,** 1833-1846.

DANDAPAT, B. S., SANTRA, B. & KITAMURA, A. 2005. Thermal effects on film development during spin coating. *Physics of Fluids,* 17.

DAS, N. C. 2014. Phase behaviour and separation kinetics of polymer blends. *J Microsc,* 253**,** 198-203.

DATT, C., THAMPI, S. P. & GOVINDARAJAN, R. 2015. Morphological evolution of domains in spinodal decomposition. *Physical Review E,* 91.

DE GENNES, P. G. 1979. *Scaling concepts in polymer physics,* Ithaca and London, Cornell University Press.

DE GENNES, P. G. 1985. Wetting: statics and dynamics. *Reviews of Modern Physics,* 57**,** 827-863.

DE GENNES, P. G. 2001. Instabilities during the evaporation of a film: Non-glassy polymer + volatile solvent. *The European Physical Journal E,* 6**,** 421-424.

DE GENNES, P. G. 2002. Solvent evaporation of spin cast films: “crust” effects. *The European Physical Journal E,* 7**,** 31-34.

DE GENNES, P. G., BROCHARD-WYART, F. & QUERE, D. 2004. *Capillarity and Wetting Phenomena: Drops, Bubbles, Pearls, Waves*

DEBENEDETTI, P. G. 2000. Phase separation by nucleation and by spinodal decomposition: fundamentals. *In:* PUBLISHERS, K. A. (ed.) *Supercritical Fluids.* E. Kiran et al.

DEPREZ, J. 2016. *Dynamic and Microscturcure in Porous Polymer Films.* Master Master Thesis, Ghent University.

DHONT, J. K. G. 1996. Spinodal decomposition of colloids in the initial and intermediate stages. *The Journal of Chemical Physics,* 105**,** 5112-5125.

DONATO, L., GARNIER, C., NOVALES, B., DURAND, S. & DOUBLIER, J.-L. 2005. Heat-Induced Gelation of Bovine Serum Albumin/Low-Methoxyl Pectin Systems and the Effect of Calcium Ions. *Biomacromolecules,* 6**,** 374-385.

DOWCELLULOSICS. 2005. *ETHOCEL, Ethylcellulose Polymers Technical Handbook* [Online]. USA. [Accessed].

DUNBAR, A. D., MOKARIAN-TABARI, P., PARNELL, A. J., MARTIN, S. J., SKODA, M. W. & JONES, R. A. 2010. A solution concentration dependent transition from self-stratification to lateral phase separation in spin-cast PS:d-PMMA thin films. *Eur Phys J E Soft Matter,* 31**,** 369-75.

EBBENS, S., HODGKINSON, R., PARNELL, A. J., DUNBAR, A., MARTIN, S. J., TOPHAM, P. D., CLARKE, N. & HOWSE, J. R. 2011. InSitu Imaging and Height Reconstruction of Phase Separation Processes in Polymer Blends during Spin Coating. *ACS Nano,* 5**,** 5124-5131.

EDSBÄCKER, S., BENGTSSON, B., LARSSON, P., LUNDIN, P., NILSSON, Å., ULMIUS, J. & WOLLMER, P. 2003. A pharmacoscintigraphic evaluation of oral budesonide given as controlled-release (Entocort) capsules. *Alimentary Pharmacology & Therapeutics,* 17**,** 525-536.

EL KHOURY, D. 2017. *Towards the use of Electrostatic Force Microscopy to study interphases in nanodielectric materials.* PhD, Grenoble University, Grenoble, France.

FAGER, C. 2018. *3D Reconstruction of Porous and Poorly Conductible Soft Materials using FIB-SEM Tomography.* Licentiate thesis Licentiate of engineering, Chalmers University of Technology.

FAGER, C., BARMAN, S., RÖDING, M., OLSSON, A., LORÉN, N., VON CORSWANT, C., BOLIN, D., ROOTZEN, H. & OLSSON, E. 2020a. 3D high spatial resolution visualisation and quantification of interconnectivity in polymer films. *Int J Pharm,* 587**,** 119622.

FAGER, C., RÖDING, M., OLSSON, A., LORÉN, N., VON CORSWANT, C., SARKKA, A. & OLSSON, E. 2020b. Optimization of FIB-SEM Tomography and Reconstruction for Soft, Porous, and Poorly Conducting Materials. *Microsc Microanal,* 26**,** 837-845.

FAGER, C., VON CORSWANT, C., RÖDING, M., VIRIDÉN, A., JOHANSSON, M.-O., OLSSON, A., LORÉN, N. & OLSSON, E. 2021. Correlating release properties with porous structure of pellet coatings used for controlled drug release. . *In:* MANUSCRIPT (ed.) *International Journal of Pharmaceutics.* .

FANG, L., WEI, M., BARRY, C. & MEAD, J. 2010. Effect of Spin Speed and Solution Concentration on the Directed Assembly of Polymer Blends. *Macromolecules,* 43**,** 9747-9753.

FIROOZMAND, H., MURRAY, B. S. & DICKINSON, E. 2012. Microstructure and elastic modulus of mixed gels of gelatin+oxidized starch: Effect of pH. *Food Hydrocolloids,* 26**,** 286-292.

FISCHER, H., MURRAY, M., KELLER, A. & ODELL, J. A. 1995. On the phase diagram of the system hydroxypropylcellulose-water. *Journal of Materials Science,* 30**,** 4623-4627.

FOWLER, P. D., RUSCHER, C., MCGRAW, J. D., FORREST, J. A. & DALNOKI-VERESS, K. 2016. Controlling Marangoni-induced instabilities in spin-cast polymer films: How to prepare uniform films. *Eur Phys J E Soft Matter,* 39**,** 90.

FOX, S. C., LI, B., XU, D. & EDGAR, K. J. 2011. Regioselective Esterification and Etherification of Cellulose: A Review. *Biomacromolecules,* 12**,** 1956-1972.

FUJITA, T. & CHEN, M. 2018. Erratum: "Characteristic Length Scale of Bicontinuous Nanoporous Structure by Fast Fourier Transform". *Japanese Journal of Applied Physics,* 57.

FURUKAWA, H. 1985. A dynamic scaling assumption for phase separation. *Advances in Physics,* 34**,** 703-750.

GEBÄCK, T., MARUCCI, M., BOISSIER, C., ARNEHED, J. & HEINTZ, A. 2015. Investigation of the Effect of the Tortuous Pore Structure on Water Diffusion through a Polymer Film Using Lattice Boltzmann Simulations. *The Journal of Physical Chemistry B,* 119**,** 5220-5227.

GIBBS, J. W. 1961. *The Scientific Papers of J. Willard Gibbs,* Dover, New York.
GUPTA, H., BHANDARI, D. & SHARMA, A. 2009. Recent Trends in Oral Drug Delivery: A Review. *Recent Patents on Drug Delivery & Formulation,* 3**,** 162-173.
HASHIMOTO, T. 1988. Dynamics in spinodal decomposition of polymer mixtures. *Phase Transitions,* 12**,** 47-119.
HERIOT, S. Y. & JONES, R. A. 2005. An interfacial instability in a transient wetting layer leads to lateral phase separation in thin spin-cast polymer-blend films. *Nat Mater,* 4**,** 782-6.
HILL, M. 1995. Ostwald ripening in polyethylene blends. *Polymer,* 36**,** 3369-3375.
HUANG, H., WU, Z., QI, X., ZHANG, H., CHEN, Q., XING, J., CHEN, H. & RUI, Y. 2013. Compression-coated tablets of glipizide using hydroxypropylcellulose for zero-order release: In vitro and in vivo evaluation. *International Journal of Pharmaceutics,* 446**,** 211-218.
HUTTON, J. T. & MORRIS, J. L. 1992. Long-acting carbidopa-levodopa in the management of moderate and advanced Parkinson's disease. *Neurology,* 42**,** 51-6; discussion 57-60.
HUYNH, C. T. & LEE, D. S. 2015. Controlled Release. *Encyclopedia of Polymeric Nanomaterials.*
INNOCENZI, P., MALFATTI, L., COSTACURTA, S., KIDCHOB, T., PICCININI, M. & MARCELLI, A. 2008. Evaporation of ethanol and ethanol-water mixtures studied by time-resolved infrared spectroscopy. *J Phys Chem A,* 112**,** 6512-6.
JANSSON, A., BOISSIER, C., MARUCCI, M., NICHOLAS, M., GUSTAFSSON, S., HERMANSSON, A.-M. & OLSSON, E. 2014. Novel Method for Visualizing Water Transport Through Phase-Separated Polymer Films. *Microscopy and Microanalysis,* 20**,** 394-406.
JARKE, A. 2009. *Effect of manufacturing conditions and polymer ratio on the permeability and film morphology of ethyl cellulose and hydroxypropyl cellulose free films produced by using a novel spray method.* Master, Uppsala University.
JASNOW, D. 1984. Critical phenomena at interfaces. *Rep. Prog. Phys.,* 47**,** 1059.
JIN, W., XU, W., GE, H., LI, J. & LI, B. 2015. Coupling process of phase separation and gelation in konjac glucomannan and gelatin system. *Food Hydrocolloids,* 51**,** 188-192.
JONES, R. A. L. & RICHARDS, R. W. 1999. *Polymers at Surfaces and Interfaces,* Cambridge, UK, Cambridge University Press.
JONKMAN, J. & STELZER, E. 2002. Resolution and Contrast and Two-Photon Microscopy. *Confocal and Two-Photon Microscopy: Foundations, Applications and Advances.* New York: Wiley.
K. HAAS, C. & M. TORKELSON, J. 1997. Two-dimensional coarsening and phase separation in thin polymer solution films. *Physical Review E*.
KHANDELWAL, M. & ALAN, H. W. 2013. Hierarchical Organisation in the Most Abundant Biopolymer –Cellulose. *MRS Online Proceedings Library,* 1504**,** 10.1557/opl.2013.379.
KLEIN, E. 2002. The role of extended-release benzodiazepines in the treatment of anxiety: a risk-benefit evaluation with a focus on extended-release alprazolam. *The Journal of clinical psychiatry,* 63 Suppl 14**,** 27-33.
KLEMM, D., HEUBLEIN, B., FINK, H. P. & BOHN, A. 2005. Cellulose: fascinating biopolymer and sustainable raw material. *Angew Chem Int Ed Engl,* 44**,** 3358-93.
KONINGSVELD, R., KONINGSVELD, R., STOCKMAYER, W. H. & NIES, E. 2001. *Polymer Phase Diagrams: A Textbook*, Oxford University Press.
KOUIJZER, S., MICHELS, J. J., VAN DEN BERG, M., GEVAERTS, V. S., TURBIEZ, M., WIENK, M. M. & JANSSEN, R. A. J. 2013. Predicting Morphologies of Solution

Processed Polymer:Fullerene Blends. *Journal of the American Chemical Society,* 135**,** 12057-12067.

LANGER, R. & PEPPAS, N. 1983. Chemical and Physical Structure of Polymers as Carriers for Controlled Release of Bioactive Agents: A Review. *Journal of Macromolecular Science, Part C,* 23**,** 61-126.

LANGER, R. & PEPPAS, N. A. 2003. Advances in biomaterials, drug delivery, and bionanotechnology. *AIChE Journal,* 49**,** 2990-3006.

LI, X., XING, R., ZHANG, Y., HAN, Y. & AN, L. 2004. Molecular weight effects on the phase morphology of PS/P4VP blend films on homogeneous SAM and heterogeneous SAM/Au substrates. *Polymer,* 45**,** 1637-1646.

LORÉN, N., HERMANSSON, A.-M., WILLIAMS, M. A. K., LUNDIN, L., FOSTER, T. J., HUBBARD, C. D., CLARK, A. H., NORTON, I. T., BERGSTRÖM, E. T. & GOODALL, D. M. 2001. Phase Separation Induced by Conformational Ordering of Gelatin in Gelatin/Maltodextrin Mixtures. *Macromolecules,* 34**,** 289-297.

LORÉN, N., LANGTON, M. & HERMANSSON, A. M. 2002. Determination of temperature dependent structure evolution by fast-Fourier transform at late stage spinodal decomposition in bicontinous biopolymer mixtures. *J. Chem. Phys.,* 116**,** 10536-10546.

LORÉN, N., LANGTON, M. & HERMANSSON, A. M. 2007. *Confocal fluorescence microscopy (CLSM) for food structure characterisation*.

MARUCCI, M., HJÄRTSTAM, J., RAGNARSSON, G., ISELAU, F. & AXELSSON, A. 2009. Coated formulations: new insights into the release mechanism and changes in the film properties with a novel release cell. *J Control Release,* 136**,** 206-12.

MARUCCI, M., RAGNARSSON, G., VON CORSWANT, C., WELINDER, A., JARKE, A., ISELAU, F. & AXELSSON, A. 2011. Polymer leaching from film coating: effects on the coating transport properties. *Int J Pharm,* 411**,** 43-8.

MCDONOUGH, R., CUETO, R., PHILLIES, G. D. J., RUSSO, P. S., DORMAN, D. & STRELETZKY, K. A. 2015. Fluorescent Labeling Can Alter Polymer Solution Dynamics. *Macromolecules,* 48**,** 7245-7255.

MEYERHOFER, D. 1978. Characteristics of resist films produced by spinning. *J. Appl. Phys.,* 49**,** 3993–3997.

MEZZENGA, R., SCHURTENBERGER, P., BURBIDGE, A. & MICHEL, M. 2005. Understanding foods as soft material. *Nature Materials,* 4**,** 729-740.

MOKARIAN-TABARI, P., GEOGHEGAN, M., HOWSE, J. R., HERIOT, S. Y., THOMPSON, R. L. & JONES, R. A. 2010a. Quantitative evaluation of evaporation rate during spin-coating of polymer blend films: Control of film structure through defined-atmosphere solvent-casting. *Eur Phys J E Soft Matter,* 33**,** 283-9.

MOKARIAN-TABARI, P., GEOGHEGAN, M., HOWSE, J. R., HERIOT, S. Y., THOMPSON, R. L. & JONES, R. A. L. 2010b. Quantitative evaluation of evaporation rate during spin-coating of polymer blend films: Control of film structure through defined-atmosphere solvent-casting. *The European Physical Journal E,* 33**,** 283-289.

MORRIS, E. R., CUTLER, A. N., ROSS-MURPHY, S. B. & REES, D. A. 1981. Concentration and shear rate dependence of viscosity in random coil polysccharide solutions. *Carbohydrate Polymers,* 1**,** 5-21.

MULLER-BUSCHBAUM, P. & STAMM, M. 2001. Film Thickness dependence of the domain size in weakly incompatible thin polymer blend films. *Colloid Polymer Science,* 279**,** 376-381.

NGUYEN, T. & LATKANY, R. 2011. Review of hydroxypropyl cellulose ophthalmic inserts for treatment of dry eye. *Clinical ophthalmology (Auckland, N.Z.),* 5**,** 587-591.

OTTESEN, V. 2011. Nucleation and growth. *In:* GROWTH, N. A. (ed.) *Wikimedia.*

PAWLEY, J. 2006. *Handbook of Biological Confocal Microscopy*, Springer US.

PETERSSON, M. 2005. Characterization of Phase Separation in Film Forming Biopolymer Mixtures. *Biomacromolecules,* 6**,** 932-941.

PICKER-FREYER, K. M. & DÜRIG, T. 2007. Physical mechanical and tablet formation properties of hydroxypropylcellulose: In pure form and in mixtures. *AAPS PharmSciTech,* 8**,** 82.

PICULLEL, L., BERGFELDT, K. & NILSSON, S. 1995. Factors Determining Phase Behaviour of Multi Component Polymer Systems. *Meeting, Biopolymer mixtures.* Nottingham: Nottingham University Press.

PLAYNE, D. P. & HAWICK, K. A. Data Parallel Three-Dimensional Cahn-Hilliard Field Equation Simulation on GPUs with CUDA. *In:* PDTA, ed., 2009.

RAWLINGS, J. M. & LUCAS, M. L. 1985. Plastic pH electrodes for the measurement of gastrointestinal pH. *Gut,* 26**,** 203-207.

RENKEMA, J. M. S. 2004. Relations between rhological properties and network structure of soy protein gels. *Food Hydrocolloids,* 18**,** 39-47.

RHODES, C. T. & PORTER, S. C. 1998. Coatings for controlled-release drug delivery systems. *Drug Dev Ind Pharm,* 24**,** 1139-54.

RÖDING, M., FAGER, C., OLSSON, A., VON CORSWANT, C., OLSSON, E. & LORÉN, N. 2021. Three-dimensional reconstruction of porous polymer films from FIB-SEM nanotomography data using random forests. *Journal of Microscopy,* 281**,** 76-86.

SAGUI, C. & GRANT, M. 1999. Therory of nucleation and growth during phase separation. *Physical Review E,* 59.

SAKELLARIOU, P. & ROWE, R. C. 1995. Interactions in cellulose derivative films for oral drug delivery. *Progress in Polymer Science,* 20**,** 889-942.

SAKELLARIOU, P., ROWE, R. C. & WHITE, E. F. T. 1985. The thermomechanical properties and glass transition temperatures of some cellulose derivatives used in film coating. *International Journal of Pharmaceutics,* 27**,** 267-277.

SCHAEFER, C. 2016. *Theory of nanostructuring in solvent-deposited thin polymer films.* PhD, Eindhoven University of Technology.

SCHAEFER, C., MICHELS, J. J. & VAN DER SCHOOT, P. 2016. Structuring of Thin-Film Polymer Mixtures upon Solvent Evaporation. *Macromolecules,* 49**,** 6858-6870.

SCHAEFER, C., VAN DER SCHOOT, P. & MICHELS, J. J. 2015. Structuring of polymer solutions upon solvent evaporation. *Physical Review E,* 91.

SCHOBER, T. J., BEAN, S. R., BOYLE, D. L. & PARK, S.-H. 2008. Improved viscoelastic zein–starch doughs for leavened gluten-free breads: Their rheology and microstructure. *Journal of Cereal Science,* 48**,** 755-767.

SCHOLTEN, E., M. C. SAGIS, L. & VAN DER LINDEN, E. 2004. Coarsening Rates of Bicontinuous Structures in Polymer Mixtures.

SCRIVEN, L. E. & STERNLING, C. V. 1960. The Marangoni Effects. *Nature,* 187**,** 186-188.

SERSHEN, S. & WEST, J. 2002. Implantable, polymeric systems for modulated drug delivery. *Advanced Drug Delivery Reviews,* 54**,** 1225-1235.

SHAW, M. & MACKNIGHT, W. 2005. *Introduction to Polymer Viscoelasticity*, Wiley.

SHEPPARD, C. & SHOTTON, D. 1997. *Confocal Laser Scanning Microscopy*, Springer Singapore.

SHOTTON, D. 1989. Confocal scanning optical microscopy and its applications for biological specimens. *Journal of Cell Science,* 94**,** 175.

SIGGIA, E. D. 1979. Late stages of spinodal decomposition in binary mixtures. *Physical Review A,* 20**,** 595-605.

SOLON, A. P., STENHAMMAR, J., CATES, M. E., KAFRI, Y. & TAILLEUR, J. 2018. Generalized thermodynamics of motility-induced phase separation: phase equilibria, Laplace pressure, and change of ensembles. *New Journal of Physics,* 20.

STEWART, S., DOMÍNGUEZ-ROBLES, J., DONNELLY, R. & LARRAÑETA, E. 2018. Implantable Polymeric Drug Delivery Devices: Classification, Manufacture, Materials, and Clinical Applications. *Polymers,* 10**,** 1379.

TANAKA, H. 1994. Double phase separation in a confined, symmetric binary mixture: Interface quench effect unique to bicontinuous phase separation. *Physical Review Letters,* 72**,** 3690-3693.

TANAKA, H. 2001. Interplay between wetting and phase separation in binary fluid mixtures: roles of hydrodynamics. *Journal of Physics: Condensed Matter,* 13**,** 4637–4674.

TANAKA, H. 2012. Viscoelastic phase separation in soft matter and foods. *Faraday Discussions,* 158.

TANAKA, H. & ARAKI, T. 1998. Spontaneous Double Phase Separation Induced by Rapid Hydrodynamic Coarsening in Two-Dimensional Fluid Mixtures. *Physical Review Letters,* 81**,** 389-392.

TANAKA, H. & NISHI, T. 1985. New types of phase separation behavior during the crystallization process in polymer blends with phase diagram. *Phys Rev Lett,* 55**,** 1102-1105.

TIWARI, G., TIWARI, R., SRIWASTAWA, B., BHATI, L., PANDEY, S., PANDEY, P. & BANNERJEE, S. K. 2012. Drug delivery systems: An updated review. *Int J Pharm Investig,* 2**,** 2-11.

TOLSTOGUZOV, V. 2003a. Some thermodynamic considerations in food formulation. *Food Hydrocolloids,* 17**,** 1-23.

TOLSTOGUZOV, V. 2003b. Thermodynamic considerations of starch functionality in foods. *Carbohydrate Polymers,* 51**,** 99-111.

TOOLAN, D. T. W., HAQ, E. U., DUNBAR, A., EBBENS, S., CLARKE, N., TOPHAM, P. D. & HOWSE, J. R. 2013. Direct observation of morphological development during the spin-coating of polystyrene-poly(methyl methacrylate) polymer blends. *Journal of Polymer Science Part B: Polymer Physics,* 51**,** 875-881.

TOOLAN, D. T. W. & HOWSE, J. R. 2013. Development of in situ studies of spin coated polymer films. *J. Mater. Chem. C,* 1**,** 603-616.

UHRICH, K. E., CANNIZZARO, S. M., LANGER, R. S. & SHAKESHEFF, K. M. 1999. Polymeric Systems for Controlled Drug Release. *Chemical Reviews,* 99**,** 3181-3198.

VAN FRANEKER, J. J., WESTHOFF, D., TURBIEZ, M., WIENK, M. M., SCHMIDT, V. & JANSSEN, R. A. J. 2015. Controlling the Dominant Length Scale of Liquid–Liquid Phase Separation in Spin-coated Organic Semiconductor Films. *Advanced Functional Materials,* 25**,** 855-863.

WALHEIM, S., BÖLTAU, M., MLYNEK, J., GEORG, K. & STEINER, U. 1997. Structure Formation via Polymer Demixing in Spin-Cast Films. *Macromolecules,* 30**,** 4995-5003.

WASSÉN, S., BORDES, R., GEBÄCK, T., BERNIN, D., SCHUSTER, E., LORÉN, N. & HERMANSSON, A.-M. 2014. Probe diffusion in phase-separated bicontinuous biopolymer gels. *Soft Matter,* 10**,** 8276-8287.

WASSÉN, S., LORÉN, N., VAN BEMMEL, K., SCHUSTER, E., RONDEAU, E. & HERMANSSON, A.-M. 2013. Effects of confinement on phase separation kinetics and final morphology of whey protein isolate–gellan gum mixtures. *Soft Matter,* 9.

WILLIAMS, E. L., GORELIK, S., PHANG, I., BOSMAN, M., VIJILA, C., SUBRAMANIAN, G. S., SONAR, P., HOBLEY, J., SINGH, S. P., MATSUZAKI, H., FURUBE, A. & KATOH, R. 2013. Nanoscale phase domain structure and associated device performance of organic solar cells based on a diketopyrrolopyrrole polymer. *RSC Advances,* 3.

WILTZIUS, P., CUMMING, A. W. & SHI, B. Q. 1994. Domain growth and wetting in phase-separating fluid mixtures. *Macromolecular Symposia,* 79**,** 71-80.

YAMAMURA, M., NISHIO, T., TOSHIHISA, K. & ATACHI, K. 2002. Evaporation-induced pattern formation in polymer films via secondary phase separation. *Chemical Engineering Science,* 57**,** 2901-2905.

YIANTSIOS, S. G., SERPETSI, S. K., DOUMENC, F. & GUERRIER, B. 2015. Surface deformation and film corrugation during drying of polymer solutions induced by Marangoni phenomena. *International Journal of Heat and Mass Transfer,* 89**,** 1083-1094.

ZHU, J., BALIEU, R., LU, X. & KRINGOS, N. 2018. Microstructure evaluation of polymer-modified bitumen by image analysis using two-dimensional fast Fourier transform. *Materials & Design,* 137**,** 164-175.

ZOUMPOULI, G. A. & YIANTSIOS, S. G. 2016. Hydrodynamic effects on phase separation morphologies in evaporating thin films of polymer solutions. *Physics of Fluids,* 28**,** 082108.